SAPIENZA
UNIVERSITÀ DI ROMA

SENSITIVE LABEL-FREE AND FLUORESCENCE CANCER BIOMARKER DETECTION USING ONE DIMENSIONAL PHOTONIC CRYSTAL BIOCHIPS

BY

ALBERTO SINIBALDI

A dissertation submitted in partial fulfillment
of the requirements for the degree of
Doctor of Philosophy
In Electromagnetism
at SAPIENZA University of Rome
December 2016

Supervisor

Prof. Francesco Michelotti

To Lisena

ACKNOWLEDGMENTS

First and foremost, I would like to thank my mentor Prof. Francesco Michelotti for his guidance, inspiration, support, and patience during my Ph.D. study. He allowed me great freedom to work independently and to initiate projects and collaborations, and encouraged me to work with my own imagination and creativity. Meanwhile, he guided, criticized, and provided any support I needed. I am immensely grateful for his advice, support and perpetual optimism during (and not only)my doctorate period.

I am extremely thankful to my research group members for the often helpful, usually entertaining discussions we've had: Aleksei Anopchenko, Agostino Occhicone, Elisabetta Sepe and Riccardo Rizzo.

I would also like to thank Dr. Norbert Danz, Dr. Peter Munzert, Dr. Frank Sonntag and Stefan Schmieder for their collaboration, fruitful discussions and help on 1DPC and microfluidics fabrication. I would like to give special thanks to Dr. Patrizio Giacomini and Dr. Camilla Sampaoli for biological materials and fruitful scientific exchanges. Without them, I can hardly imagine my thesis work being accomplished so smoothly and comprehensively.

I'd like to thank Dr. Paola Rivolo and Dr. Francesca Frascella for the initial guidance on surface chemistry and for plasma polymerized acrylic acid coatings production.

Most importantly, I would like to thank my wife Giulia for her love, encouragement, support and patience. For the past four years, I have had the joy and privilege to share all of my successes and all of my fears with her. Without her support, nothing would have ever been possible.

LIST OF FIGURES

LIST OF TABLES

TABLE OF CONTENTS

ABSTRACT

Biological and biochemical processes play a very important role in living organisms and their understanding is particularly important in medicine, biology and biotechnology. Optical biosensors hold great promise for solving challenging molecular recognition issues, such as the detection of biomolecules at very low concentration. In this framework, a direct measurement of the binding of analytes to a target molecule in biological samples is an essential step in diagnosis and in understanding how biomolecules interact under physiological conditions.

In this thesis, I contributed to the development of an optical platform that combines label-free and fluorescence detection modes. Such a platform makes use of one-dimensional photonic crystals (1DPC) sustaining Bloch surface waves (BSW) to detect relevant cancer biomarkers in body fluids. BSWs are surface electromagnetic waves that propagate along the truncation interface between a 1DPC and an external medium (the analyte) and can be strongly confined with a significantly enhanced field at the surface. By exploiting such features, 1DPC sustaining BSW (BSW biochips) are used as optical transducers that convert refractive index changes and fluorescence emission at their surface into a measurable optical signal.

After discussing the results of the platform development, I report on the use I made of BSW biochips to detect clinically relevant concentrations of Angiopoietin 2 and ERBB2 in different biological matrices. The aim of such a research endeavour is clear: to reveal cancer by means of integrated optofluidic structures before cancer reveals itself. In the case of breast cancer, for example, it is a fact that ERBB2 is a pivotal biomarker and targetable oncogenic driver associated with several different aggressive subtypes. To quantitate Angiopoietin 2 and soluble ERBB2, I developed and implemented specific sandwich detection assays in which the BSW biochips' sensitive surface is tailored with monoclonal antibodies for highly specific biological recognition. In a second step, a second antibody quantitatively detects the bound analytes. The strategy of the present approach takes advantage of the combination of both label-free and fluorescence techniques, making bio-recognition more robust and sensitive. In the fluorescence operation mode, the platform can attain the limit of detection 0.3 ng/mL (1.5 pM) for ERBB2 in cell lysates, which is the most complex biological matrix studied in the present work. Such a resolution meets the international guidelines and recommendations (15 ng/mL) for diagnostic ERBB2 assays that in the future may help to assign more precisely therapies counteracting cancer cell proliferation and metastatic spread.

CHAPTER 1

Introduction

1.1 OPTICAL BIOSENSORS

During the last two decades, the demand for high-throughput, sensitive, and multiplexed detection of biomarkers has speeded up the development of a variety of analytical platforms based on an optical transduction mechanism. Optical biosensing devices are mostly intended for point of care biomoleculars detection. The biosensors based point of care testing segment accounted for over 40% (on a total market value of $11.39 billion in 2013, expected to be $21.17 billion by 2020) of the end-use market in 2013 [1]. Moreover, the rising demand for portable and integrated technologies that can be operated by untrained personnel outside conventional laboratories is expected to improve the usage rates.

Optical biosensors fall under this heading, holding great promise for solving challenging molecular recognition issues, such as the detection of biomolecules at very low concentration. In this framework, a direct measurement of the binding of analytes to a target molecule in biological samples is an essential step in diagnosis and in understanding how biomolecules interact under physiological conditions. Furthermore, specificity and affinity between biomolecules can be assessed by means of optical systems, leading to the discovery and development of new pharmaceuticals and cancer treatments.

An optical biosensor is an analytical device that integrates a biological sensing element (e.g., an enzyme, antibody, DNA strands and aptamers) with an optical transducer, whereby the interaction between the target and the bio-recognition molecules is translated into a measurable electrical signal. Optical biosensors that exploit light absorption, fluorescence, luminescence, reflectance, Raman scattering and refractive index are powerful alternatives to conventional analytical techniques (Fig. 1.1). These biosensors provide rapid, highly sensitive, real-time, and high-frequency monitoring without any time-consuming sample concentration and/or prior sample pre-treatment steps. Although optical biosensors have great potential applications in

the areas of environmental monitoring, food safety, drug development, biomedical research, and diagnosis [2-5], their use in fields of environmental pollution control and early warning is still in the early stages [6].

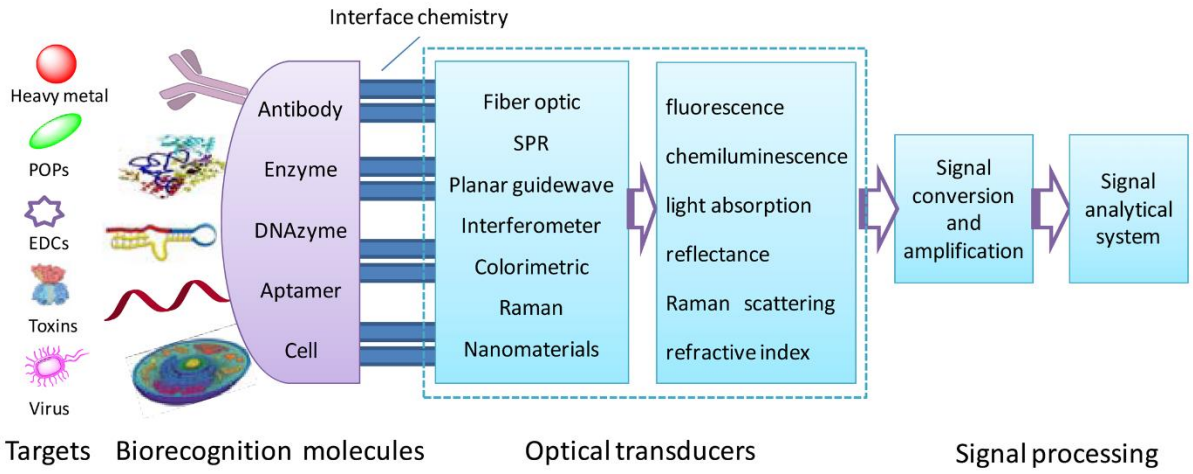

Figure 1.1 – Biosensor's optical transduction scheme [6].

For example, the complete characterization of a novel therapeutic antibody to treat cancer (see Chapter 6), joined to the screening of large repositories of antibodies becomes necessary in order to identify high specificity and high affinity binders, followed by a more detailed determination of epitope specificity (epitope mapping). However, the development of a technology that permits to identify such binding is challenging because of the characteristics of the analytes, such as drug compounds (often with molecular weights of 300 Da or even below), DNA oligonucleotides, lipids, peptides, enzymes, antibodies, and viral particles. These molecules are exceedingly small and different in size (e.g. viruses) and are present in complex matrices (human plasma, serum and cell lysates) in a concentration range of (pM – nM), making the specific detection hard to track.

As shown in Fig. 1.2, there are two main detection approaches that can be implemented in optical biosensing: fluorescence or label-free detection.

In fluorescence-based detection, either target molecules or bio-recognition molecules are labelled with fluorescent labels, and the intensity of the emitted fluorescence at certain wavelengths reveals the presence and the strength of the interaction between target and bio-recognition molecules (top row in Fig. 1.2).

On the other hand, there are methods that allow direct detection of biological analytes without labelling processes. They generally measure some physical properties of the analytes, such as mass, volume, polarization, dielectric permittivity, and conductivity, using an appropriate

sensor. In this case, the biosensor acts as a transducer that can convert one of these physical properties (for example, the mass of a substance deposited on the sensing surface) into a detectable signal that can be measured by an instrument. These biosensing mechanisms are illustrated in the bottom row of Fig. 1.2.

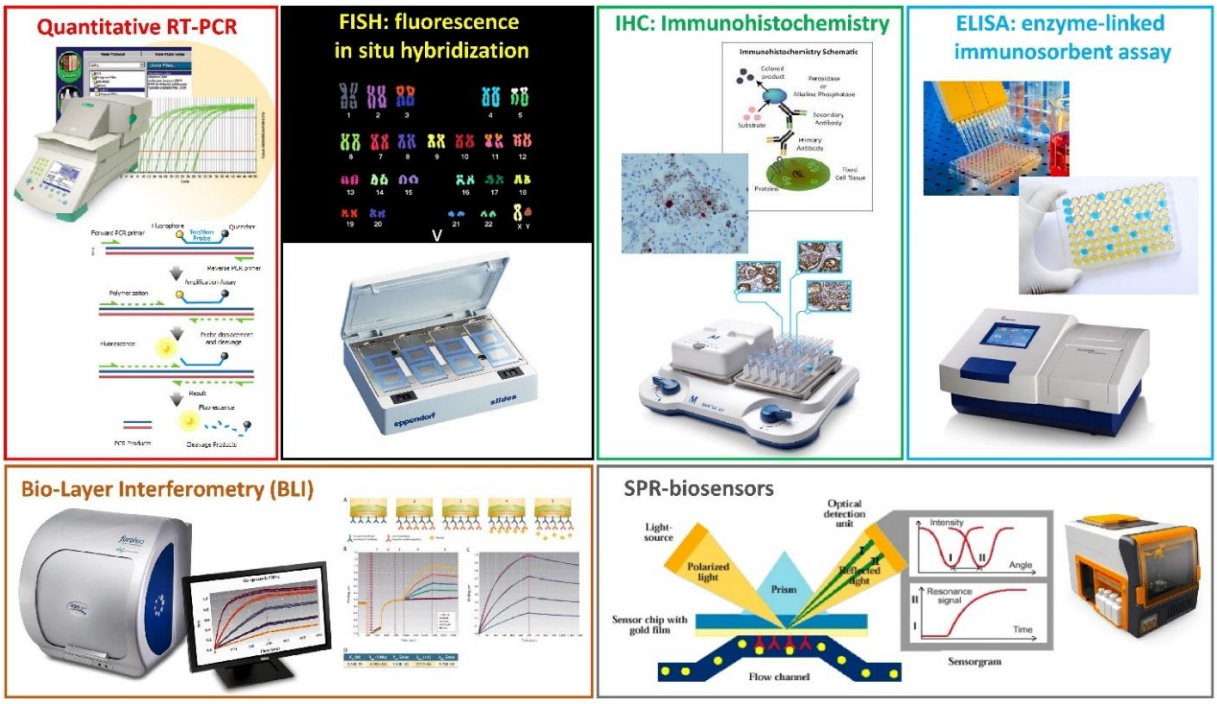

Figure 1.2 – Commercial label-free or fluorescence techniques exploiting an optical transduction mechanism.

1.2 SURFACE WAVE BIOSENSORS AND MOTIVATION OF THE WORK

A large number of optical biosensors exploits evanescent waves to probe the presence of analytes at the sensor surface in the proximity of the surrounding medium by detecting the effective refractive index. Generally, the evanescent field intensity decays exponentially from the sensing surface, with a decay length of about 200 nm into the probed medium. Such a decay length (named penetration depth) depends on the technology used.

In recent years, a large amount of interest has been focused on optical phenomena connected to Surface Plasmon Polaritons (SPP) on flat and structured metal films [8]. These kind of surface waves are particularly interesting because of three important features: the strong electromagnetic field enhancement, the spatial confinement at interfaces and a consequent high

sensitivity upon changes of the refractive index at metal/dielectric interfaces. One of the most simple and widespread used sensing configuration in sensors based on Surface Plasmon Resonance (SPR) is known as the Kretschmann configuration, as shown in Figure 1.3A. It is a fact that most of bio-sensors used in proteomics are based on the exploitation of SPR at the surface of thin gold layers deposited on glass prisms. Native and recombinant proteins are used extensively, from investigations of disease pathways through to the identification of protein targets for drug therapies [9]. Such sensors exploit the perturbation of the dispersion law of SPP when the surface of the metal film is exposed to an analyte [10]. As shown in Figure 1.3B, the excited surface plasmon mode is very sensitive to the influence of bound molecules in the dielectric medium adjacent to the metal film (see Fig.1.3C), with a sensitivity in the range of 80 degree (deg, incident angle) per refractive index unit (RIU) [7]

Some attempts to substitute metals with dielectrics for the design and fabrication of functional sensing elements were already reported. Reflectometric interference spectroscopy, measuring the spectral shift of reflected light at a given angle and grating coupling external light to waveguide modes were proposed.

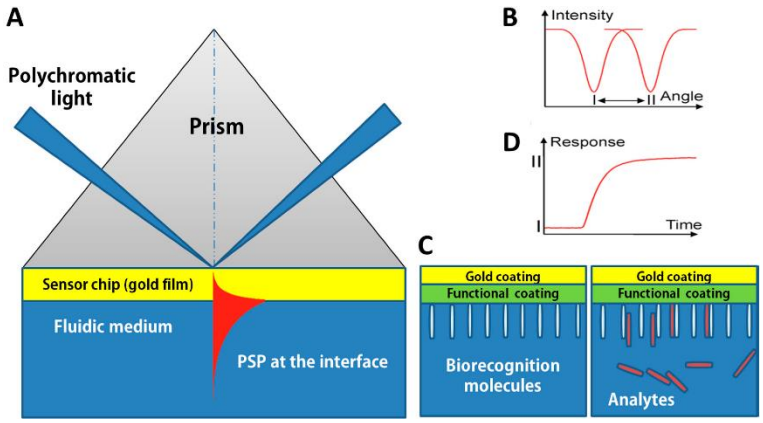

Figure 1.3 - Surface plasmon resonance (SPR) biosensor: (**A**) Kretschmann geometry of the ATR method; (**B**) spectrum of reflected light before and after refractive index change; (**C**) analyte-bio-recognition elements binding on SPR sensor surface and (**D**) refractive index changes caused by the molecular interactions in the reaction medium [10].

The main shortcomings of the SPP based sensing approaches are the following:

- Design limitations imposed by the dielectric properties of the metal layers
- Large radiation absorption in metal layers at optical frequencies and limitation to the sensitivity
- Quenching of fluorescence emitted by fluorophores bound to the metal layers

- Sensitivity decrease upon deposition of additional layers
- Limitation to the surface functionalisation techniques
- Limitation to the SPP biochip design

Such shortcomings restrict the detection resolution (LoD) and preclude its use for applications that require detection of small molecules, low surface coverage of bound molecules and fluorescent molecules [11].

The present work is focused on the development of an optical biosensing platform that is capable to operate in both label-free and fluorescence modalities. Such a combined approach, making use of either gold thin layers [12] or low periodicity dielectric stacks [13,14], is recently gaining attention from the biosensing community. With reference to Fig. 1.4, one dimensional photonic crystals (1DPC) sustaining Bloch surface waves (BSW) are used as an optical transducer in order to convert refractive index changes and fluorescence emission at their surface into a measurable optical signal.

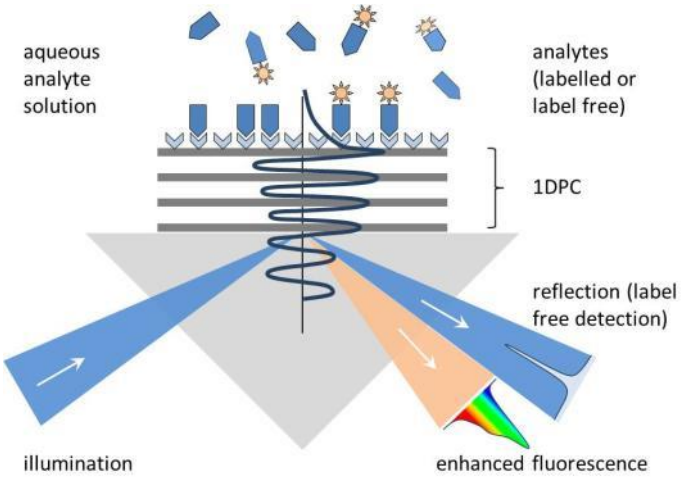

Figure 1.4 - Simplified view of the proposed biosensors. Label-free analytes are detected by revealing the shift of the BSW resonance appearing in the reflected beam. Labeled analytes are detected by collecting the fluorescence whose intensity is strongly enhanced by the localization of both excitation and luminescence waves. The luminescence beam is shifted with respect to the reflectance one due to the large dispersion of the Bloch modes.

The two basic elements constituting the tandem approach are the label-free detection based on the resonance shift, and the enhanced spectral analysis of fluorescence emitted by biomolecules immobilised on the surface.

The properties of the BSW sustained by properly designed 1DPC can be finely engineered so as to optimise both label-free and fluorescence real-time sensing schemes.

- In the first case, BSW can be used in an SPR-like sensing scheme exploiting label free detection based on resonance shifts, as shown in the Fig. 1.4 (blue reflected beam). Thanks to the high tunability of the 1DPC structures and the low absorption of the dielectric materials employed, BSW can be excited in a wide spectral range (from NIR to visible), providing 10 to 100 times narrower resonances compared to those associated to surface plasmon polaritons (SPP).
- In the second case, the strong field confinement at the very last interface of the photonic crystal can be used to enhance the excitation of fluorescent labels placed in close proximity of the surface by two to four orders of magnitude. As a complementary mechanism, the Stokes-shifted fluorescence emission from labels immobilized at the surface is preferentially coupled to BSW sustained by the 1DPC and leaks back into the prism, as shown in Fig. 1.4 (pink beam). This results in a further improvement of fluorescence collection. Angular separation between the reflected and the fluorescence beam is guaranteed by the strong dispersion of BSW modes, compared to that of SPP.

With reference to the SPR shortcomings listed above, the advantages of the BSW based approach can be schematically summarized as follows. BSWs provide a very sensitive optical transduction mechanism of chemical/physical alteration taking place close to dielectric or metallic surfaces. Unlike for surface plasmons, the resonances associated with BSW can be made very narrow, due to the low losses caused by scattering and absorption of the material. The use of dielectrics opens new perspectives in the chemical functionalization, providing the chemical specificity of the sensors. Nevertheless, each additional layer (perhaps organic or inorganic) that is added to the 1DPC can be taken in to account in the multilayer definition, thus leading to a BSW always lying on the last interface.

1.3 PERFORMANCES OF THE BSW APPROACH

In this section, the main parameters quantifying the BSW sensors' performance are introduced, keeping an eye to the SPR standards. Some of these parameters are inherent to the geometry of the sensor itself, others have a strong dependence on the surface functionalization and the biochemical reactions that take place during bio-sensing events.

1.3.1 LABEL-FREE OPERATION: Sensitivity, Figure of merit and Limit of detection

The sensitivity is a crucial parameter in evaluating the performance of a label-free biosensor. It is defined as the ratio of the change in sensor output response to the change in the quantity to be measured (e.g., the analyte mass density on the sensing surface). In turn, a mass density change can be proportionally related to a change in the effective refractive index after bio-molecular interactions. The sensitivity formulation can depend on the detected change (the thickness or refractive index) and the detection methods (the angle, wavelength, intensity, or phase). In our case, the incident angle (θ in Fig.1.5), changes as a function of refractive index variation (or analyte concentration) is assumed as volume sensitivity:

$$S_V = {\partial\theta}/{\partial n}\Big|_{\theta_{RES}}$$

The bulk solvent refractive index sensitivity in the units of deg per refractive index unit (deg/RIU) permits a comparison of the sensing capability among optical technologies that exploits evanescent field.

Strictly related to the volume sensitivity S_V is the surface sensitivity (S_S) defined as follows:

$$S_S = {S_V \cdot (n_{BIO} - n_W)}/{L_{PEN}}$$

where n_{BIO} and n_W are the refractive indices of the biomolecules and water, respectively. The L_{PEN} is the penetration depth of the evanescent field in the probing medium. The sensitivity of an optical biosensor can be characterized in a number of ways, depending on the applications and detection methods. However, an important and inherent comparative parameter of sensing devices is the figure of merit (FoM) [7]:

$$FoM = {D \cdot S}/{W}$$

where is the W is the full-width of the resonant dip at half-maximum, and D is the depth of the resonance defined in Fig. 1.5.

The limit of detection (LoD) or resolution is the minimum change in the parameter that can be resolved by a sensing device [20]. Practically, it is measured as follows:

$$LoD = \frac{2\sigma}{S} \propto \frac{1}{FoM}$$

where S is the sensitivity and σ is the baseline noise of the transduction signal.

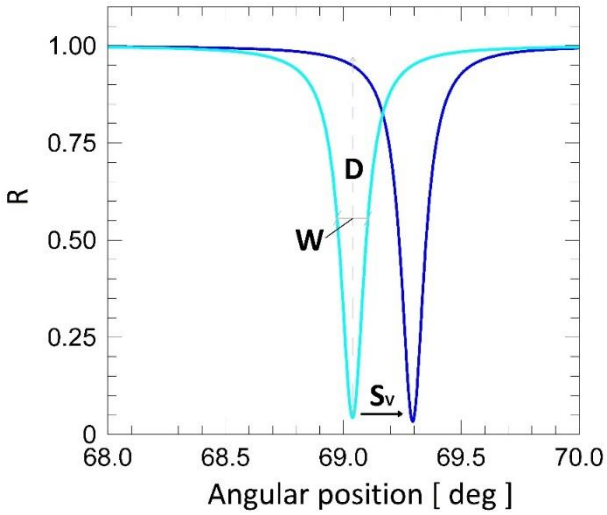

Figure 1.5 – Angular reflectance profile and main performance parameters.

Obviously, the LoD can be improved by decreasing σ (level of noise) and/or by increasing the FoM. Moreover, the LoD can be expressed in different ways according to the nature of the variations occurring at the biosensor surface. First, most of the optical sensors are sensitive to RI changes in the bulk solution, and the resolution in terms of refractive index changes can be used to compare the sensor capability. The parameters introduced above are invariant to the biochemical activity of the sensor and can be considered as physical parameters of the optical transduction element. The overall performance of a biosensor, taking into account the quality of the surface chemistry, can be characterized in terms of LoD (for example in the surface mass density units of ng/cm^2), allowing the evaluation of the analyte density after binding events. This latter it is a critical parameter for detection of analytes present at low concentration or detection of adsorbed molecules with low molecular weight. However, the surface mass density is experimentally difficult to determine, and it is usually obtained by relating it to the effective refractive index or thickness that could be measured experimentally (e.g., as in Chapter 6). Another way to measure bio-interactions is to use the analyte concentration (in units of ng/mL or molarity), which is useful and easy to handle in experiments. However, a detection limit defined in this manner needs to be specified for each type of biomolecule, as it depends on the molecular weight of target molecule and its affinity to the capturing elements.

1.3.2 FLUORESCENCE OPERATION: Enhancement of the excitation field and directionality of the emission

The excitation of SPP on a metal/dielectric interface and of BSW on a 1DPC, provides a strong electromagnetic field intensity at the boundary of the structure. This leads to two important effects: firstly, an enhanced fluorescence signal due to the resonant coupling between the emitting fluorophores and the surface waves (BSW or SPP), secondly a directional fluorescence emission, resulting in a higher fluorescence collection efficiency (that leads to an increased sensitivity) and enabling better suppression of background noise.

In the field of fluorescence-based SPR-biosensors, mainly two techniques exploit the fluorescence emission, namely, the surface plasmon field-enhanced fluorescence (SPFS) and the surface plasmon coupled fluorescence (SPCE) [15]. In SPFS, the enhanced excitation of the fluorophores upon resonant coupling of the excitation radiation to the SPP sustained by the metallic film leads to an overall measured enhanced fluorescence. On the other hand, SPCE is based on the coupling of fluorescence and SPR. Due to the strong energy field within the near-field distance, when the wave-vector matching occurs, fluorophores can be coupled with SPPs, thereby inducing the release of energy as radiation. Since the plasmon wave can be considered as an evanescent field distributed around ~200 nm beyond the surface, fluorophores must be placed up to 200 nm above the metallic film so that coupling occurs. Due to its unique properties, SPCE [16] has been proposed as a tool to significantly improve the detection performances. Its main advantages are the already mentioned directionality of fluorescence emission, which results in a higher signal-to-noise ratio (higher sensitivity) and in the ability to detect smaller volumes.

As all the SPR-based techniques, SPCE and SPFS are affected by the quenching phenomenon, resulting in an attenuation of the detectable signal through the metal layer, and thereby in a high dependence on the distance between the (metal/dielectric) interface and the emitter position. In fact, due to the evanescent profile of SPPs, only the surface molecules can be excited [17].

BSW-based techniques have several advantages compared to SPFS and SPCE. First, using dielectric media to enhance the fluorescence, they do not suffer from signal losses. Second, the distance between the emitters and the 1DPC surface is a less critical parameter due to the absence of quenching and strong absorption effects played by metals [18]. Furthermore, the angular separation between the reflected and the fluorescence beam is guaranteed by the strong

dispersion of BSW modes. As a result, the excitation of fluorescent labels placed in close proximity of the surface is two to three [19] orders of magnitude greater than those associated with SPR, enabling the detection of smaller concentrations of biomarkers.

As an example in Figure 1.6 we show the calculation of the distributions of the fields associated to the resonant excitation at λ= 826 nm of either a SPP on a thin metal layer or a BSW on a 1DPC [31]. The surface waves are excited in the Kretschmann configuration with a plastic prism (TOPAS n = 1,526) and the external medium is ethanol (n = 1.357). The distributions are compared to the intensity distribution for the single prism/ethanol interface under total internal (TIR) reflection conditions and at the same angle. As it is seen the BSW field at the surface of the sensor is strongly enhanced with respect to the TIR case (factor 1000) and with respect to the SPR case.

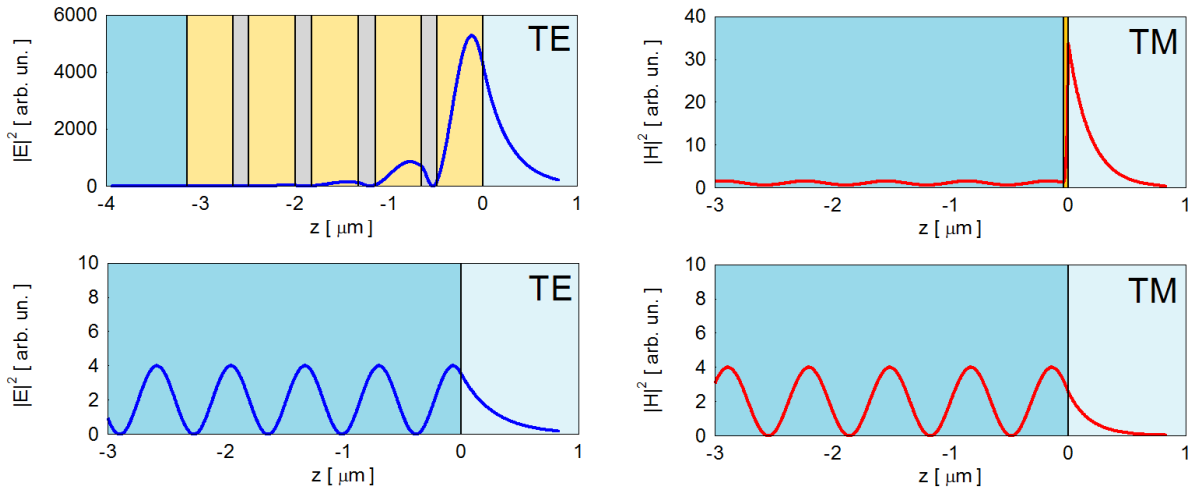

Figure 1.6 - Calculated field distributions associated to the resonant excitation at λ=826 nm for a BSW on a 1DPC and TIR edge on a prism/ethanol interface under TIR reflection (blue curves on the left hand-side).Under the same conditions, we recalculated the field distribution in case of SPP on a thin metal layer and TIR edge on a prism/ethanol single interface (red profiles on the right hand-side).

On the other hand, in Fig. 1.7 we show the radiation emission pattern for a Cyanine 7 dye at the surface of either a metal layer or a 1DPC. The metal layer, the 1DPC, the substrate and the external medium are the same used to calculate the fields shown in Fig. 1.6. In the simulations, the Cyanine 7 molecule was positioned 10 nm away from the surface to neglect quenching, which is not taken into account in the simulations. The angular patterns are compared to that obtained for a molecule at the prism/ethanol single interface. As it can be seen, for BSW on 1DPC, the emission from the substrate side is strongly modified with respect to bare substrate and shows a preferential direction in both TE and TM cases, respectively. About one half of

the energy is emitted from the substrate side and is strongly confined in a reduced angular cone providing an higher fluorescence collection efficiency.

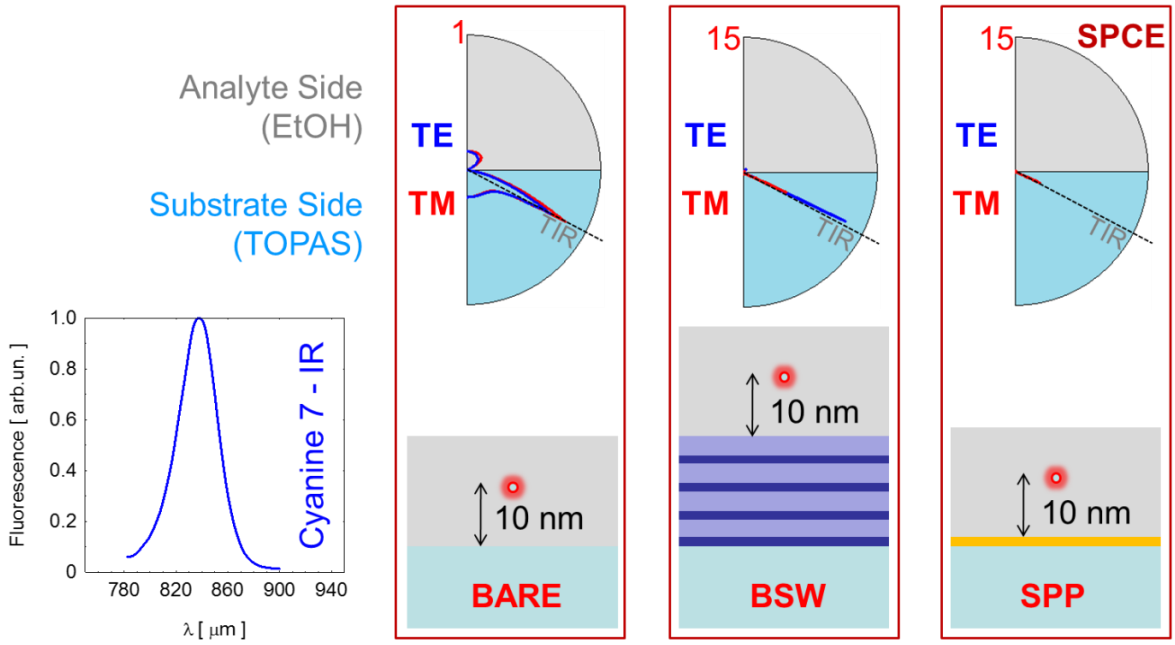

Figure 1.7 – Directionality of the emitted light from different systems: single interface at TIR edge; 1DPC in which the two modes TE and TM are strongly re-directed in the substrate side and thin metallic film in which only TM emission can be re-arranged.

Inclusion of quenching in the calculation would further shift the balance in favour of BSW, given that they do not suffer from quenching by any metal layer.

1.4 STATE OF ART OF OPTICAL BIOSENSORS COMBINING LABEL-FREE AND FLUORESCENCE DETECTION

Only a restricted number of optical biosensing platforms are able to work combining both approaches (label-free and fluorescence) using the same read-out system.

Recently, Wang et al. [12] demonstrated that surface plasmon-enhanced fluorescence spectroscopy (SPFS), employing long- range surface plasmons (LRSP), can be efficiently used for the detection of free prostate specific antigen (f-PSA) in buffer and human serum. LRSPs are surface plasmon modes that propagate along a thin metallic film with orders of magnitude lower damping compared to regular surface plasmons and penetrating up to micrometers in distance from the sensor surface. By exploiting such a penetration depth, they anchored a photo-crosslinkable dextran hydrogel binding matrix (PCDM) with micrometer thickness.

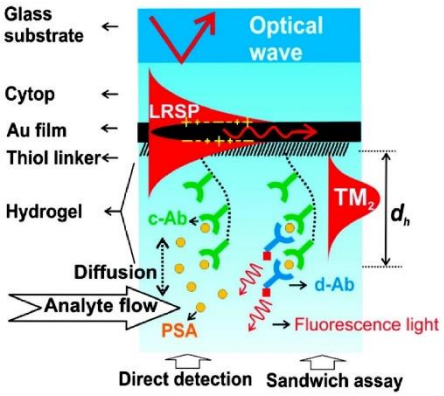

Figure 1.8 - Scheme of the LRSPs on the sensor surface with a hydrogel binding matrix for f-PSA detection immunoassays.

This approach provides large binding capacity and allows a sensitive detection strategy in f-PSA sandwich immunoassays. Thus this latter method could suffer from quenching just because a thin metal layer is close to a radiating dipole (dye molecule) used to complete the immunoassay. Moreover, the use of a 3D hydrogel probing structure could be affected by analyte diffusion problems/limitations reducing overall sensing performances (Fig. 1.8).

In 2013, Chen et al.[13] proposed a new concept of optical microscopy combining nanostructured photonic crystal surfaces and a hyperspectral reflectance imaging detection. Such technique, called Photonic Crystal Enhanced Microscopy (PCEM) enables the label-free, quantitative, and kinetic monitoring of biomaterial interaction with substrate surfaces. In principle, such a technique can be used to investigate a broad class of materials, which include dielectric nanoparticles, metal plasmonic nanoparticles, biomolecular layers, and live cells. Because PCEM does not require any cytotoxic stains or photo-bleachable fluorescent dyes, it could be useful for monitoring the long-term interactions of cells with extracellular matrix surfaces. Due to its intrinsic characteristics (i.e. localized electromagnetic field at the interface), PCEM is sensitive to the attachment of cell components within ~200 nm of the photonic crystal surface, which may correspond to the region of most interest for adhesion processes that involve stem cell differentiation, chemotaxis, and metastasis.[20]. As shown in Fig. 1.9, the kinetics of dynamic interaction between cellular materials and surface coating materials can be measured quantitatively using PCEM. In Fig. 1.9D, a sequence of movie frames demonstrates murine dental stem cells (mHAT9a) gradually attaching on a fibronectin-coated PC biosensor surface [13].

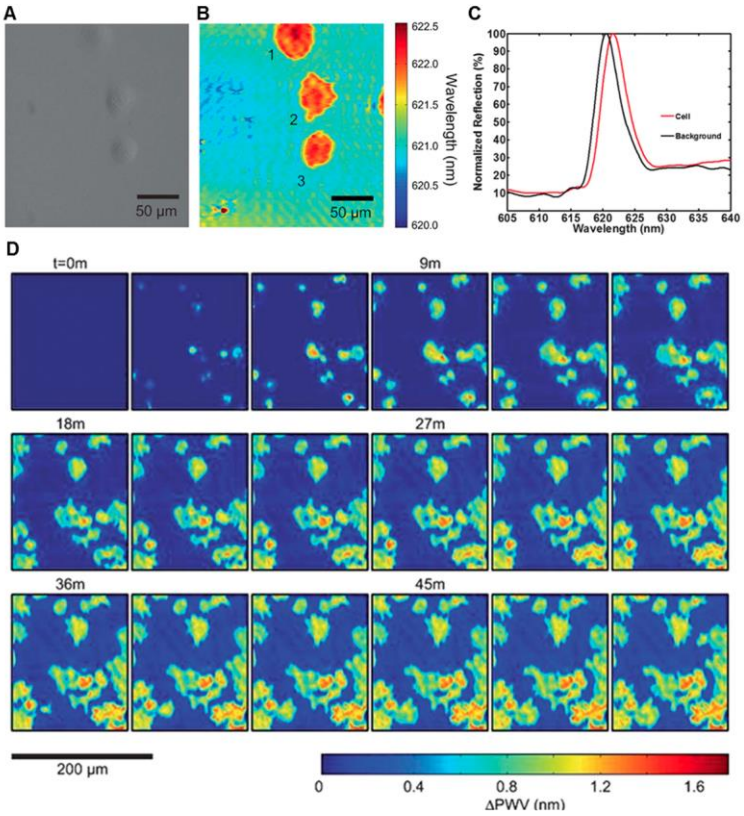

Figure 1.9 - Wavelength-sensitive live cell image from PCEM. (**A**) Brightfield and (**B**) resonant peak wavelength value (PWV) images of pancreatic carcinoma cells (Panc-1) attached to the PC surface. (**C**) Representative spectra (normalized) from background regions and regions with cellular attachment. Selected areas of the PWV image from beneath a cell show the PWS of a typical Panc-1 cell is ~1.0 nm; (**D**) Time-lapse PWS images of cellular attachment of dental stem cells (mHAT9a) [13].

This technique is not only limited to detection in label-free modality, but is also capable of enhancing the emission and extraction from optical emitters (such as fluorescent dyes) via the evanescent field at the interface of the PC biosensor surface. Fig. 1.10 illustrates the corresponding enhanced fluorescence images for membrane dye-stained 3T3 fibroblast cells [14]. The combination of both modalities extends the PC-enhanced imaging system to be multi-functional and capable of imaging in numerous bio-applications. To implement such a technique, a fluorescence microscope equipment (or similar) is strictly needed. This could represent a disadvantage in a further development step that implies a miniaturization of the system.

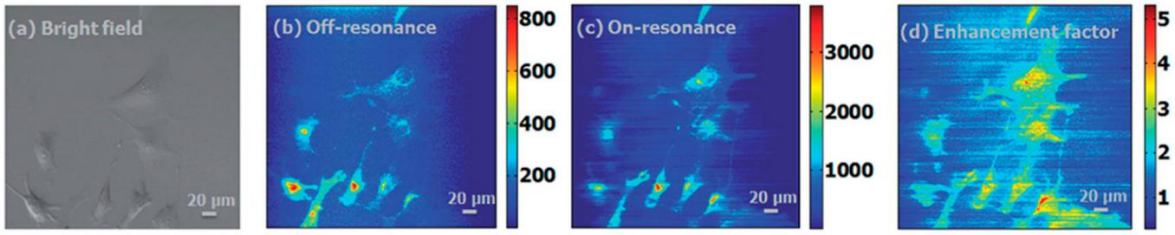

Figure 1.10 – Bright field and PCEF images of membrane dye-stained 3T3 fibroblast cells: (a) brightfield, (b) off-resonance PCEF, (c) on-resonance PCEF, (d) enhancement factor image [14,20].

In order to overtake SPR and PCEF possible drawbacks, in this work we focus our attention on simple one-dimensional photonic crystal (1DPC) structures (i.e. alternating pairs of dielectric layers, periodicity along one direction only). Compared to more complicated 2D/3D PC structure-based sensors [21-23] or photonic crystal fibers [24], 1DPC structures are simpler to fabricate and the FoM can be easily adjusted by varying the number/thickness of alternating pairs or changing dielectric materials [25]. The periodicity of the 1DPC provides a photonic bandgap, such that a range of wavelengths is not allowed to propagate within the structure. Inside such a stop band surface modes can exist, can be properly excited and a Bloch surface wave can be launched at the surface sensor. By slightly altering the periodicity of the 1DPC, a thin dielectric absorbing layer can be added on top of the periodic structure in order to confine more efficiently and enhance the electromagnetic field in the vicinity of the sensing area (details in Chapter 2). The resolution in terms of LoD and FoM can be improved, with respect to a standard SPR sensor, due to reduced losses of all-dielectric structures. This permits to make use of fluorescent molecules without facing absorption and quenching issues. Moreover, the capturing surface is completely available for the biomolecular reactions keeping the possibility to make the 1DPC biosensor and the read-out system more compact (see in Chapter 4).

1.5 DISSERTATION OUTLINE

In this work, the development of a combined label-free/fluorescence optical biosensor using a 1DPC structure is presented. The sensing surface available for analyte binding allows real-time label-free binding measurements and fluorescence investigation by using the same optical read-out system (described in details in Chapter 4). This configuration possesses the advantages of evanescent-field-based optical without the light-coupling problems [26]. The properties of the

1DPC structures make them easy to be engineered in order to work at any desired wavelength and to detect analytes over a large dynamic range.

In Chapter 2, a general introduction to surface waves on multilayer dielectric structures is presented. After a brief introduction on layered dielectric structure, the effective transfer matrix method, used to simulate 1DPCs, is presented giving the governing principles for 1DPCoptimization. Then, a numerical characterization of the surface electromagnetic mode (BSW), the monitoring of the resonance shift, and how the electromagnetic field can be shaped and confined at the interface are discussed. Moreover, a description of fluorescence emission in presence of 1DPCs is illustrated and simulated, taking into account all possible experimental variables. The effects of the experimental parameters on the 1DPC sensor are comprehensively investigated and analyzed by means of simulations in order to obtain an optimized 1DPC structure.

Chapter 3 is fully devoted to the description of optical set-ups used in this work. In particular, the results are obtained on two different platforms operating under the same principle and making use of similar optical configurations.

In Chapter 4, details on the 1DPC fabrication technique and dielectric materials used are given. The optimized 1DPC structure is then characterized and tested, assessing the overall performances of the sensor. In the end, an alternative coating technology based on hydrogenated silicon nitride 1DPCs are presented and tested.

Chapter 5 is focused on the functionalization strategies adopted to tailor the 1DPC surface. In this work, two main strategies are considered. The main route is based on APTES-glutaraldehyde modification while the second approach makes use of a thin polymeric film of poly-acrylic acid as a functional layer.

In Chapter 6, the 1DPC biochips are used for label-free and fluorescence biomolecular detection, including sensitivity characterization, surface functionalization, binding experiments design and execution, and results analysis. The first part is focused on the early detection of colorectal cancer biomarkers such as Angiopoietin 2 (Ang-2) either using glutaraldehyde and polymer thin film functionalization chemistry. In the second part, a systematic study on breast cancer biomarkers (ERBB2) in cell lysates is performed. A detailed analysis of the results (measuring control negative cell lysates) validates the 1DPC biosensors in pre-clinical environment. Future perspectives, further developments and boundary activities are presented in Chapter 7.

CHAPTER 2

General properties of Bloch surface waves sustained by 1D photonic crystal

Among novel possibilities for the control of electromagnetic phenomena, photonic crystals are considered as an emerging technology in sensing applications. In particular, one dimensional photonic crystals are periodically structured media, constituted by depositing dielectric materials with different geometries. These structures possess photonic bandgaps in which light can or cannot propagate depending on the incident radiation characteristics. Under certain conditions, the electromagnetic field can be re-shaped and localized through the presence of the 1DPC itself. With this purpose, the propagation theory of optical waves in layered media is presented introducing the transfer matrix method (TMM). Then, a systematical study of 1DPC structures and an optimization strategy are described in details by means electromagnetic simulations. In conclusion, a series of simulations on the interaction of fluorescent dye molecules with a system where the electromagnetic field is strongly confined are presented.

2.1 TRANSFER MATRIX METHOD FORMULATION

A multilayer structure can be regarded as an optical system with one input and one output port. Thus, a transfer matrix $\boldsymbol{T}$ can be associated to the system in order to relate the incident and reflected waves at the input port with the incident and reflected waves at the output port. The calculation algorithm adopted in this dissertation is based on the transfer matrix method (TMM). This model describes the relationship between the amplitude of a plane wave at the input and output ports of multilayer structure.

In Figure 2.1 it is shown the schematic diagram of a dielectric multilayer structure. In order to connect the output fields $(E_F(x_{N-1}^+), E_B(x_{N-1}^+))$ with the input fields $(E_F(x_0^-), E_B(x_0^-))$, the multilayer stack can be considered as a cascaded system of interfaces and layers, with an

interface matrix $\boldsymbol{T}_{i,j}$ between two layers (i and j) and a propagation matrix $\boldsymbol{T}_j$ connecting the beginning and the end within the layer j, respectively.

The normal to the interface planes (x-axis direction) and the wave vector of the incident plane wave define a plane, the so called incidence plane, whereas the z-axis belongs to this plane but is orthogonal to the x-axis. This assumption makes that, the y-axis is defined and the wave vector lies in the (x,z)-plane: its y-component is zero, $k_y = 0$. The multilayer structure in this coordinate system is depicted in Fig. 2.1.

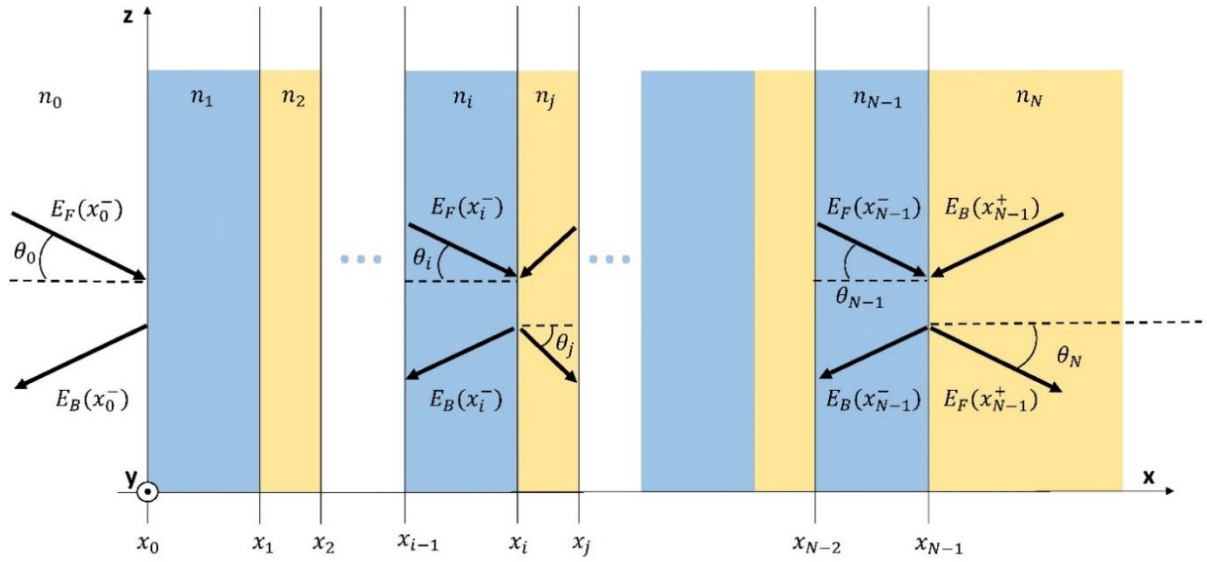

Figure 2.1 – Dielectric multilayer structure.

In this case, the problem can be solved separately in two orthogonal polarizations. In order to solve easily the problem, we can address the propagation of TE wave (s-polarization) and TM wave (p-polarization) with E and H parallel to the multilayer interfaces, respectively (Fig. 2.2). In the following calculations, the two problems (for TE and TM) differ only in the polarization dependent reflection and transmission coefficients.

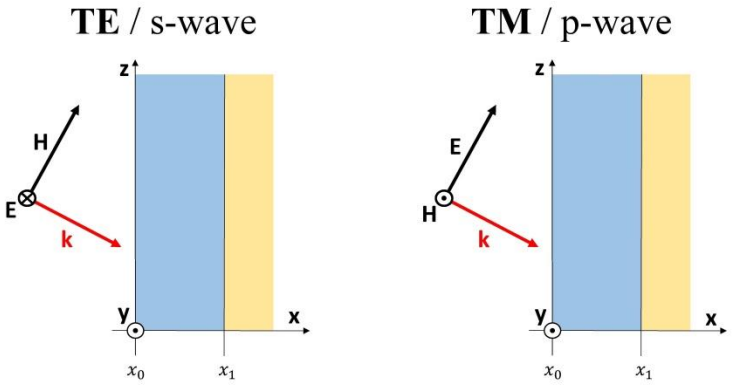

Figure 2.2 – Polarizations of the incident light with respect to the 1DPC surface.

Therefore, if one considers one polarization (TE or TM), the electric field is fully described by its amplitude E(x,y,z). In each layer, all contributions to the forward propagating wave (in the direction of increasing x) have the same direction and thus form one plane wave. The same consideration can be made for the backward propagating wave (towards decreasing x). The total field in the i-th layer an thus be expressed as follows:

$$E(x,y,z) = A_F e^{-j(k_{x,i}\,x + k_z\,z)} + A_B e^{-j(-k_{x,i}\,x + k_z\,z)} \tag{2.1}$$

$$= A_F e^{-jk_{x,i}\,x}\, e^{-jk_z\,z} + A_B e^{+jk_{x,i}\,x}\, e^{-jk_z\,z}$$

$$= E(x)_F\, e^{-jk_z\,z} + E(x)_B\, e^{-jk_z\,z}$$

where $k_{x,i}$is the x-component of $\boldsymbol{k_i}$ in the i-th layer:

$$k_{x,i} = [(n_i k_0)^2 - k_z^2]^{1/2} \quad , \qquad i = 0, 1, 2, 3 \ldots, N \tag{2.2}$$

and $k_0 = (\omega/c)$. Due to boundary conditions that relate the field amplitudes of the incident, reflected and transmitted wave at the interfaces, k_z remains constant.

When working with lossless media and in the absence of total internal reflection (TIR), $k_{x,i}$ can be related to the ray angle θ_i (see Fig.2.1) in the following way:

$$k_{x,i} = n_i k_0 \cos\theta_i \tag{2.3}$$

Nevertheless, dielectrics can show a non-zero extinction coefficient giving $Im(n_i) \neq 0$, or have a situation in which $k_z > n_i k_0$. The first case corresponds to wave propagation in a lossy medium, the second to incident angles that are larger than the critical angle for total internal reflection (TIR condition). When TIR occurs, the electric field vector decreases exponentially in the x-direction and attenuation occurs within a distance of $1/q$, where q is defined as:

$$q_i = [k_z^2 - (n_i k_0^2)]^{1/2} \quad , \qquad i = 0, 1, 2, 3 \ldots, N \tag{2.4}$$

In that case, the Eq.2.1 is an evanescent wave that propagates parallel to the multilayer's interfaces (in the z direction). For a given z value, the whole transfer matrix $\boldsymbol{T}_{0N}$ relates the complex amplitudes E_F and E_B just before and just behind the first and the last interface of the multilayer stack:

$$\begin{bmatrix} E_F(x_0^-) \\ E_B(x_0^-) \end{bmatrix} = \boldsymbol{T}_{0N} \begin{bmatrix} E_F(x_{N-1}^+) \\ E_B(x_{N-1}^+) \end{bmatrix} = \begin{bmatrix} T_{0N}^{11} & T_{0N}^{12} \\ T_{0N}^{21} & T_{0N}^{22} \end{bmatrix} \begin{bmatrix} E_F(x_{N-1}^+) \\ E_B(x_{N-1}^+) \end{bmatrix} \tag{2.5}$$

To build the complete transfer matrix, individual transfer matrices for the wave transmission through an interface and the propagation through a single layer have to be evaluated. We start with the transfer matrix for wave transmission through an interface. Consider the interface between the layer i and the layer j (Fig. 2.1). Due to boundary conditions, for a given z, the amplitudes of the forward and backward propagating waves just before and just behind the interface are related in the following way:

$$\begin{bmatrix} E_F(x_i^+) \\ E_B(x_i^-) \end{bmatrix} = \begin{bmatrix} t_{ij} & r_{ij} \\ r_{ji} & t_{ji} \end{bmatrix} \begin{bmatrix} E_F(x_i^-) \\ E_B(x_i^+) \end{bmatrix} \tag{2.6}$$

where $t_{ij,ji}$ and $r_{ij,ji}$ are the complex Fresnel reflection and transmission coefficients in the case of single incident wave. This is actually the scattering matrix description of the interface between two layers. For the TE-polarization, the Fresnel coefficients are given by:

$$r_{ij} = \frac{E_B(x_i^-)}{E_F(x_i^-)} = \frac{k_x^i - k_x^j}{k_x^i + k_x^j}$$

$$t_{ij} = \frac{E_F(x_i^+)}{E_F(x_i^-)} = 1 + r_{ij} = \frac{2k_x^i}{k_x^i + k_x^j}$$

and in the TM-polarization case by:

$$r_{ij} = \frac{E_B(x_i^-)}{E_F(x_i^-)} = \frac{n_i^2 k_x^j - n_j^2 k_x^i}{n_i^2 k_x^j + n_j^2 k_x^i}$$

$$t_{ij} = \frac{E_F(x_i^+)}{E_F(x_i^-)} = \frac{n_i}{n_j}\left(1 + r_{ij}\right)$$

Alternatively, the Fresnel coefficients can be described as a function of the refractive indices n_i, n_j and ray angles θ_i, θ_j, for the TE-polarization:

$$r_{ij} = \frac{E_B(x_i^-)}{E_F(x_i^-)} = \frac{n_i \cos\theta_i - n_j \cos\theta_j}{n_i \cos\theta_i + n_j \cos\theta_j}$$

$$t_{ij} = \frac{E_F(x_i^+)}{E_F(x_i^-)} = \left(1 + r_{ij}\right) = \frac{2n_i \cos\theta_i}{n_i \cos\theta_i + n_j \cos\theta_j}$$

and for the TM-polarization:

$$r_{ij} = \frac{E_B(x_i^-)}{E_F(x_i^-)} = \frac{n_j \cos\theta_i - n_i \cos\theta_j}{n_j \cos\theta_i + n_i \cos\theta_j}$$

$$t_{ij} = \frac{E_F(x_i^+)}{E_F(x_i^-)} = \frac{n_i}{n_j}\left(1 + r_{ij}\right) = \frac{2n_i \cos\theta_i}{n_j \cos\theta_i + n_i \cos\theta_j}$$

These latter permit to rewrite Eq.(2.6) as follows:

$$\begin{bmatrix} E_F(x_i^-) \\ E_B(x_i^-) \end{bmatrix} = \begin{bmatrix} \frac{1}{t_{ij}} & -\frac{r_{ji}}{t_{ij}} \\ \frac{r_{ij}}{t_{ij}} & t_{ji} - \frac{r_{ij}}{t_{ij}} r_{ji} \end{bmatrix} \begin{bmatrix} E_F(x_i^+) \\ E_B(x_i^+) \end{bmatrix} \tag{2.7}$$

and making use of the symmetry relations of the Fresnel coefficients, the Eq.(2.7) becomes:

$$\begin{bmatrix} E_F(x_i^-) \\ E_B(x_i^-) \end{bmatrix} = \frac{1}{t_{ij}} \begin{bmatrix} 1 & r_{ij} \\ r_{ij} & 1 \end{bmatrix} \begin{bmatrix} E_F(x_i^+) \\ E_B(x_i^+) \end{bmatrix} \tag{2.8}$$

where for symmetry one can utilize $r_{ij} = -r_{ji}$ and $t_{ji}t_{ij} - r_{ij}r_{ji} = 1$.

Therefore, the transfer matrix $\boldsymbol{T}_{ij}$ for wave propagation through the interface between layers i and j can be expressed as follows:

$$\boldsymbol{T}_{ij} = \frac{1}{t_{ij}} \begin{bmatrix} 1 & r_{ij} \\ r_{ij} & 1 \end{bmatrix} \tag{2.9}$$

As a further step, it is required to write the transfer matrix for wave propagation through a layer. If one considers the i-th layer, for a given z, the amplitudes of the forward and backward propagating waves just before and just behind the interfaces of the adjacent layers are related in the following way:

$$E_F(x_i^-) = E_F(x_{i-1}^+) e^{-k_{x,i}\, d_i} \tag{2.10}$$

$$E_B(x_{i-1}^+) = E_B(x_i^-) e^{-k_{x,i}\, d_i} \tag{2.11}$$

with d_i the thickness of layer i. Thus, the transfer matrix $\boldsymbol{T}_i$ for wave propagation through layer is given by:

$$\boldsymbol{T}_i = \begin{bmatrix} e^{j\varphi_i} & 0 \\ 0 & e^{-j\varphi_i} \end{bmatrix} \tag{2.12}$$

in which we defined, $\varphi_i = k_i\, d_i$ which in general is a complex quantity. In a lossless medium and in the absence of total internal reflection, $\varphi_i = k_i\, d_i$ is a real quantity:

$$\varphi_i = k_{x,i}\, d_i = \frac{2\pi}{\lambda_0} n_i d_i \cos\theta_i \tag{2.13}$$

In conclusion, to build the complete transfer matrix for the wave propagation through the layered medium, one can now multiply all individual transfer matrices.

$$\begin{bmatrix} E_F(x_0^-) \\ E_B(x_0^-) \end{bmatrix} = \boldsymbol{T}_{0N} \begin{bmatrix} E_F(x_{N-1}^+) \\ E_B(x_{N-1}^+) \end{bmatrix} = \begin{bmatrix} T_{0N}^{11} & T_{0N}^{12} \\ T_{0N}^{21} & T_{0N}^{22} \end{bmatrix} \begin{bmatrix} E_F(x_{N-1}^+) \\ E_B(x_{N-1}^+) \end{bmatrix} \tag{2.14}$$

where:

$$\boldsymbol{T}_{0N} = \boldsymbol{T}_{01}\boldsymbol{T}_1\boldsymbol{T}_{12}\boldsymbol{T}_2 \dots \boldsymbol{T}_{(N-1)}\boldsymbol{T}_{(N-1)N} \tag{2.15}$$

The Eq.(2.14) is known as the matrix formulation for wave propagation through multilayer structures.

2.2 BLOCH WAVES AND BAND STRUCTURES

It is important to notice that the electromagnetic model developed until this point is general and can be applied to a large number of multilayer structures. In particular, for a periodically stratified medium, the fields can be considered equivalent to a one-dimensional lattice which is invariant under a lattice characteristic translation (lattice constant). In this case, the translational symmetry is in the x-axis direction and the lattice translation operator is defined by: LTO(x) = x + pΛ, where p is an integer.

According to the Floquet's theorem, a wave propagating in a periodic medium has to satisfy:

$$\mathrm{E}(\mathrm{x} + \Lambda) = \mathrm{E}(\mathrm{x})\, e^{jK_B\Lambda} \tag{2.16}$$

where the constant K_B is known as the Bloch wavevector and Λ is the period of the layered structure. A similar equation holds for the magnetic field H(x). Thus, the problem is that of determining K_B and E(x) in terms of column vector representation. From Eq.(2.1), the periodic condition Eq.(2.16) for the Bloch wave can be simply obtained:

$$\begin{pmatrix} \mathrm{E_F}(x_N) \\ \mathrm{E_B}(x_N) \end{pmatrix} = \mathrm{e}^{\mathrm{j}K_B\Lambda} \begin{pmatrix} \mathrm{E_F}(x_{N-2}) \\ \mathrm{E_B}(x_{N-2}) \end{pmatrix} \tag{2.17}$$

It follows from Eq.(2.5) and Eq.(2.17) that the column vector of the Bloch wave satisfies the following eigenvalue problem:

$$\begin{pmatrix} T_{N,N-2}^{11} & T_{N,N-2}^{12} \\ T_{N,N-2}^{21} & T_{N,N-2}^{22} \end{pmatrix} \begin{pmatrix} \mathrm{E_F}(x_N) \\ \mathrm{E_B}(x_N) \end{pmatrix} = \mathrm{e}^{-\mathrm{j}K_B\Lambda} \begin{pmatrix} \mathrm{E_F}(x_N) \\ \mathrm{E_B}(x_N) \end{pmatrix} \tag{2.18}$$

where $\boldsymbol{T}_{\mathrm{N,\,N\text{-}2}}$ can be written as follows

$$\begin{pmatrix} \mathrm{E_F}(x_{N-2}) \\ \mathrm{E_B}(x_{N-2}) \end{pmatrix} = \begin{pmatrix} T_{N,N-2}^{11} & T_{N,N-2}^{12} \\ T_{N,N-2}^{21} & T_{N,N-2}^{22} \end{pmatrix} \begin{pmatrix} \mathrm{E_F}(x_N) \\ \mathrm{E_B}(x_N) \end{pmatrix} \tag{2.19}$$

However, the trace of the translation matrix (Tr($\boldsymbol{T}_{\mathrm{N,\,N\text{-}2}}$)) is directly related to the band structure of the stratified periodic medium. Thus, the eigenvalues of the translation matrix are given by:

$$\mathrm{e}^{-\mathrm{j}K_B\Lambda} = \frac{1}{2}\mathrm{Tr}\,(T_{N,N-2}) \pm \left\{\left[\frac{1}{2}\mathrm{Tr}\,(T_{N,N-2})\right]^2 - 1\right\}^{1/2} \tag{2.20}$$

The eigenvectors that correspond to the eigenvalues Eq.(2.20) are obtained from Eq.(2.18) and are:

$$\begin{pmatrix} \mathrm{E_F}(x_0) \\ \mathrm{E_B}(x_0) \end{pmatrix} = \begin{pmatrix} T_{N,N-2}^{12} \\ \mathrm{e}^{-\mathrm{j}K_B\Lambda} - T_{N,N-2}^{11} \end{pmatrix} \tag{2.21}$$

times any arbitrary constant. The Bloch waves, which result from Eq.(2.21), can be considered as the eigenvectors of the translation matrix with eigenvalues $\mathrm{e}^{\mathrm{j}K_B\Lambda}$ given by Eq.(2.20). The two eigenvalues in Eq.(2.20) are the inverse of each other, since the translation matrix is unimodular. Eq.(2.20) gives the dispersion relation between ω, k_z , and K_B for the Bloch wave function:

$$K_B(k_z, \omega) = \cos^{-1}\left[\frac{1}{2}\mathrm{Tr}\left(T_{N,N-2}\right)\right] \tag{2.22}$$

In other words, for each Bloch wavevector K_B one can find a dispersion relation ω(k_z). If all possible dispersion relations are plotted on the same graph one obtains the so-called band-diagram. The points in the graph where $|1/2\ \mathrm{Tr}\ (T_{N,N-2})| < 1$ correspond to real K_B and thus to propagating Bloch waves, when $|1/2\ \mathrm{Tr}\ (T_{N,N-2})| > 1$, $K_B = (m\pi/\Lambda) + jK_i$ and has an imaginary K_i so that the Bloch wave is evanescent (frequency regions for which propagation is inhibited). The latter case represent the so called "forbidden bands" of the periodic medium. The band edges are the regime in which: $|1/2\ \mathrm{Tr}\ (T_{N,N-2})| = 1$. An example is shown in Fig. 2.3 where the shaded areas correspond to allowed bands for which propagation through the crystal is possible. However, for a 1DPC there is no complete bandgap, i.e. there are no frequencies for which propagation is inhibited in all directions. In particular, when a wave propagating in vacuum is directed onto the photonic crystal, only modes with k_z values smaller than $k = \omega/c$ can be

excited. The vacuum light-lines (dashed lines) are indicated in the Fig.2.3 and one can find complete frequency bandgaps inside the region $k_z < k$. In this frequency range, the photonic crystal acts a perfect mirror.

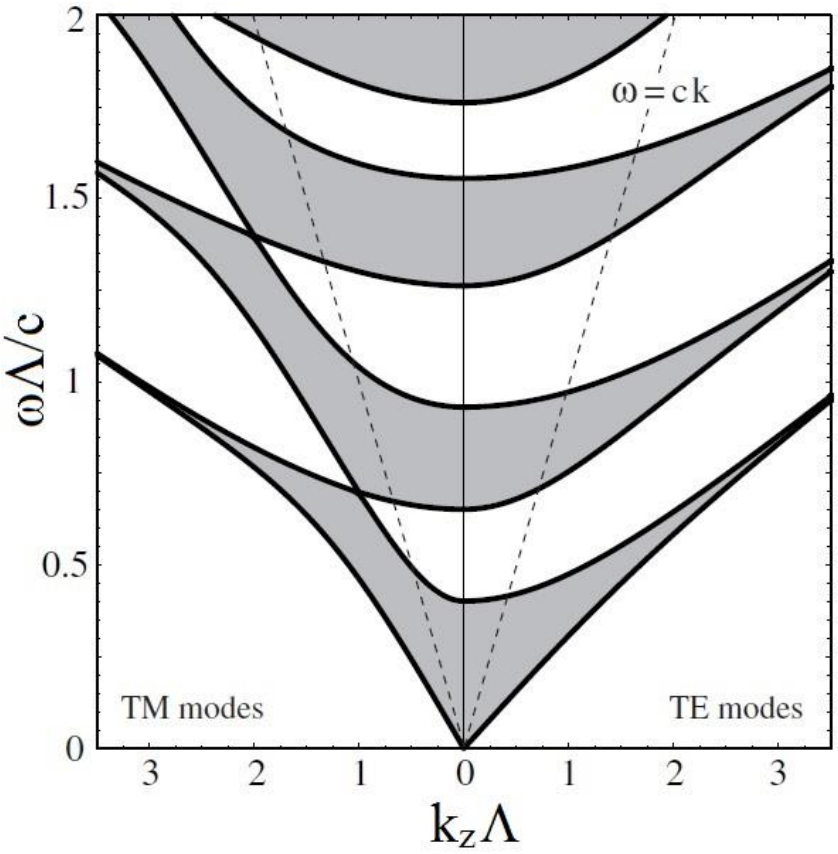

Figure 2.3 – Band-diagram for a one-dimensional photonic crystal. The dark zones are the allowed bands. The diagram represents both TE and TM modes. For a1DPC, there are no complete bandgaps, i.e. there are no frequencies for which propagation is inhibited in all direction. Values used: n_1=1.53 (SiO_2), n_2=4.23 (InSb) [27].

The band structures for a typical stratified periodic medium, as obtained from Eq.(2.14), are shown in Fig.2.3 for TE and TM waves, respectively. It has to be noticed that the TM "forbidden" bands shrink to zero when: $k_z = (\omega/c)\, n_2 \sin\theta_{BREW}$, where θ_{BREW} it the Brewster angle, since at this angle the incident and reflected waves are decoupled.

2.3 ELECTROMAGNETIC BLOCH SURFACE WAVES

A surface electromagnetic wave is a wave associated to an interface between two semi-infinite systems. The presence of surface states at the interface of multilayer structure can be explained considering that at a given frequency, there are regions of k_z, for which K_B is complex and $K_B = m\pi/\Lambda \pm jK_i$. As already introduced above, in such regions, propagation through the structure is not allowed (forbidden bands), obtaining an evanescent field profile. For a semi-infinite periodic medium, the exponentially damped solution is a possible solution near the interface and the field envelope decays as $e^{-jK_i x}$; where x is the distance from the considered interface. To study the properties of the surface modes it may be considered a semi-infinite periodic multilayer dielectric medium consisting of alternating layers of different indices of refraction. The geometrical parameters and refractive index distribution are given in Fig. 2.4 (where $n_2 > n_1 > n_e$.).

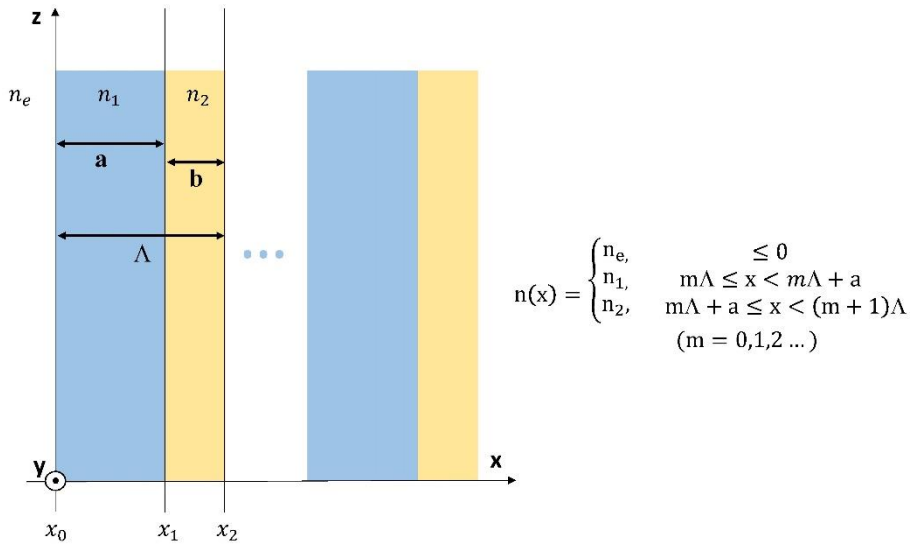

Figure 2.4 – Semi-infinite periodic structure made of two different materials with period Λ.

Let us consider the case of TE surface modes where the electric field is polarized in the y direction (see in scheme of Fig. 2.2). The electric field distribution (TE) obeys the wave equation:

$$\frac{\partial^2 E_y}{\partial z^2} + \frac{\partial^2 E_y}{\partial x^2} + \left(\frac{\omega}{c}\right)^2 n^2(x) E_y = 0 \qquad (2.23)$$

Assuming $E_y(x, y, z) = E(x)e^{jk_z z}$ the wave equation becomes:

$$\frac{\partial^2 \mathrm{E(x)}}{\partial \mathrm{x}^2} + \left(\frac{\omega^2}{\mathrm{c}^2}\,\mathrm{n}^2(\mathrm{x}) - {k_z}^2\right)\mathrm{E(x)} = 0 \tag{2.24}$$

The solution of Eq (2.24) is:

$$\mathrm{E(x)} = \begin{cases} \alpha \mathrm{e}^{\mathrm{q_e x}}, & \mathrm{x} \le 0, \\ \mathrm{E}_{K_B}(\mathrm{x})\mathrm{e}^{\mathrm{j}K_B \mathrm{x}}, & \mathrm{x} \ge 0. \end{cases} \tag{2.25}$$

where α is a numerical factor and q_e is given by:

$$\mathrm{q_e} = \left\{ {k_z}^2 - \left[\frac{\omega}{\mathrm{c}}\mathrm{n_e}\right]^2 \right\}^{1/2} \tag{2.26}$$

In order to be a guided wave, the constant K_B in Eq.(2.25) must be complex so that the field decays exponentially for large x values. This is possible only when the propagating conditions in the periodic medium correspond to a "forbidden" band. Another condition is that E(x) and its x derivative be continuous at the interface with medium e. This gives the condition for surface modes:

$$\mathrm{q_e} = \frac{\mathrm{q}(\mathrm{e}^{-\mathrm{j}K_B \Lambda} - T_{e,N}^{11} - T_{e,N}^{12})}{(\mathrm{e}^{-\mathrm{j}K_B \Lambda} - T_{e,N}^{11} + T_{e,N}^{12})} \tag{2.27}$$

It is evident that the energy is more or less concentrated in the first few periods of the semi-infinite periodic medium. It can easily be shown that:

$$\frac{W_I}{W_{TOT}} = (1 - \mathrm{e}^{-2\mathrm{K_i}\Lambda}) \tag{2.28}$$

where K_i is the imaginary part of K_B. The W_I, W_{TOT} are the energies in the first period and in the whole structure, respectively. The field distribution in each period is similar to that of the distribution in the preceding period except for the amplitude that results reduced by a factor of $(-1)^{\mathrm{m}}\mathrm{e}^{-\mathrm{j}\mathrm{K_i}\Lambda}$, where m is the integer corresponding to the m-th forbidden gap [2].

In this case the fundamental surface wave has the highest K_i that means higher degree of localization. Therefore, the fundamental surface wave should be in the zero-th or the first forbidden gap. It depends on the magnitude of the index of refraction n_e. For n_e less than n_1, which is a case of practical interest (n_e is the index of refraction of air), the fundamental surface wave has a Bloch wave vector in the first forbidden gap (details in the following paragraphs).

2.4 EXCITATION OF BLOCH SURFACE WAVES

The excitation of a Bloch surface wave on a 1DPC can be attained by a coupling prism in the Kretschmann–Raether (K-R) configuration under total internal reflection conditions (TIR). In this particular configuration, a light beam passes from air into the glass prism and impinges at an angle θ with respect to the normal to the 1DPC surface, , as shown in Fig. 2.5. In order to ensure optical continuity between the prism and the 1DPC, a contact oil is added on the back-side of the substrate on which the 1DPC is deposited (glass side).

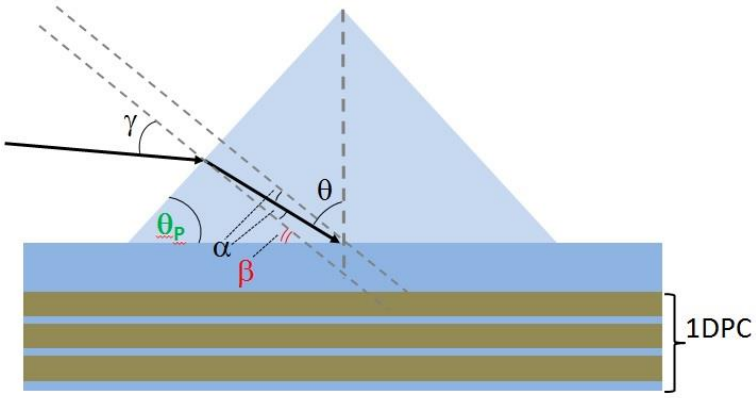

Figure 2.5 – Kretschmann–Raether configuration and angles of interest.

To guarantee the excitation and the propagation of the BSW, total internal reflection condition is needed. In order to operate with a monochromatic incident laser beam at λ and at an angle θ, the transmitted wave in the prism, according to Snell's law, is at an angle α given by:

$$n_a \sin\gamma = n_p \sin\alpha \tag{2.29}$$

where n_a and n_p are the refractive indices of the air $n_a = 1$ and the glass prism , respectively. The angle of incidence at the interface prism-substrate is:

$$\vartheta = \vartheta_p + \alpha \tag{2.30}$$

The critical angle (ϑ_L) for TIR between prism-air, is given by:

$$\vartheta_L = \arcsin\left(\frac{n_a}{n_p}\right) \tag{2.31}$$

Eq.(2.30) and Eq.(2.31), the transmission angle at the air-prism interface is obtained as follows:

$$\alpha \geq \vartheta_L - \vartheta_P = \arcsin\left(\frac{n_a}{n_p}\right) - \vartheta_P \tag{2.32}$$

By determining α, it is possible to find the values of γ, at which total internal reflection occurs. When TIR takes place, the incident light goes to an evanescent wave at the interface. Such an

evanescent wave is at the same frequency of the incident light and its amplitude decays exponentially as a function of x with a given penetration depth. Therefore, BSWs can be excited only when the propagation conditions in the periodic media correspond to a photonic bandgap. The penetration depth of this evanescent field depends on the angle and wavelength of the incident light, and on the refractive indices of the two media. Increasing the incident light angle leads to a reduced penetration depth. On the contrary, larger wavelengths lead to an increased penetration depth. In Fig. 2.6 it is represented a typical Bloch surface wave angular reflectance in TE polarization and the distribution of the electric field along the 1DPC.

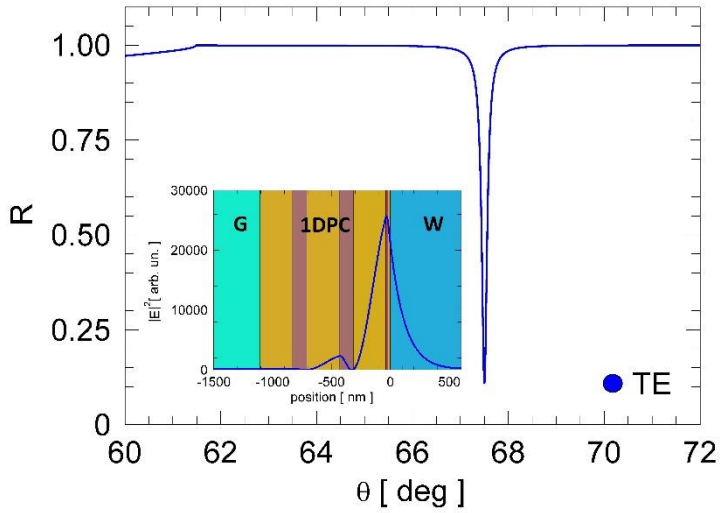

Figure 2.6 – TE polarized reflectance of a typical 1DPC used during the experimental characterization. In the inset, the electric field distributed along the multilayer structure.

2.5 OPTIMIZATION OF THE 1DPC STRUCTURE

In biosensing, there are three kinds of modulation methods to monitor the resonance mode shift and then to retrieve the information of bio-molecular interactions: angular or wavelength [7], intensity [29], and phase [30] resolved detection. In the following, I briefly report on the study on the influence of 1DPC parameters on the overall sensing performances. A more systematic and detailed description can be found in the article [25]

First, the effect of different values of the index-contrast between dielectric layers is explored when simulating the 1DPC structure, as they can give rise to high reflectivity, thus leading to a high Q resonator. For a 1DPC characterized by the same number of periods, high-index-contrast materials produce larger field intensity on the sensing surface and, thus, larger sensitivity. In the following simulations the number of periods (from N=2 to N=5), the losses

in the dielectrics (k = 5E-5) and thicknesses of the layers are kept constant; only the ratio (γ) between the real part of the refractive indices of the two 1DPC materials has been changed. With this aim, with reference to Figure 2.4, we compare three sets of dielectric materials: 1) n_1=1.474, n_2=2.16 (γ=1.46), 2) n_1=1.474, n_2=2.28 (γ=1.54) and 3) n_1=1.474, n_2=2.56 (γ=1.73). The related reflectance profiles in the K-R configuration are shown in Fig.2.7.

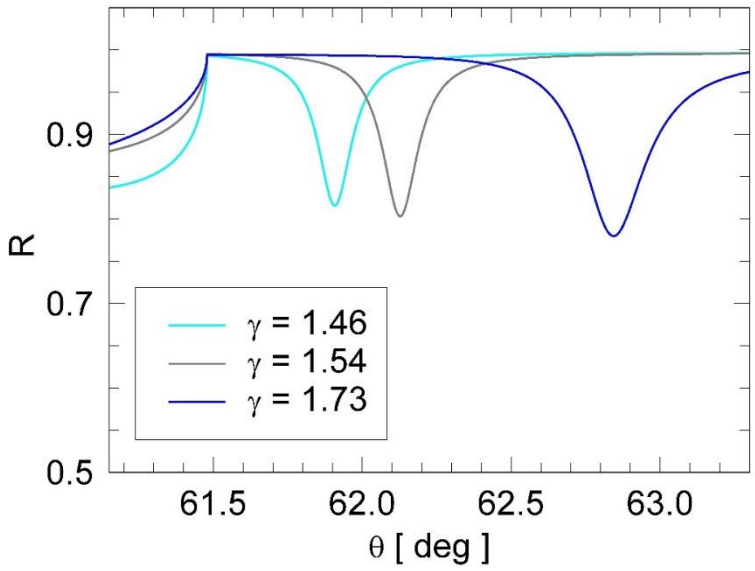

Figure 2.7: Angular reflectance profiles varying the ratio between the high and low refractive indices.

In Fig. 2.7, it is evident that increasing the contrast between refractive indices of the two layers results in a shift towards larger angles of the resonance position and in a broadening of the resonance width. The depth of the resonances seems to be invariant to the changes in the refractive index ratio between layers (slightly deeper as the ratio increases). For what concerns the field distribution, as shown in Fig. 2.8, the electric field profile changes at the 1DPC surface as a function of the ratio. In particular, the larger it is the refractive index contrast the more the field is localized at the interface. This means that the sensitivity increases with the ratio γ. It has to be noticed that there are not dramatic differences between the case γ=1.73 and γ=1.54.

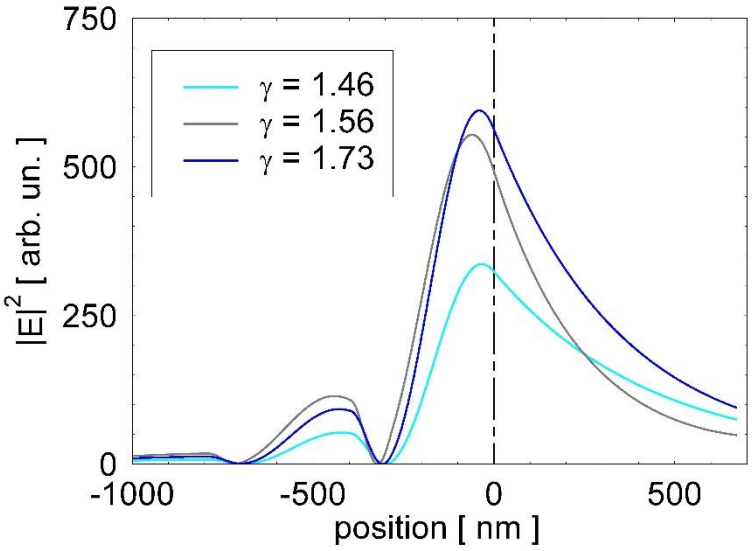

Figure 2.8 – Electric field profile (square modulus) at the 1DPC surface (dotted black line) as a function of refractive index contrast (γ).

Another important parameter when designing 1DPC is the number of periods N. In Fig. 2.9A it is shown the behavior of the reflectance dip by increasing N. It is evident from Fig. 2.9A that a larger number of periods provides a narrower and slightly shifted resonance enabling to confine more efficiently the electric field at the interface (Fig. 2.9B). Nevertheless, this is true keeping the losses (in the low refractive index materials) constants and in the range of k = 5E-6. A clear drawback in increasing the number of periods is that also the distance of the interface from the collecting prism increases.

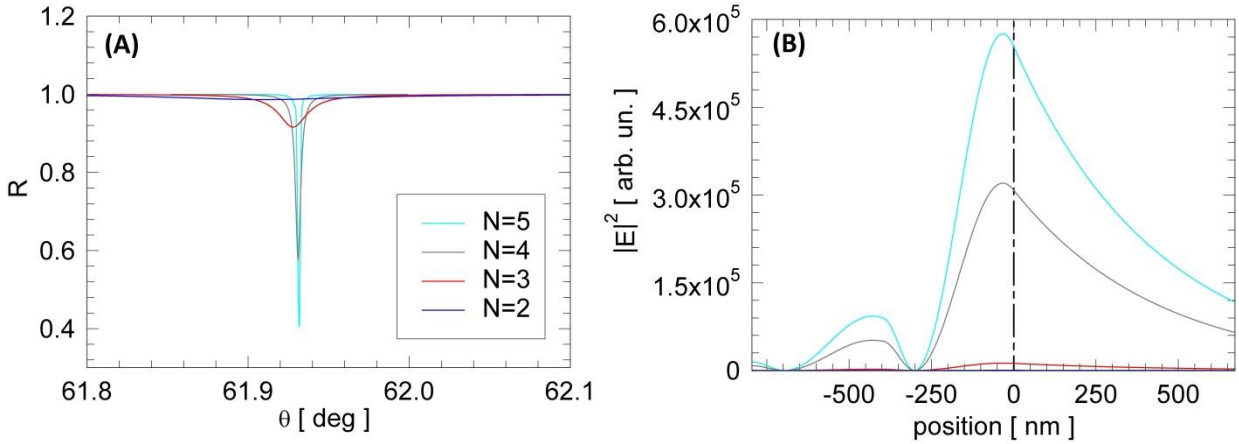

Figure 2.9: Angular reflectance profiles as a function of the number of periods N. In this case the period consists in $\Lambda = d_{SiO2} + d_{Ta2O5}$ (A); the associated electric field intensities across the interface (position = 0 nm) between 1DPC and the external medium (B). Simulation parameters: $n_{SiO2} = 1.474 + j\ 5E\text{-}6$ (d_{SiO2} =275); $n_{Ta2O5} = 2.16 + j\ 5E\text{-}5$ (d_{Ta2O5} =120 nm).

This aspect can spoil the detection efficiency in fluorescence applications, when small amount of fluorescent molecules bind the surface. In that case, the decoupling efficiency can be also compromised by the increased distance between the emitter and the decoupling system leading to a worst fluorescence detection yield. In other words, thicker structures work better in terms of sensitivity but they make the fluorescence decoupling not efficient.

Another possible drawback derives from the necessity to deposit 1DPCs on plastic substrates. Thicker multilayers imply a large stress between single layers causing delamination of the topping layers during operation in aqueous environment. This makes the deposition of 1DPCs with a high number of periods not appropriate for stable multilayers on plastic substrates. According to the previous considerations, during the doctorate period, we converged towards 1DPC designs that include high index thin layers on top of a periodic multilayer (see Fig. 2.10). The role of the high index layer is to enhance the sensitivity while keeping a low number of periods.

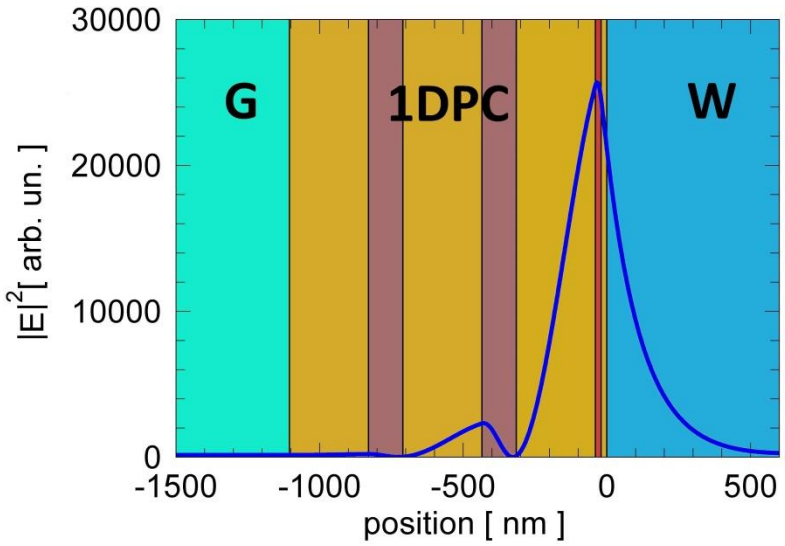

Figure 2.10 – Spatial distribution of the electric field squared within the structuture (1DPC). The simulation is performed with a BK7 glass substrate (G) and DI-water (W) as external medium.

In particular during the last part of the doctorate I made use of 1DPC with the following design. For this reason, we introduced a non-periodic 1DPC structure to better tune the sensitivity while keeping a structure with a low number of periods. Starting from the substrate side (G side in Fig. 2.10), the 1DPC is composed of a first SiO_2 matching layer that is used to improve the reliability of the subsequent high index layer. Given the small difference of the refractive index with respect to the substrate, such a layer does not play any significant optical role. The core of the 1DPC is a periodic structure with two Ta_2O_5/SiO_2 bilayers with period $\Lambda = d_{Ta2O5} + d_{SiO2}$

(n_{SiO2} = 1.474 + j 5E-6 and d_{SiO2} =275 n_{Ta2O5} = 2.16 + j 5E-5 and d_{Ta2O5} =120 nm). The 1DPC is then topped by a thin TiO_2/SiO_2 bilayer. The last SiO_2 top layer (n_{SiO2} = 1.474 + j 5E-6 and d_{SiO2} = 20 nm) is introduced to provide a suitable surface for robust chemical functionalization method via silanization approach (see in Chapter 5), whereas the thickness and absorption coefficient of the TiO_2 top layer was tuned to optimize the position of the BSW dispersion in the 1DPC forbidden band and the depth of the resonance. This leads to the choice of TiO_2 as high index layer (n_{TiO2} = 2.28 +j 1.8E-3) with a thickness of 20 nm and an absorption coefficient that matches the need of balanced losses. Moreover, the insertion of such a layer provides a considerable enhancement of the electric field at the interface with respect to the periodic case emulating the confinement produced by structures with a large number of periods. In Fig.2.11 are illustrated the two structures, periodic (without TiO_2 and SiO_2 topping layers) and non-periodic, and the electric fields at the 1DPC surface at resonance.

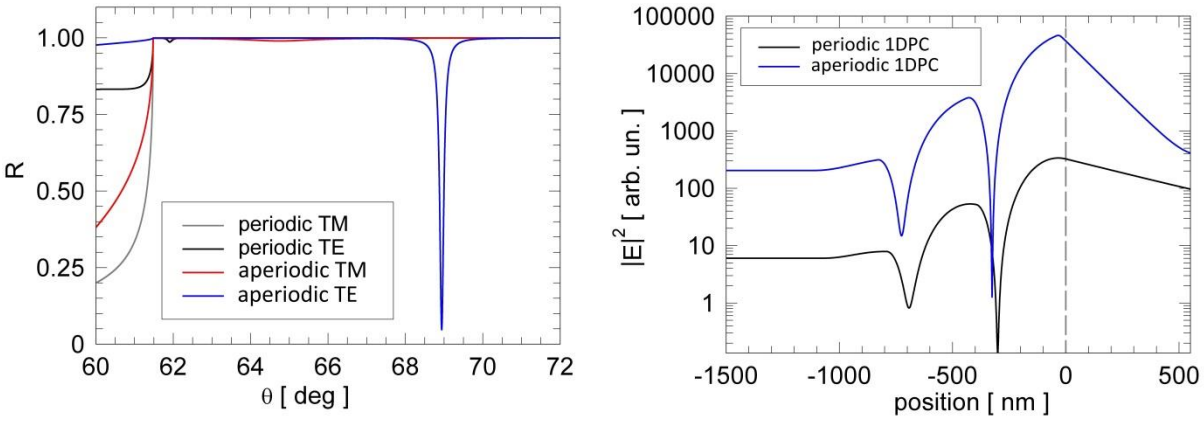

Figure 2.11 – Reflectance profiles and field distributions for periodic and quasi-periodic 1DPC. Simulation parameters for the periodic structure: n_{SiO2} = 1.474 + j 5E-6 (d_{SiO2} =275 and 20 nm); n_{Ta2O5} = 2.16 + j 5E-5 (d_{Ta2O5} =120 nm); n_{TiO2} = 2.28 +j 1.8E-3 (d_{TiO2} =20 nm).. Simulation parameters for the non-periodic structure: n_{SiO2} = 1.474 + j 5E-6 (d_{SiO2} =275 and 20 nm); n_{Ta2O5} = 2.16 + j 5E-5 (d_{Ta2O5} =120 nm); n_{TiO2} = 2.28 +j 1.8E-3 (d_{TiO2} =20 nm). All the simulations are performed at λ= 670 nm

As clearly shown in Fig. 2.11, the TiO_2 thin layer acts as a guiding layer for the surface modes improving the depth of the resonance and enhancing the field confinement at the surface, i.e. the sensitivity. We selected TiO_2 instead of Ta_2O_5 for technological reasons. Absorption losses in TiO_2 can be inserted more easily with respect to Ta_2O_5 thin oxide layers. The optical properties of this TiO_2 thin film were extensively studied to optimize the overall performances of the 1DPC.

In particular, we focused on the study of absorption losses in TiO_2 layer. In Figure 2.12 are shown different reflectance profiles as a function of the TiO_2 extinction coefficient. Starting from a value k for the losses of 5E-5 and increasing such a parameter, the resonance becomes deeper until a critical k value (k=0.0018). After this value the resonance, when further increasing k, recovers to its initial condition broaden features (light blue curve in Fig. 2.12). The optimum condition, in terms of width and depth, is observed in the range of k = (0.0015 – 0.002).

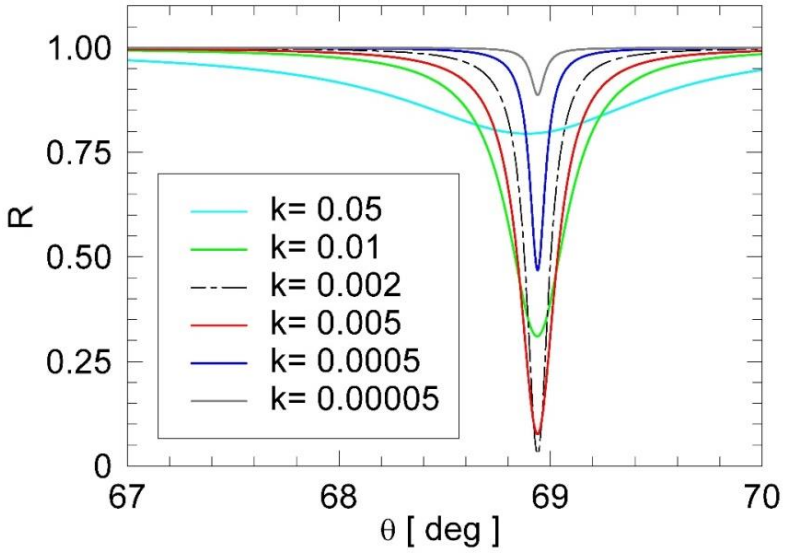

Figure 2.12 – Reflectance changes as a function of the absorption losses (k) in TiO_2 thin layer.

In order to compare the periodic and non-periodic structures, the 1DPC band diagram for TE and TM polarizations was numerically calculated with the TMM. First, we focus on the photonic properties of the periodic 1DPC reported above. In Fig. 2.13, where k_z is the transverse component of the wavevector and ω is the angular frequency, we show the calculated photonic band diagrams for an infinite 1DPC with the same d_{Ta2O5} and d_{SiO2}. Such diagrams are invariant with respect to Λ, provided the ratio d_{Ta2O5} / d_{SiO2} is constant. The permitted and forbidden bands are filled with grey and white colors, respectively, and the dispersion of light in the external medium (LL) is plotted as a black dashed curve. The diagram is calculated by means of an iterative plane wave eigen-solver method [31].

As shown in Fig.2.11, the 1DPC can sustain a BSW confined at the truncation interface, between the 1DPC and the external medium, whose dispersion lays in a forbidden band of the 1DPC [23]. In Fig. 2.12 (blue curve), we show the numerically calculated dispersions of such BSW when the top bilayer is absent, for the TE and TM polarizations. The dispersions are located beyond the light line (LL), confirming that the BSW can be excited only in a TIR

configuration. For the non-periodic 1DPC (red curve in Fig. 2.13), the dispersion of the BSW obtained when the top bilayer is present, is calculated by the same method. The effect of the dielectric load of such TiO_2/SiO_2 bilayer is to shift the BSW dispersion towards larger k_z values. For the TE polarization, this has the effect to bring the dispersion at the center of the forbidden band and far from the LL (see also reflectance profiles in Fig. 2.11), increasing the field localization of the BSW (see Fig .2.11) at the truncation interface. At the chosen λ_0 = 670 nm that is used in the experimental characterizations, whose corresponding normalized angular frequency is marked with a horizontal line in Fig. 2.13 (green dashed line), we therefore obtain two BSW, one TE and one TM.

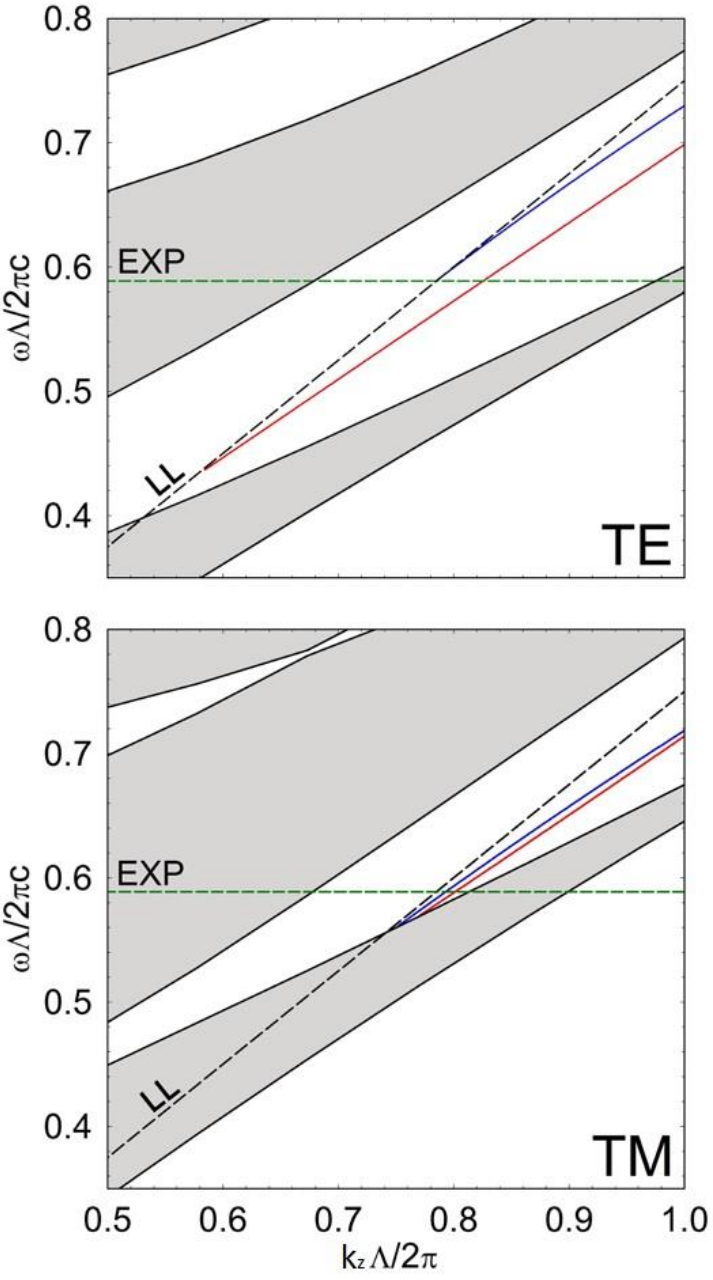

Figure 2.13 - Photonic bands for a periodic and infinite 1DPC with d_{SiO2} = 275 nm and d_{Ta2O5} = 120

nm, for the TE and TM polarizations. The permitted and forbidden bands are filled with grey and white colors, respectively. The light line in the external medium (LL) is plotted with a black dashed line. The dispersion of the BSW for the finite 1DPC are shown either for periodic (blue) and quasi-periodic (red) are plotted. The horizontal green dashed line corresponds to the wavelength used in the experiments λ_0 = 670 nm.

The effect of both SiO_2 and TiO_2 top layers on the properties of the TE BSW was taken into account when designing the 1DPC. The optimization procedure to design the 1DPC (pursued in this dissertation work and in reference [32]) maximizes the sensitivity S of the BSW resonance angle θ with respect to the change of the thickness h of a biological adlayer, with n_{BIO} = 1.42, bound at the biochip surface (S_S). As already discussed in Section 1, the performances of the optimized biochips can be characterized in terms of sensitivity and the figure of merit (in Chapter 4).

2.6 FLUORESCENCE OPERATION

In this paragraph we describe the fluorescence operation of the 1DPC focusing the attention on the emission pattern of fluorescent molecules anchored at the surface. The fluorescence simulations are obtained by means a rigorous electrodynamic approach applying dyadic Green's functions to describe the effects classically developed at Fraunhofer IOF [33]. As briefly introduced above, a 1DPC structure can also modify the emission properties of a dye close to the sensing surface. This occurs when an emitting dye interacts with a structure with confined density of state. In the present case, the 1DPC acts as a directional antenna channeling the emitted light into same angular window used for label-free investigation. Through the same coupling prism we are able to decouple the emitted light and collect an angular spectrum of the dye via TE and/or TM modes. In general, this is true for all the surface modes sustained from the 1DPC structure providing a replica of the dye emission spectra (λ_{EM}).The role of the 1DPC is dual. First, the fluorescent molecules bound onto 1DPC sensitive area can be resonantly excited at the surface of the biosensor in order to match the maximum of the dye absorption spectrum (λ_{EXC}). The resonant excitation through the 1DPC stack permits to transfer the maximum energy to the dye exploiting the resonant condition in light absorption [29]. The latter condition allows to increase the energy delivered to the dye at λ_{EXC} thus excite more efficiently the fluorescent molecule. Secondly, the re-direction of the fluorescence signal emitted can be evaluated through the dispersion relation of the 1DPC obtaining an emission

pattern as a replica of the fluorescence spectrum of selected dye.

This fluorescence emission pattern can be calculated assuming that the dye labels in the emitting layer can be modelled as rod-like dipole emitters with an isotropic orientation.

The orientation distribution of the ensemble of dipoles can be described by means of the normalised distribution function $f_0(\theta,\varphi)$, where:

$$f_0(\theta,\varphi) = \frac{1}{4\pi} \tag{2.33}$$

In real applications, due to the fact that they are covalently bound at the surface, it may be assumed that their orientation cannot change in time; consequently the orientational distribution of the excited dipoles coincides with that of the emitting dipoles. With reference to Figure 2.14 the excitation is carried out with a beam focused in the (x,z) incidence plane and polarised along the y direction. If the polarisation of the fluorescence excitation beam is along the y direction (TE polarisation for the 1DPC) the orientational distribution of the excited (emitting) molecules under stationary conditions (CW excitation) can be calculated according to the following considerations.

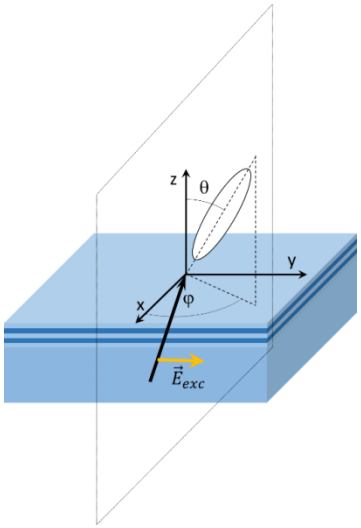

Figure 2.14 – Fluorescence excitation configuration and system of coordinates for the emitter orientation

According to Figure 2.14, a generic dipole in the distribution is excited according to an absorbed power proportional to:

$$P_{abs}(\theta,\varphi) \propto \left|\vec{\mu}\cdot\vec{E}_{exc}\right|^2 \tag{2.34}$$

where $\vec{\mu}$ is the transition dipole moment. In turn, $P_{abs}(\theta,\varphi)$ can be written as:

$$P_{abs}(\theta,\varphi) \propto \mu^2 I_{exc} \sin^2(\theta)\sin^2(\varphi) \tag{2.35}$$

It is possible then to calculate the average transition power over the isotropic distribution of the dye labels and get:

$$\begin{aligned} \overline{P}_{abs} &\propto \mu^2 I_{exc} \int f_0(\theta,\varphi,t)\sin^2(\theta)\sin^2(\varphi)d\Omega \\ &= \mu^2 I_{exc} \int \frac{1}{4\pi}\sin^2(\theta)\sin^2(\varphi)d\Omega = \frac{1}{3}\mu^2 I_{exc} \end{aligned} \tag{2.36}$$

Such last result states that in case of TE excitation of dye labels angularly distributed isotropically the excitation rate obtained is 1/3 of the power that we would have if the dipoles would be all oriented along the y direction. When addressing the fluorescence emission, the emitted power of each dipole is given by:

$$P_{em}(\theta,\varphi) \propto \eta\mu^2 I_{exc} \sin^2(\theta)\sin^2(\varphi) \tag{2.37}$$

where η is the quantum efficiency, related to the dipole molecule's properties and to the external environment. An emitting dipole can be then decomposed over 3 independent dipoles oriented along the x,y and z directions, emitting according to the following emitted power:

$$\begin{cases} P_{em,x}(\theta,\varphi) = P_{em}(\theta,\varphi)\sin^2(\theta)\cos^2(\varphi) \\ P_{em,y}(\theta,\varphi) = P_{em}(\theta,\varphi)\sin^2(\theta)\sin^2(\varphi) \\ P_{em,z}(\theta,\varphi) = P_{em}(\theta,\varphi)\cos^2(\theta) \end{cases} \tag{2.38}$$

The average emitted power of the three dipoles can be evaluated as follows:

$$\begin{cases} \overline{P}_{em,x} \propto \eta\mu^2 I_{exc} \int f_0(\theta,\varphi,t)\sin^4(\theta)\sin^2(\varphi)\cos^2(\varphi)d\Omega = \frac{1}{15}\eta\mu^2 I_{exc} \\ \overline{P}_{em,y} \propto \eta\mu^2 I_{exc} \int f_0(\theta,\varphi,t)\sin^4(\theta)\sin^4(\varphi)d\Omega = \frac{1}{5}\eta\mu^2 I_{exc} \\ \overline{P}_{em,z} \propto \eta\mu^2 I_{exc} \int f_0(\theta,\varphi,t)\sin^2(\theta)\cos^2(\theta)\sin^2(\varphi)d\Omega = \frac{1}{15}\eta\mu^2 I_{exc} \end{cases} \tag{2.39}$$

The total average emitted power is then given by:

$$\left\{\overline{P}_{em} = \overline{P}_{em,x} + \overline{P}_{em,y} + \overline{P}_{em,z} = \left(\frac{1}{15}+\frac{1}{5}+\frac{1}{15}\right)\eta\mu^2 I_{exc} = \frac{1}{3}\eta\mu^2 I_{exc} = \eta\overline{P}_{abs}\right. \tag{2.40}$$

Confirming that the total emitted power is given by the total absorbed power times the quantum efficiency. With reference to Fig. 2.14 the fluorescence is collected from the substrate side in

the (x,z) plane, the same plane used for the excitation. Therefore the dipole components along x and z will only irradiate TM polarised radiation, whereas the dipole component along y can only emit TE polarised radiation in the (x,z) plane.

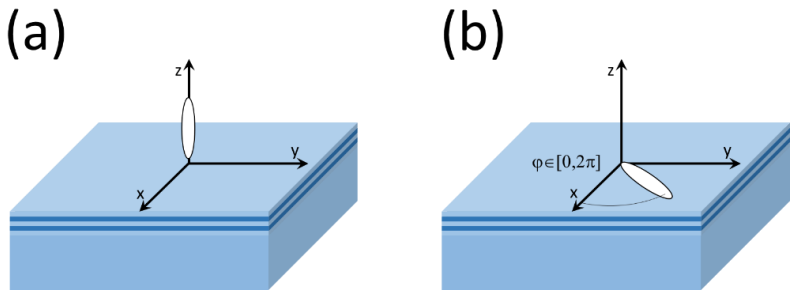

Figure 2.15 – Cylindrical dipole orientation distributions used to calculate the base radiance patterns. a) ⊥ case, b) ∥ case [29].

The next step is the calculation of the radiance pattern (angular and wavelength) of the fluorescence emission. Usually, when addressing such an issue, it is convenient to describe the emission of dipoles in proximity of a one-dimensional stack of metal/dielectric layers by assuming a cylindrical symmetry of their distribution function around the z axis. In the present case, given that the fluorescence excitation is carried out with a TE polarised beam such cylindrical symmetry is lost. However, with reference to Fig. 2.15, the radiance patterns for dipoles aligned perpendicularly to the stack (Fig. 2.15(a)) and for dipoles uniformly distributed in the plane of the stack (Fig. 2.15(b)) can be calculated. The results obtained can be used as a base set to describe the emission pattern arising from non-cylindrically symmetric dipoles distribution, as it occurs in our case.

In Fig. 2.16 the radiance patterns for the fluorescence emission of dye labels, for the two base distributions given in Fig. 2.15, are shown. The radiance pattern are obtained by means a numerical approach that makes use of a rigorous electrodynamic approach applying dyadic Green's functions developed at Fraunhofer IOF [33] In the following simulations the non-periodic 1DPC and a DyLight 650 fluorescent molecule are used to calculate all the emission patterns. Emission of fluorescence in the substrate (prism side) is considered here for the TE and TM polarisations. The emission in the cladding is not considered (because the fluorescence emission is collected from the prism side).

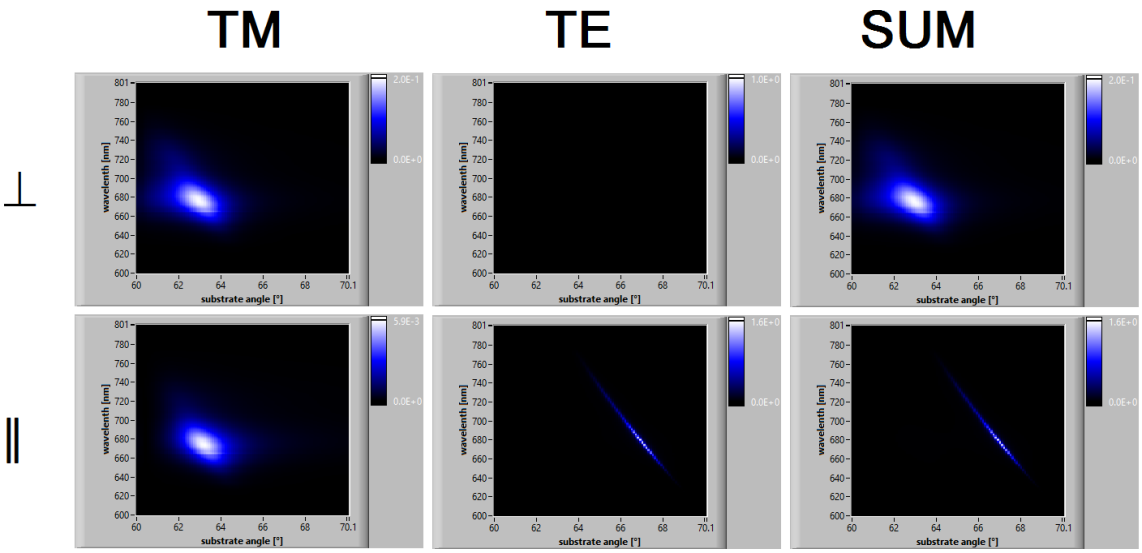

Figure 2.16 – Radiance patterns emitted in the substrate for the two dipole orientational distributions defined in Fig. 2.14. The patterns are calculated for the TM, TE polarisation states and for their SUM. The curves were obtained for the non-periodic 1DPC structure and for a DyLight650 dye.

From the radiance patterns shown in Fig.2.16, the luminous intensity curves, which are shown in Fig 2.17, can be extracted in all cases. These are the curves that are effectively measured in a biosensing experiment in which the angularly dispersed fluorescence emission of dye labels at the surface of the 1DPC is collected from the substrate side.

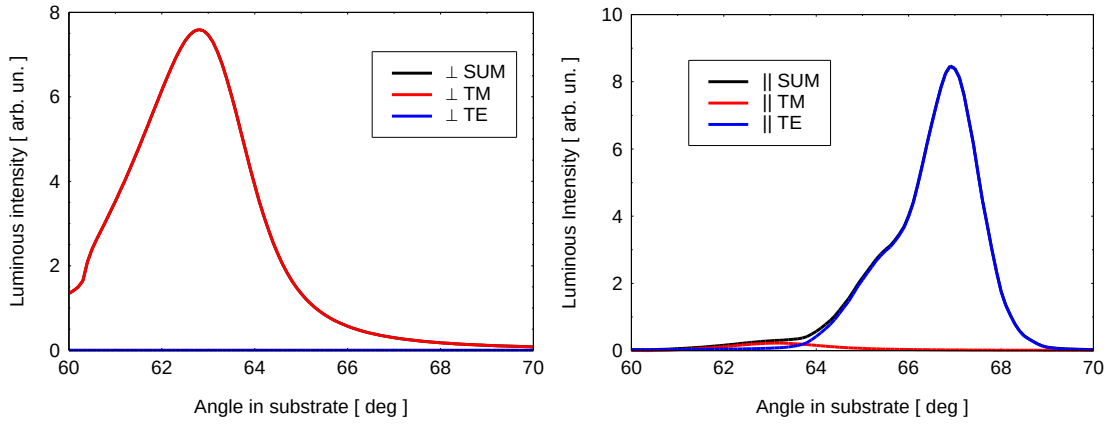

Figure 2.17 – Luminous intensity for fluorescence emitted in the substrate. (left) Dipole oriented perpendicularly to the stack, (right) dipoles oriented in the plane of the stack.

The emission of dye labels excited by a TE polarised beam can be calculated, according to the following considerations:

1) The dipoles aligned along z, perpendicularly to the 1DPC, will emit TM radiation only, with the radiance pattern shown in Fig. 2.16 (top left)

2) The dipoles aligned along x will emit TM radiation only, with the same radiance pattern shown in Fig. 2.16 (bottom left) but scaled by a factor 2 taking into account the orientation in the (x,y) plane. Here below the value of such scaling factor is derived. Assuming dipoles laying in the (x,y) plane with the following isotropic distribution (Fig. 2.15(b)):

$$f(\vartheta,\varphi)=\frac{1}{2\pi}\delta\left(\theta-\frac{\pi}{2}\right) \tag{2.41}$$

each dipole has a component along x according to a factor cos(φ) and contribute to the TM radiance with a factor $\cos^2(\varphi)$. The average of all dipoles contributions to the TM emission in the (x,z) plane will then be given by:

$$\int_0^{\pi}\delta\left(\theta-\frac{\pi}{2}\right)\sin(\theta)\,d\theta\int_0^{2\pi}\frac{1}{2\pi}\cos^2(\varphi)d\varphi=\int_0^{2\pi}\frac{1}{2\pi}\cos^2(\varphi)d\varphi=\frac{1}{2} \tag{2.42}$$

Such result indicates that they emit ½ of the radiance that they would emit if they were oriented along x. Therefore a dipole along the x direction contribute to the emission with the same TM radiance obtained for the ∥ case multiplied by a factor 2.

3) The dipoles aligned along y will emit TE radiation only, with the same radiance pattern shown in Fig. 2.16 (bottom centre) but again scaled by a factor 2 taking into account the orientation in the xy plane.

Assuming dipoles laying in the (x,y) plane with an isotropic distribution Eq.(2.41) (Fig. 2.15(b)), each dipole will have a component along y according to a factor sin(φ) and contribute to the TE radiance with a factor $\sin^2(\varphi)$. The contribution of all dipoles to the TE emission in the (x,z) plane will then be given by:

$$\int_0^{2\pi}\frac{1}{2\pi}\sin^2(\varphi)d\varphi=\frac{1}{2} \tag{2.43}$$

Such result indicates that they emit ½ of the radiance that they would emit if they were oriented along y. Therefore a dipole along the y direction contribute to the emission with the same TE radiance obtained for the ∥ case multiplied by a factor 2.

According to the considerations given above the TE and TM radiance emitted in the substrate by the dye labels upon excitation with TE polarised radiation will be given by the following expression:

$$\begin{cases} I_{TE}(\alpha,\lambda) = 2\dfrac{1}{5} I_{TE}^{\parallel}(\alpha,\lambda) \\ I_{TM}(\alpha,\lambda) = \dfrac{1}{15} I_{TM}^{\perp}(\alpha,\lambda) + 2\dfrac{1}{15} I_{TM}^{\parallel}(\alpha,\lambda) \end{cases} \tag{2.44}$$

The same expression can be used for the luminous intensity. In Fig. 2.18 the angular dependency of the luminous intensity of fluorescence collected in the (x,z) plane form the substrate side is shown.

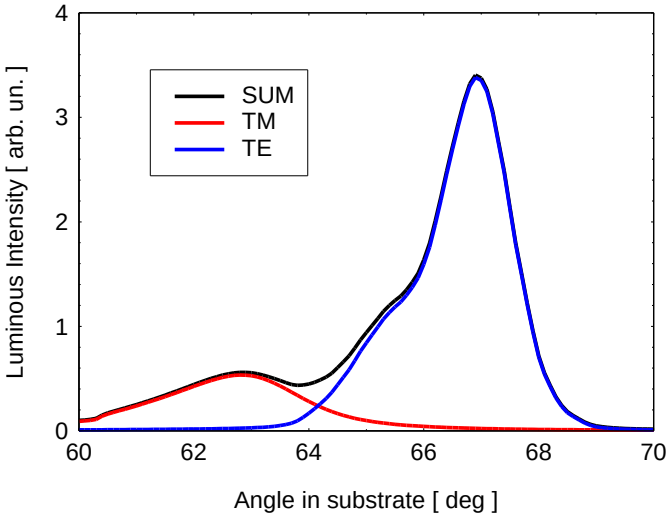

Figure 2.18 – Luminous intensity emitted in the substrate and in the (x,z) plane for dye labels at the surface of the 1DPC.

CHAPTER 3

Optical systems for the excitation and detection of BSW on 1DPC

In previous chapters, we discussed the optimum 1DPC design in order to obtain high performances in protein detection. In this chapter, we discuss the experimental set-ups that were developed during the present thesis work and that were used for the experimental characterization of the BSW biochips and for the bio-sensing experiments.

As we have seen, the BSW biochip consists of a 1DPC structure in which a resonance mode is excited and bio-molecular binding between the ligand immobilized on the sensing surface and the target analyte is measured. A standard BSW biochip must include the biochemical modification of the surface (bio-conjugation process) and the fluidic coupling system that usually consists of a flow cell confining the sample solution on the sensing surface.

It is therefore needed to set up an appropriate optical apparatus that can illuminate the BSW biochip in the correct angular range with light at a given wavelength (or more wavelengths) and to collect the reflected/emitted radiation for their analysis.

The three apparatuses used during the present work were:

S1- Extended laboratory test bench

Such apparatus was fully developed at SAPIENZA in the frame of the present work. It is a custom laboratory test bench designed and built with discrete optical elements. The custom nature of the test bench makes that it can operate in a wide range of the relevant parameters such as the wavelength, excitation angle, sample temperature. Therefore it was particularly suitable to characterize of the 1DPC and provide feed-back that was used to improve their design and fabrication (Chapter 6). In the final version, the setup can operate at λ=543nm, 632,8nm, 671nm, 830nm, 1300nm, 1550nm (fixed), 1450nm-1590nm (tunable); in the far-field configuration the incidence angle can be scanned in

the interval $\theta \in [30deg, 72deg]$; in the angular interrogation mode operates with a CMOS camera and a detection window that, depending on the optics used, can be tuned between 1deg and 4deg.

S2 – Modified infrared SPR platform

Such apparatus is based on a SPR platform that was formerly developed at Fraunhofer-IOF for biosensing with SPP and operating in the near infrared at the wavelength λ=804nm. The apparatus was adapted at SAPIENZA to operate in the label-free mode with BSW on 1DPC instead of SPP on Gold layers. Moreover it was complemented by an external optical setup used to excite fluorescence under controlled conditions. The main reason to modify and work with such apparatus was to preliminarily and quickly test the possibility to work with BSW in a SPR-like configuration, both in the label-free and fluorescence modes of operation (Chapter 6). The fact that the SPR platform operates at λ=804nm, whereas the target label-free wavelength for the present work was λ=670nm, does not constitute a limitation as all results obtained at one wavelength can be easily transferred to another wavelength by scaling the 1DPC geometry.

S3 – Final integrated BSW analytical instrument

Such apparatus was developed in the frame of the European project BILOBA coordinated by SAPIENZA. The integrated apparatus, whch can be considered as a self-consistent instrument, was designed and fabricated at Fraunhofer-IOF, partner of BILOBA, making use of the experience and the know how gathered by using the two other apparatuses. During the present work, the instrument was at SAPIENZA where its operation protocols were optimized and the first assays for cancer biomarkers detection were carried out (Chapter 6).

In the following paragraphs, we describe the three experimental apparatuses. Their optical scheme is explained in detail, putting into evidence the optical systems that were set up to implement both label-free and fluorescence operation modes. The description is complemented by some selected experimental results obtained with optimized BSW biochips, which will be used to illustrate the performance of the platforms. On the other hand, such results are used to demonstrate the effectiveness of the BSW approach and the characteristics of the BSW used in the biosensing assays described in the Chapter 6.

3.1 EXTENDED LABORATORY TEST BENCH (S1)

The extended laboratory test bench was setup starting from a precedent laboratory apparatus developed at SAPIENZA. During the present work, the test bench was completely rearranged, by adding, modifying, removing optical, electronic, fluidic, firmware, software and mechanical parts, in order to implement the label-free and fluorescence schemes. In Fig. 3.2 the latest version of the apparatus is shown.

Before their use, the bio-conjugated BSW biochips' surface is topped with a two-channels fluidic cell (see Paragraph Microfluidics) and the back face is coupled to a BK7 glass prism by means of a refractive index matching oil. Then the biochip is topped by an aluminium back plate with a PDMS contact layer that provides the fluidic connections (Fig. 3.1A) and then is mounted in the optical platform (Fig. 3.1B).

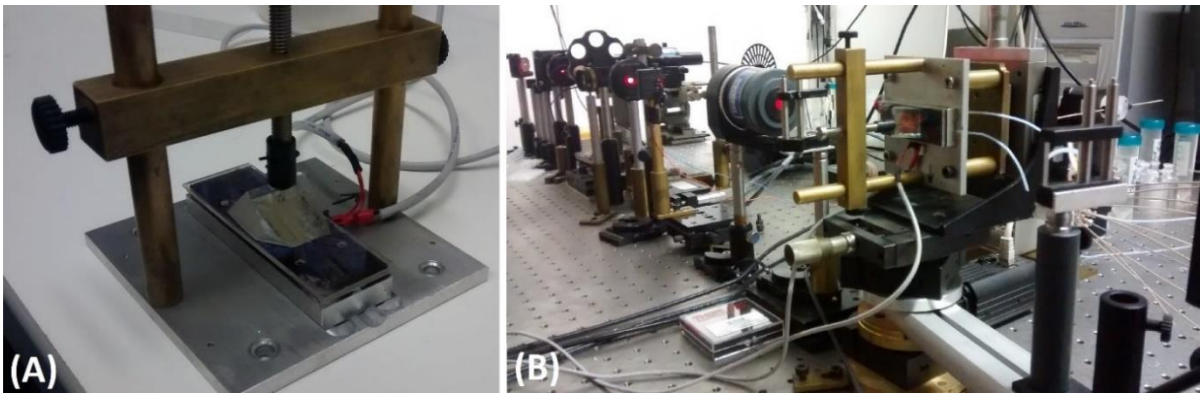

Figure 3.1 – (A) Detail of the BSW biochip holder with microfluidic flow cell and coupling prism. (B) Extended optical setup with BSW biochip holder mounted and aligned to the main optical path.

3.1.1 Optical system

For the label-free mode (LF mode), the fibre output from a temperature stabilized (±0.01°C) pigtailed laser diode (LD1), emitting at λ=671 nm with P_{CW}=3mW (Thorlabs LPS-675-FC), is collimated by means of an integrated fibre collimator and aligned to the optical table.

The linear polarisation of the beam is set by an input polariser (POL) which can be set at any angle. For the standard operation of the apparatus, the input polariser is set to:

- 0 deg for TE operation
- 90 deg for TM operation
- 45 deg for ellipsometric (CROSS) operation

The input polariser can be set to any other angle to perform particular measurements.

The beam then passes through a liquid crystal retarder (LCR) phase shifter (Newport, LCR-902). Such active element is used to change the phase between the TE and TM components of the probe beam. The LCR is voltage controlled by the apparatus PC via the output of an ADC. When the input polariser is set to 45 deg the state of polarization after the LCR can be set to any elliptic state in the reference system turned by 45 deg with respect to the table plane (incidence plane).

The beam is expanded by means of a telescope and the central portion is selected by a circular diaphragm (D). The parallel beam is focused by a cylindrical lens (f_1 = 100 mm) onto the coupling prism. A double rotation stage is used to set the average incidence angle at θ_{LF} and the angle of the detection arm at $2\theta_{LF}$. The reflected beam is imaged by a cylindrical Fourier lens (f_2 = 75 mm) onto an array detector.

During the first period of the thesis and in the label-free mode of operation, we used a 8-bit CMOS camera (Thorlabs DCC1645C, W=1280 pixel, H=1024 pixel, corresponding to 4.61 mm and 3.69 mm, respectively): Later on, when implementing the fluorescence mode, we changed the detector to a 12-bit monochrome CCD camera (Apogee Ascent, Sony ICX814 chip, W=3388 pixel, H=2712 pixel, corresponding to 12.50 mm and 10.00 mm, respectively). The long dimension W of the array detector is used to image the angular reflectance and achieve best sampling of the BSW resonance. In the final configuration where the CCD camera is used the field of view is 2.7 deg, which is determined by W and f_2, and the conversion factor between pixels and angle is 7.9E-4 deg/pix. The spots along the x direction are imaged along the short dimension H of the array detector by means of a properly positioned cylindrical lens (f_3 = 150 mm). As shown in Fig. 3.2, a rotating scatterer (RS), placed inside the telescope, destroys the spatial coherence of the illumination beam and the CCD integration time is set to integrate the scattered light, thus ruling out speckles' effect.

The fluorescence mode (FLUO mode) is implemented by making use of the same collection optics and CCD sensor (only) used for the LF mode (different integration time and binning) [34,35] and introducing a second laser for the labels' excitation. A polarized laser diode emitting at λ_{EXC} = 635 nm (LD2) is collimated and focused by a cylindrical lens (f_4 = 130 mm) to a strip on the chip surface. A dichroic beam splitter (DBS, Chroma ZT 640 RDC) is used to reflect the excitation beam and transmit fluorescence emission.

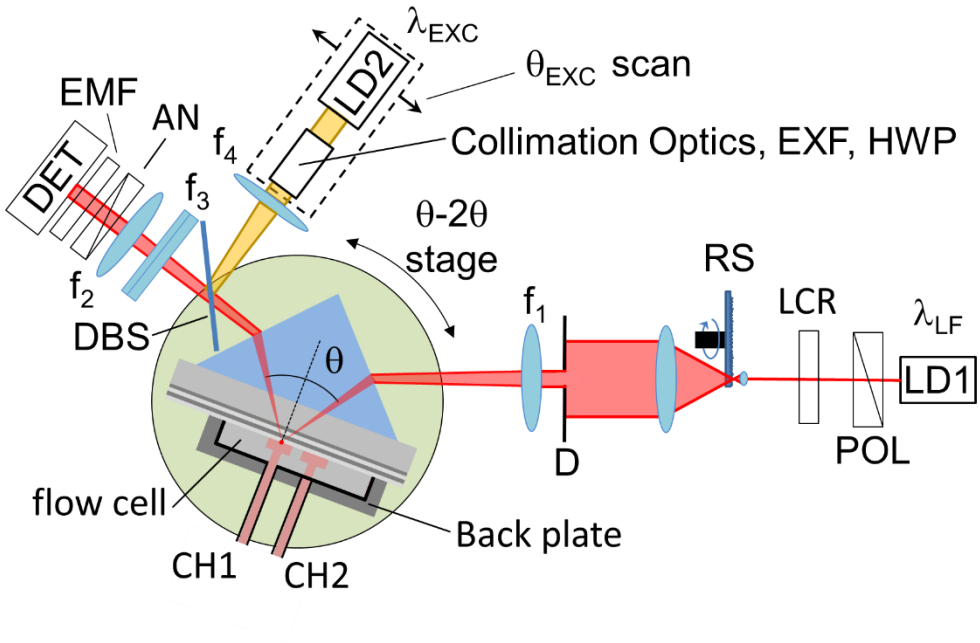

Figure 3.2: Simplified layout of the optical setup used to interrogate the BSW biochips. (LD1) LF laser at λ_{LF} = 670 nm, (LD2) FLUO laser at λ_{EXC} = 635 nm, (POL) polarizer, (LCR) liquid crystal retarder (RS) rotating scatterer, (D) diaphragm, (DBS) dichroic beam splitter, (f_1 to f_4) cylindrical lenses with f_1 = 100 mm, f_2 = 75 mm, f_3 = 150 mm, f_4 = 130 mm, (EMF) emission filter, (EXF) excitation filter, (HWP) half wave plate, (DET) either CMOS or CCD camera. Both the LF illumination beam at λ_{LF} and the fluorescence excitation beam at λ_{EXC} are focused along a strip at the biochip surface inside either the CH1 (case shown in figure) or the CH2 microfluidic channel.

The collimation optics, the excitation filter (EXF, Chroma ZET 635/20) and the half wave plate (HWP) used to set the polarization to TE are arranged inside the excitation arm. Great care was taken to align the fluorescence excitation spot to the label-free laser spot. The average incidence angle of the excitation beam θ_{EXC} can be tuned by translating the whole fluorescence excitation LD2 module (dashed box in Fig. 3.2). An emission filter (EMF, Chroma 655 LP ET Longpass Filter) is placed in front of the CCD to cut stray light from the excitation beam; such filter is transmitting at λ_{LF}, therefore preserving the label-free operation.

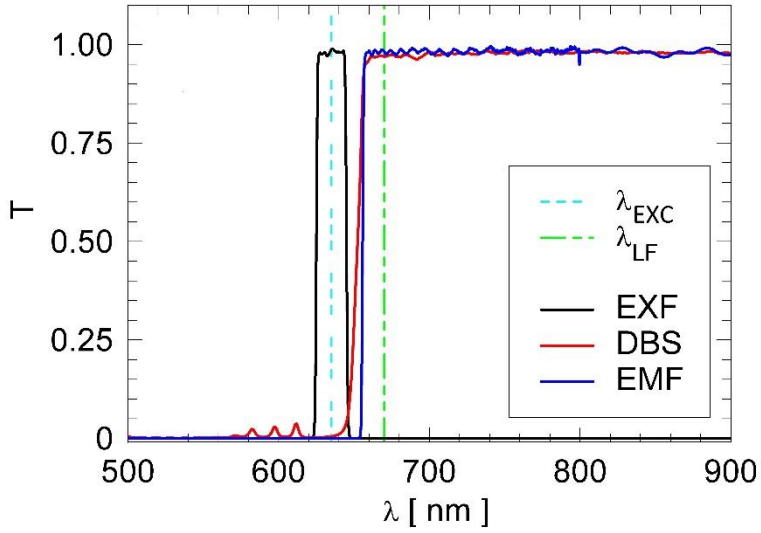

Figure 3.3 – Optical set-up filter set.

The filter set used here permits to operate with all dye labels with similar spectroscopic features and pertaining to the group: Alexa Fluor 647, DyLight 650, Cy5, Atto 647N, DiD, Quasar670. In Fig. 3.3, the filter set used in this experimental set-up is plotted with the two operation wavelengths. The design of the optical detection system ensures that the same angular range is observed for all spots along the illuminated region on the sensor surface for both LF and FLUO modes.

3.1.2 Microfluidic flow cell

The microfluidic cell is composed of a microscope glass slide with four connection holes and a structured adhesive spacer (Lohmann Adhesive Tape GL-187, thickness 200 µm) to the two channels CH1 and CH2 (see Fig.3.4). The two parallel parts of the channels are 18 mm long, 1 mm wide and 2 mm distant from each other. Such a microfluidic flow cell is fabricated at Fraunhofer IWS. Translating the coupling prism one can use either CH1 or CH2.

The surface and volume of each channel are 63.5 mm^2 and 12.7 µL, respectively.The glass slides and structured adhesive spacers are manufactured by laser-induced material ablation with a laser-microstructuring device (3D-MICROMAC, micro-STRUCT vario) and ultra-short-pulse lasers. The machining device is equipped with high precision linear axes as well as a galvanometer scanning head and additional complex measurement devices for analysis of the resulting microstructures. With this technology it is possible to generate and reproduce microstructures of approximately 5 µm. For the structuring of the microscope glass slides with overall dimensions of 76 x 26 mm^2 a wavelength of 355 nm, pulse duration of 30 ns and a

repetition rate of 50 kHz (Coherent, AVIA 355-X) was used. The structuring of the adhesive spacer with overall dimensions of 76 x 26 mm² was executed with a wavelength of 355 nm, pulse duration of 10 ps and a repetition rate of 66 kHz (Time-Bandwidth Products, FUEGO) [36].

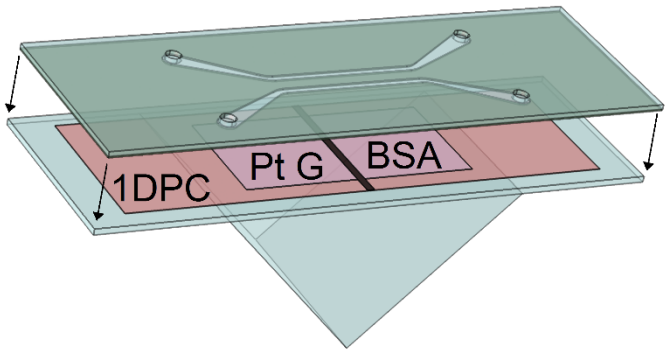

Figure - 3.4. Schematic of the 1DPC biochip and the fluidic cell. The microscope slide with four holes and the patterned adhesive tape is pressed on top of the 1DPC biochip. Both fluidic channels contain, for example, a PtG and a BSA region. The coupling prism position is also shown; the prism is coupled to the biochip by means of a contact oil.

After gluing the microfluidic cell to the bio-conjugated 1DPC surface, the resulting BSW biochip is topped by an aluminium back plate with a PDMS contact layer that provides the fluidic connections, as shown in Fig. 3.1. The plate can be temperature controlled by means of a resistor and a thermistor element (details in the following paragraph) and assure a stable temperature of the biochip (±0.01 °C). During the measurements, the temperature was kept constant at T = 30 °C.

3.1.3 Fluid handling system and temperature controller

The fluids handling system has been developed with the aim to drive/move the fluids across the micro-channels that constitute the fluidic circuit/path. The pumping and selecting system consists of a motorized syringe pump and of a 10 position stream selector (VICI-Valco), as shown in Figure 3.5A. The syringe pump (CAVRO Centris, Tecan) is used to suck the solutions from the drain end of the fluidic cell, in contact with the biochip surface, via a 4-way port. The syringe can be emptied in the waste by commuting the 4-way port. The source channel of the fluidic cell is connected to a 10-position stream selector allowing to pick the solutions from several different Eppendorf cuvettes. Both the syringe pump and the 10-position switch are

controlled by the same computer that is controlling the optical and electronic subsystems of the experimental set-up (S1).

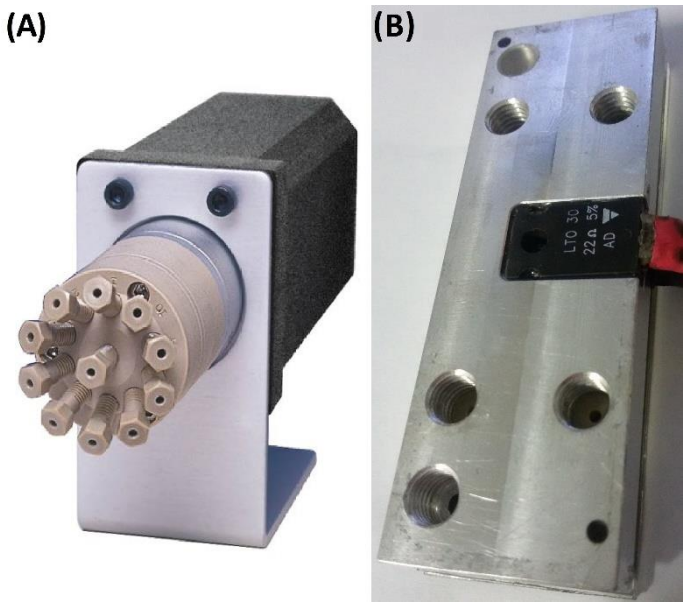

Figure 3.5 – (A) 10 position stream selector; (B) PT1000 thermocouple and thermistor embedded in the aluminum back-plate, the four chucks are intended to flux fluids in/out from the two channels.

The temperature controller, produced by Fraunhofer-IWS, is designed to match the two-channel fluidic cells and control the temperature of the chip during measurements. A PT1000 thermocouple and a thermistor (30 W Power Resistor Thick Film Technology from VISHAY) are embedded in the aluminum back-plate (shown in Figure 3.5B). By means such a back plate, the 1DPC surface provides the fluidic connections to the fluidic channels and the thermal contact needed to stabilize the temperature on the chip. An external controller is used to read the PT1000 (from Jumo) and drive the thermistor in a feedback loop configuration. The controller, by means the thermistor, can set any fixed temperature value needed for the biological assay.

3.1.4 Software interface

The LabVIEW software interface permits to control the instrument in label-free and fluorescence modes. The possibility of switching from one operating mode to another is insured by the optical shutters. In Fig.3.6 is shown the Labview software interface developed for the extended platform.

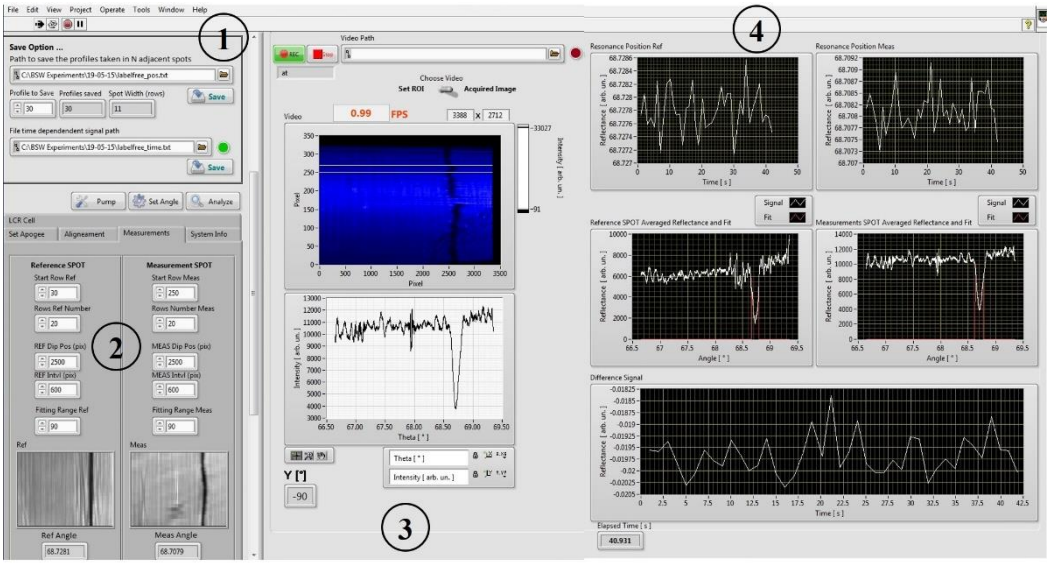

Figure 3.6 – Labview interface in label-free mode.

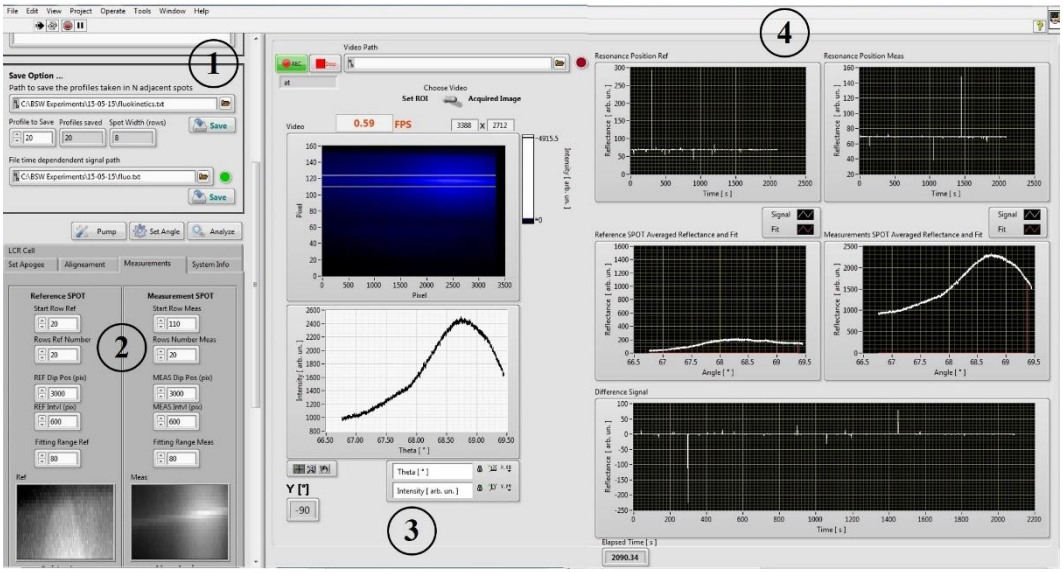

Figure 3.7 – Labview interface in fluorescence mode.

As shown in Fig.3.6, the software permits to track the resonance dip in real time in different spots (2) on the biochip surface providing the minima position plotted as a function of the experimental time (4). The box in position (1) is inserted to control input/output files while the part (3) consists in the real-time outputs from the CMOS/CCD sensors.

For example, in the label-free mode, the fit range, the integration time and the laser temperature can be set. It is also possible to define the CCD parameters such as binning, the spot width, the separation between each spot and the offset. Similarly, in fluorescence operation mode the integration time, region of interest and excitation position can be selected directly by the user (see Fig. 3.7).

3.3 MODIFIED INFRARED SPR PLATFORM (S2)

The modified SPR apparatus is derived from an SPR platform previously developed at Fraunhofer-IOF. In the original configuration, the instrument makes use of disposable cyclic olefin copolymer (COC, commercial name TOPAS, n_{sub}=1.526) chips with integrated coupling optics, on which a 45 nm thick gold film is directly deposited by sputtering. For the label-free operation the adapted SPR platform is a self standing instrument, as it includes both light source, detector and optics.

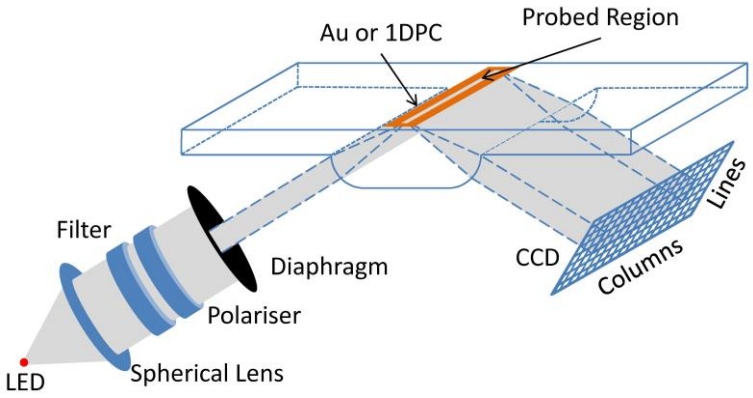

Figure 3.8 - Sketch of the optics of the adapted SPR platform used at SAPIENZA .

In Fig. 3.8 we show a sketch of the optical module of the adapted SPR platform. The beam from a light emitting diode (LED) is collimated by means of a spherical lens. To operate with BSW, the bandwidth was reduced by means of a 2.5 nm FWHM interferential filter peaked at λ=804 nm (Chroma). The polarization is defined by means of a thin film polarizer (Codixx AG) which can be rotated to ensure either TM or TE illumination. The beam is then focused by the input cylindrical facet of the TOPAS chip to an elongated spot onto the surface of the sensor. The incidence angle is around 66 deg and the angular aperture of the focused beam is ±2 deg. The reflected beam is collimated by the curved output facet of the chip and sent to a charge coupled device (CCD - Sony ICX205AL).

We used 1DPC deposited on standard microscope 170 μm cover slips (see Fig. 3.10(f)). TOPAS adaptor plastic chips were thinned and topped with a cover slip glued to their surface. Such adaptor chips could accommodate the 1DPC deposited on the cover slips and operated on SPR platform. Coupling of the cover slips to the adaptor chips was obtained by means of a contact oil (refractive index 1.518).

As shown in Figure 3.9 (top), in the label-free mode the reflectance can be measured at λ=804 nm in the $\theta \in [63.2°, 67.2°]$ angular range above the total internal reflection (TIR) edge.

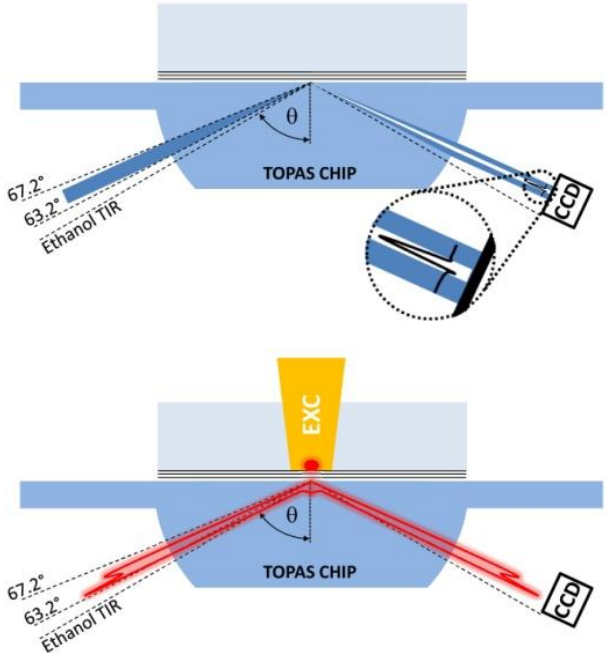

Figure 3.9 - Sketches of the label-free (top) and fluorescence (bottom) modes of operation of the sensing platform. (top) A focused beam at λ is used to illuminate the chip under total internal reflection conditions and the presence of a resonance is detected by a CCD sensor. (bottom) An external laser beam at λ_{EXC} is used to excite molecules in proximity of the chip surface and the emission, strongly coupled to the BSW surface bound modes, is directed into a narrow angular range and detected by the same CCD sensor.

For the fluorescence operation of the adapted SPR platform it was necessary to complement the original SPR instrument with external components mounted on an optical table. In the photographs shown in Fig. 3.10, we show the present implementation of the adapted SPR apparatus at SAPIENZA.

Fig. 3.10(a) shows a general view of the apparatus. The original SPR platform from Fraunhofer-IOF was un-mounted and the optical part was fixed on the optical table. The He-Ne laser in the background is used to excite fluoresce from top of the chip; along the beam line there a polarizer, an interferential filter and a mirror used to direct the beam on the bio-chip surface. With reference to Figure 3.9 (bottom) we excited the molecules by the external laser beam at λ_{EXC} (632.8 nm or 543 nm) and collected the emission in the same angular range as in the label-free mode with the same CCD sensor (operated at a different gain and integration time).

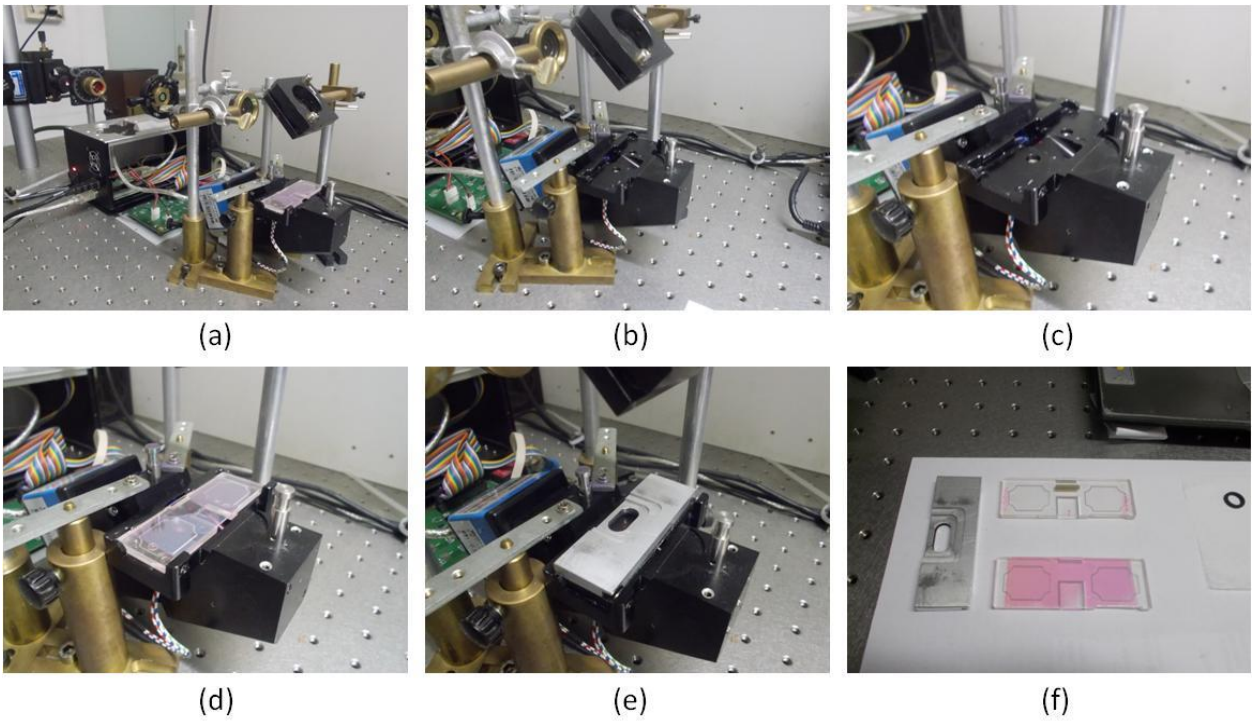

Figure 3.10 – (a) modified SPR apparatus, (b) apparatus with the mirror, (c) holder of the bio-chip, (d) holder with a TOPAS bio-chip coated with a 1DPC; one can see the red spot of the He-Ne laser at the surface of the bio-chip, (e) holder with the bio-chip and the open cell used for the fluorescence measurements, (f) couple of TOPAS chips coated with either a gold layer or a 1DPC (A|13|332).

3.4 INTEGRATED BSW ANALYTICAL INSTRUMENT (BILOBA PLATFORM, S3)

The platform is the final result of the collaborative EU funded project BILOBA devoted to BSW optical biosensors for early cancer diagnosis. The optical configuration is similar to that of the extended laboratory test bench. The design was accurately chosen in a way to obtain a compact system with the same functionalities. In the following, we shall refer to such an integrated system, which constitutes a real instrument for point-of care applications, as BILOBA platform. The instrument makes use of 1DPC deposited on molded disposable biochips, made up of a cyclic olefin copolymers (COC, commercial name TOPAS). These biochips include a prism shaped cross section in order to excite the surface wave in Kretschmann-Raether configuration, as mentioned in the above paragraph. Additionally, a two-component flow cell has been molded. As shown in Fig. 3.11, this flow cell consists of a hard polymer cover that can be clicked by hand onto the chip. Inside this cover, a straight micro

channel of 800 µm x 100 µm cross-section as well as perpendicularly aligned fluid connectors is defined by an elastomer. The injection molded chips were coated by plasma ion assisted deposition (PIAD, described in details in the next chapter) and the 1DPC, sustaining BSW located at their surface in aqueous environment for operation at the label-free wavelength of λ_{LF} = 670 nm.

Figure 3.11 –Molded disposable polymer BILOBA biochip (bottom) with its fluidic cell (up).

In the experiments carried out at SAPIENZA, the BILOBA platform, and the biochips, were complemented by the same fluid handling system described in the Paragraph 3.1.3. A simplified spring loaded and temperature controlled chip support is designed and manufactured at the Fraunhofer-IOF in order to control and limit thermal and mechanical fluctuations. Similarly, the fluidic handling system is coupled via Upchurch connectors to the external syringe pump. Again, the pump has the key role of pumping analyte solutions to be analyzed through the flow cell [36]. A simplified overview of the BILOBA optical system is illustrated in Fig. 3.12A. A collimated light beam B is focused by means of a cylindrical lens C1 into the biochip (Fig.3.11). The prismatic shape is required to illuminate the sensor surface above the critical angle so that the total internal reflection occurs (TIR). In this configuration shown in Fig. 3.12A, an illuminated line along the direction x is created on the surface, which is coated with the 1DPC. Analogously to the laboratory test bench, several measurement areas (“spots”) can be arranged in a row along this illuminated line.

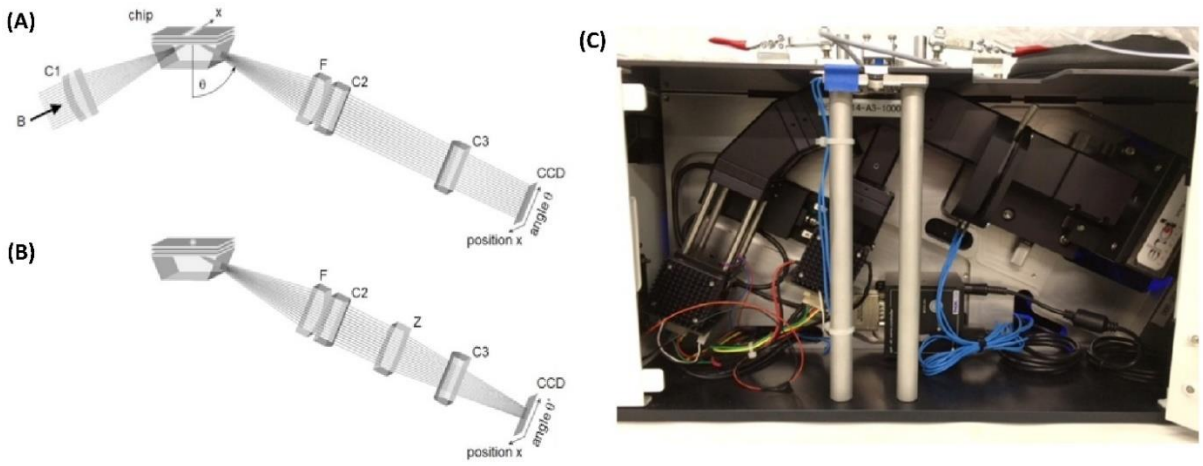

Figure 3.12 – Simplified view of the optical system in label-free (A) and fluorescence (B) modes; photo of the real optical system (C).

In order to image the direction x onto one coordinate of a CCD detector and to achieve a parallel readout of these spots a cylindrical detection optical system that consists of objective (C2) and tube lens (C3) systems is used. The design of the optical detection system ensures that the same angular range is observed for all spots along the illuminated region on the sensor surface. A laser diode at λ_{LF} = 670 nm is utilized for label-free analysis to achieve proper resolution of the narrow angular BSW resonances. The detection optical system has an extended CDD detector to obtain 3388 (angular axes) and 2712 (position axes) pixels readout. The lateral field of view (coordinate x in Fig. 3.12A) is approximately 6 mm and 8 pixels binning is generally applied because of the limited spatial resolution of lateral imaging. The angular field of view is determined by cylindrical Fourier lens F to be approximately 2.9 deg. In such a direction, a full discretization of the CCD chip (no binning) is exploited in order to achieve proper sampling of the resonance. For label-free detection the region of interest (ROI) is reduced to approximately 1200 pixels around the resonances in order to decrease the time need for CCD read out and data transmission.

On the other hand, fluorescence excitation is based on a laser beam at λ_{EXC} = 635 nm. Spatial imaging and binning are identical to the label free case. However, due to the small angular range of 2.9 deg, that does not allow to detect both emission polarization, an additional cylindrical lens Z (Fig.3.12B) is introduced onto the light path to enlarge the angular acceptance from 2.9 to 8 deg. The limited angular resolution associated with this approach is acceptable, and consequently angular binning of 8 pixels can be set in fluorescence detection mode. Filter elements for selecting a certain polarization and/or spectral range are arranged in-between the cylindrical objective (C2) and tube lens (C3) systems. The spectral fluorescence

emission filter is fixed in the detection optics because the label-free operating wavelength (670 nm) is well within the fluorescence emission band.
A complete overview of the analytical instrument with its housing is shown in Figure 3.13.

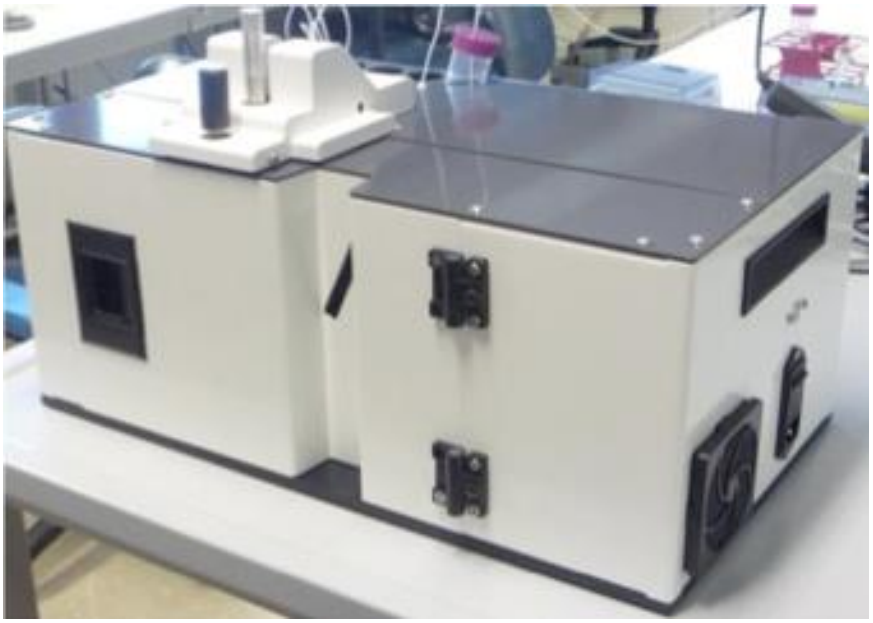

Figure 3.13 - Complete BILOBA analytical instrument.

3.5 COMBINED LABEL-FREE AND FLUORESCENCE OPERATION MODES

In the following paragraph a working scheme is presented in order to illustrate the combined functionalities of the platforms. The operation scheme described in the present paragraph is attributed to platform S1 but well explain the operation of platform S3. In this thesis, these two set-ups are used for the cancer biomarker assays (see Chapter 6). In order to monitor specific bio-molecular interactions, the BSW biochip's surface can be tailored with specific capture antibodies and used for real-time bio-sensing applications. On the sensitive surface of the BSW biochip one can define several spots along the x direction, for example three as shown in Figure 3.14a, where different capture mAbs (either specific or non-specific) are immobilized (S, R1, R2). The sensing spots are probed simultaneously, with the aim to quantify the amount of target molecules captured by each of them. The parallel read-out system is based on strip-shaped illumination beams for both label-free and fluorescence operation modes (Fig. 3.14a and Fig.

3.14d), which are obtained by using cylindrical optics. As described above, the detection is carried out by means of a cylindrical optical system and a CCD or CMOS array detector that provides along one direction (columns) the angular dependence of the intensity for each position x (rows direction).

The microfluidic cell with two channels that are aligned to the strip-shaped focused beam (red line parallel to CH2 in Figure 3.14a), permits to perform two assays on the same chip in a sequence. As an example of the general operation scheme, we made use of the 1DPC deposited on glass with the two channel PDMS fluidics (described above in the Paragraph 3.1.2).

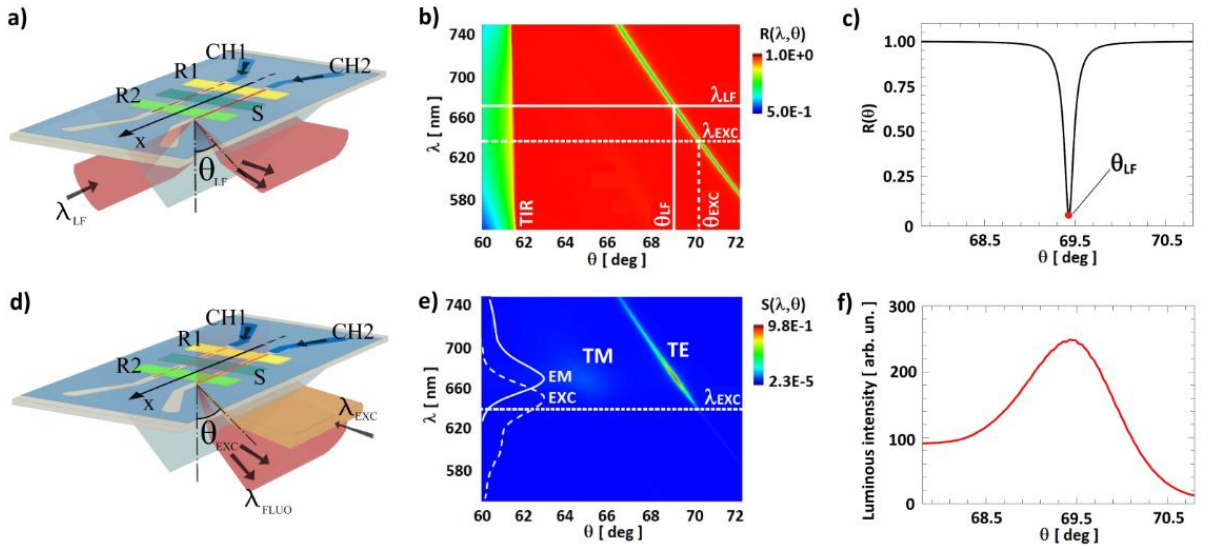

Figure 3.14 - (a) Sketch of the optical layout for the LF mode. The BSW biochip reflects the illumination laser beam at λ_{LF} and the optics in the detection arm collects the angular reflectance for each sensitive spot (R1, S, R2) along the x direction (b) Reflectance map $R(\lambda,\theta)$ calculated for the design 1DPC and TE polarization. The lasers' wavelengths λ_{LF} and λ_{EXC} correspond to two different BSW resonance angles, θ_{LF} and θ_{EXC}. (c) 1DPC reflectance $R(\theta)$ at λ_{LF} for the TE polarization. In the inset, we show the geometry of the 1DPC and the electric field intensity distribution calculated at resonance. (d) Sketch of the optical layout for the FLUO mode. For each spot, both excitation at λ_{EXC} and fluorescence collection at λ_{FLUO} take place from the same side. (e) Emitted intensity map $S(\lambda,\theta)$ calculated for isotropically oriented Alexa Fluor 647 dye molecules at the surface of the 1DPC, where both TE and TM (weak) polarized contributions appear. The absorption and emission spectra for Alexa Fluor 647 are shown on the left axis. (f) Radiant intensity $I(\theta)$ calculated for isotropically oriented Alexa Fluor 647 dye molecules at the surface of the 1DPC (integral along λ of the $S(\lambda,\theta)$ shown in Fig. 3.14e).

For label-free operation (LF mode), a cylindrically focused ($\Delta\theta \sim 5$ deg) laser beam at λ_{LF} is coupled to the biochip by means a glass prism. Owing to the illumination configuration [18],

the angular reflectance $R(\lambda_{LF},\theta)$ can be probed simultaneously in every spot along x, as also described in previous works [7,36]. In Figure 3.14b we show the numerically simulated $R(\lambda,\theta)$ map for the TE polarization case, where the BSW dispersion $\lambda(\theta)$ is apparent as a dark line laying beyond the TIR edge. As shown in Figure 3.14c, when operating at fixed λ_{LF}, a dip is observed in the $R(\theta)$ profile, whose position θ_{LF} depends on the refractive index at the surface of the 1DPC. By tracking θ_{LF} on the CCD images one can therefore probe, spot by spot, the refractive index changes and the amount of analytes captured at the biochip surface.

For fluorescence operation (FLUO mode), a laser beam at λ_{EXC} = 635 nm is cylindrically and weakly focused ($\Delta\theta \sim 1$ deg) through the prism (as already described in Paragraph 3.1.1) at θ_{EXC} in order to couple to the BSW at λ_{EXC} and to resonantly excite dye molecules at the surface of the biochip, as sketched in Fig. 3.14d. λ_{EXC} is chosen to match the maximum of the dye absorption spectrum shown in Fig. 3.14e. The angular emission pattern of the dye molecules in the presence of the 1DPC is modified and re-directed in the collecting system [18,35]. In Fig. 3.14e, we show the intensity $S(\lambda,\theta)$ emitted in the prism by randomly oriented dye labels located at the 1DPC surface. As it can be seen each λ component of the dye emission spectrum ($S(\lambda)$ in Fig. 3.14e) is emitted at a different angle θ according to the BSW dispersion $\lambda(\theta)$ for both the TE and TM polarizations. A wavelength insensitive sensor will measure the integral of $S(\lambda,\theta)$ over λ, i.e. the radiant intensity $I(\theta)$, whose angular pattern is reported in Fig. 3.14f.

CHAPTER 4

Fabrication and characterization of the optimized 1DPCs

In the present Chapter, we report on the results obtained in the experiments carried with BSW biochips. The illustration and discussion of the results will permit to point out the main characteristics of BSW modes, to demonstrate the effectiveness of the BSW approach and to show the operation of the platforms described in the Chapter 3, therefore completing the descriptions given therein.

During the thesis work, as it will be shown below, I used and characterized a large number of test 1DPC deposited on reference substrates and of complete BSW biochips, mainly in the frame of the activities of the European project BILOBA. For the sake of clarity, not all results will be shown here.

The test 1DPC deposited on reference substrates and the final BSW biochips used in the present work were fabricated at Fraunhofer-IOF in the frame of the BILOBA project, by the well-established plasma ion assisted evaporation method for thin film fabrication . Therefore, first of all the fabrication technique is briefly described. As discussed in Chapter 2, in order to get high sensitivity and resolution, it is necessary to carefully control the refractive indices and the thicknesses of the dielectric constituents. This made that the fabrication and characterization activites were carried out in close collaboration, with the aim to get to BSW biochips that are optimized for bio-sensing applications and whose performance will be widely described in Chapter 6.

4.1 FABRICATION OF 1DPC: PIAD DEPOSITION TECHNIQUE

The method used for the deposition of the 1DPC stacks was Plasma-Ion Assisted Vacuum Evaporation (PIAD). This technique belongs to the Physical Vapour Deposition (PVD) methods that are carried out under high vacuum conditions. In Fig. 4.1, a scheme of the PIAD working principle is shown. The material from a thermal vaporization source (tungsten wire coils or high energy electron beam heating) reaches the substrate with a "line-of-sight" trajectory. The high vacuum environment permits to reduce gaseous contamination in the deposition system. Typically, vacuum deposition takes place with a gas pressure in the range of 10^{-5} to 10^{-9} mbar depending on the level of gaseous contamination that can be tolerated for the application. The deposited material is proportional to the relative vapor pressure of the material in the molten source. Generally, the substrates are mounted at an distance from the vaporization source to reduce radiant heating of the substrate by the vaporization. For the PIAD technology (as shown in the schematic drawing in Figure 4.1), a plasma ion source is installed at the center of the chamber. The high energetic ions that are emitted from the source and accelerated towards the substrate holder allow to densify the growing layer very effectively without heating the substrates.

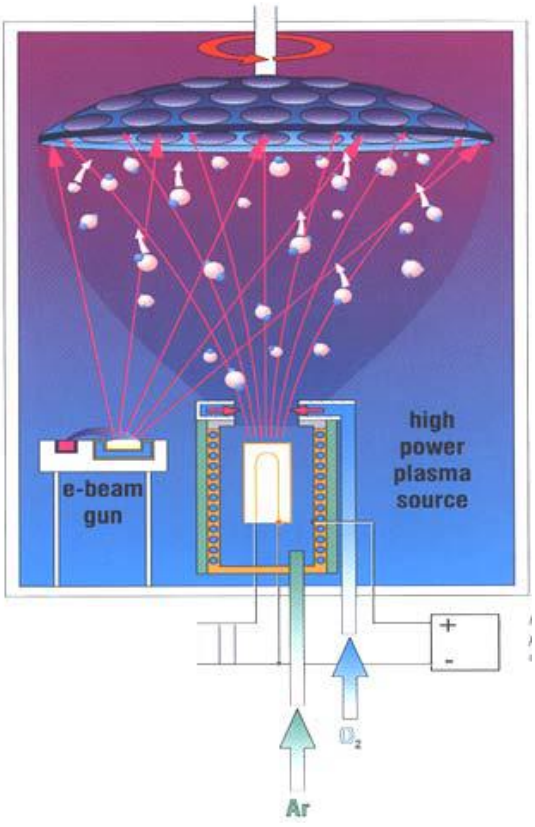

Figure 4.1 - Schematic drawing of PIAD deposition technique. Courtesy of Fraunhofer IOF.

The plasma ion source which represents the core element of a PIAD plant is based on a LaB_6 -cathode, with a cylindrical shaped anode tube in presence of a solenoid magnet. The cylindrical LaB_6 -cathode is indirectly heated by a graphite filament heater. A dc voltage between anode and cathode creates a glow discharge plasma with a hot electron emitter, supplied with a noble gas such as argon. Due to the magnetic field of the solenoid magnet, which surrounds the anode tube, the plasma is extracted and directed towards the substrate holder. The reactive gases are introduced through a ring shower located on top of the anode tube. Because of the high plasma density, the reactive gases get activated and partly ionized. Ionization of the reactive gas lowers the required reactive gas pressure, to grow stoichiometric films. Therefore, the ion energy is mainly determined by the self-bias voltage between anode and chamber ground. The magnitude of the bias voltage, which is controlled during the evaporation process, depends on the applied discharge voltage, the magnetic field strength, the gas flows and the chamber pressure. Since the plasma spreads in the total volume between the plasma source and the substrate holder, the evaporant also becomes partly ionized. Because of the possibility to deposit coatings with an adjustable densification and stoichiometry at low substrate temperature the PIAD method is suitable for the deposition of the 1DPC on polymeric substrates. The vacuum evaporation technology owns the possibility to evaporate stoichiometric materials like SiO_2, Ta_2O_5, TiO_2, Al_2O_3 and many more. Therefore, highly stoichiometric coatings with a very low level of impurities can be deposited, resulting in extremely low absorption losses. In Fig.4.2 it is shown the PIAD deposition plant APS 904 (Leybold Optics) utilized to deposit all 1DPC used in this work.The thickness and refractive index accuracy for the deposition of single layers or layer stacks can be in the range of ±1% for optimal conditions. This accuracy represents the run-to-run reproducibility as well as the thickness distribution on the complete substrate holder. During the present thesis work, the robustness of the BSW characteristics with respect to the fabrication tolerances were investigated both experimentally and theoretically [37]. The results demonstrated that the PIAD fabrication tolerance permits to manufacture robust 1DPC for the target bio-sensing application.

Figure 4.2 - PIAD deposition plant APS 904 (Leybold Optics) used for all depositions of the 1DPC. Courtesy of Fraunhofer-IOF.

By the ion assistance during the evaporation, dense coatings can be deposited without substrate heating. Hence, the temperature can be kept low enough to coat polymer substrates with comparatively thick 1DPCs (plastic chips used on S2 platform) and, of course, glass substrates (glass chips used on S1 extended optical system). The two types of 1DPC, on glass and plastic, respectively, are shown in Fig.4.3.

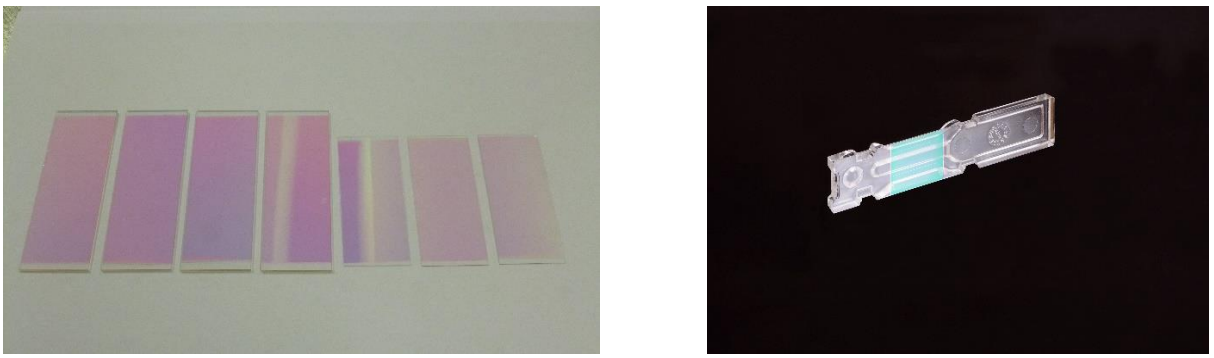

Figure 4.3 – 1DPCs on glass (left) and plastic (right) substrates.

The 1DPC families that were deposited by PIAD and used for the present work are shown in Figure 4.4, where it is indicated the platform on which they were tested and the results obtained.

The intermediate families permitted to improve the 1DPC properties and lead to a final optimized generation that was finally used in all cancer biomarkers' detection assays, which are reported in the Chapter 6.

In the following sections, as examples of the characterization measurements, I report the results obtained with the optimized 1DPC.

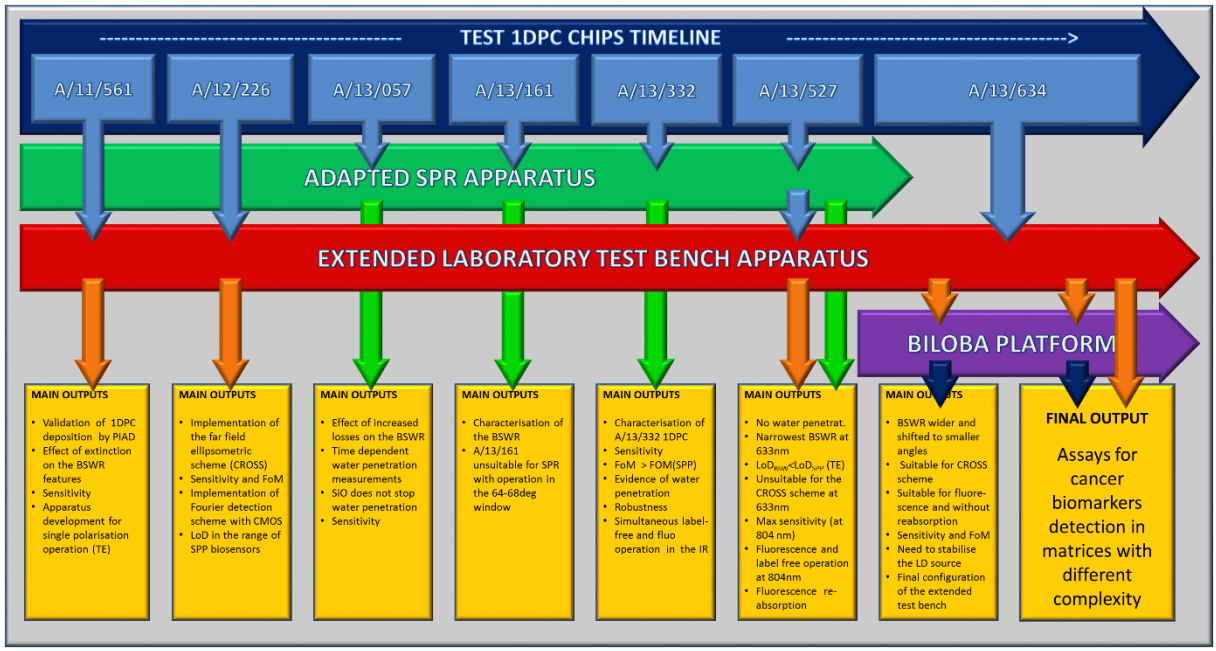

Figure 4.4 –Optical apparatuses and 1DPC families used during the doctorate period.

4.2 OPTIMIZED 1DPC FOR BLOCH SURFACE WAVE BIOCHIPS

In Chapter 2, we obtained an optimal 1DPC structure to be used in bio-sensing applications (see Chapter 6). To measure cancer biomarkers in biological matrices we made use of such optimized 1DPC noted as A|13|634 in Fig. 4.4. The dielectric materials chosen for the optimized 1DPC fabrication are silica (SiO_2) for the low index layers, and tantala (Ta_2O_5) and titania (TiO_2) for the high index layers. The refractive indices were determined either by reflection/transmission spectroscopy on single layers or by ellipsometry to be $n_{SiO2} = 1.474 + j5E\text{-}6$ and $n_{Ta2O5} = 2.160 + j5\times10^{-5}$, $n_{TiO2} = 2.28 + j1.8\times10^{-3}$ at λ_{LF} =670 nm. Starting from the substrate, the 1DPC consists of a stack with a first silica layer, a periodic part with two tantala/silica bilayers and a topping thin titania/silica bilayer. The nominal thicknesses are d_{SiO2} = 275 nm, d_{Ta2O5} = 120 nm for the periodic part and d_{TiO2} = 20 nm, d_{SiO2} = 20 nm for the topping layers. In the following paragraphs a characterization of the optimized 1DPC is presented. The characterization is carried out for the extended laboratory test bench (S1) and

the integrated platform (S3). All the experimental results obtained with cancer biomarkers (see Chapter 6) are performed with these two platforms.

4.3 CHARACTERIZATION OF THE OPTIMIZED 1DPC ON S1 PLATFORM

4.3.1 Label-free mode

In the following, we report experimental characterization obtained in the TE polarization. In particular, we measured the angular shift of the minimum of the resonance dip as a function of the properties of the solution injected onto the sensing surface. In Fig. 4.5, we show the angular reflectance measured for the 1DPC sensor in TE, from a Lorentzian fit of the experimental curve, we find that D = 0.80, W=0.13 deg.

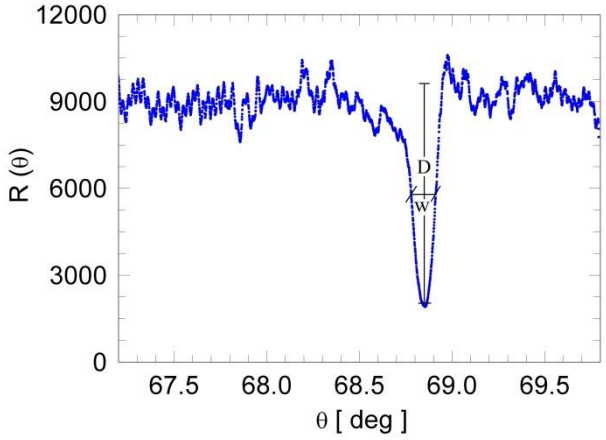

Figure 4.5 – Reflectance profile obtained in D-PBS 1X on S1 platform.

Moreover, the sensitivity (S_V) of the 1DPC sensor is determined by injecting in the fluidic cell solutions of D-glucose in DI-water at several different known concentrations (0.05, 0.5 and 5 wt%). In Fig.4.6, we show the time dependence of the resonance position measured in the cross scheme, when either DI-water or the glucose solutions are injected in the fluidic cell. From the measurement, we derived the linear dependency of the resonance angle on the refractive index of the solutions as previously done in a precedent work [38]. From the slope of the linear behavior, one can find S_V = 31.8°/RIU that in good agreement with numerical calculations.

According to the FoM definition and taking into account the parameters calculated above for the extended optical set-up S1, it follows:

$$FoM = S \cdot \frac{D}{W} = 193\ RIU^{-1} \tag{4.1}$$

The value obtained for the FoM for S3 is in very good agreement with the one evaluated on S1. It has to be noticed that for SPR-based sensors a typical value for the FoM is 48 RIU^{-1} [7].

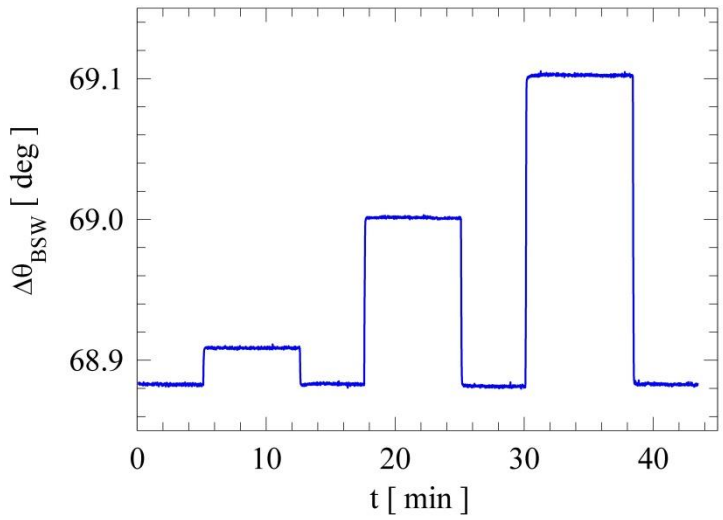

Figure 4.6 - Shift of the resonance position over time when exposing the chip to increasing solutions of D-glucose dissolved in DI-water.

4.3.2 Fluorescence mode

In order to characterize fluorescence operation on S1, we used a simple protocol to selectively bind molecules conjugated with DyLight650 onto 1DPC surface. To favor selective binding we adopted a strategy based on biotin-neutravidin interaction (details in Chapter 5).

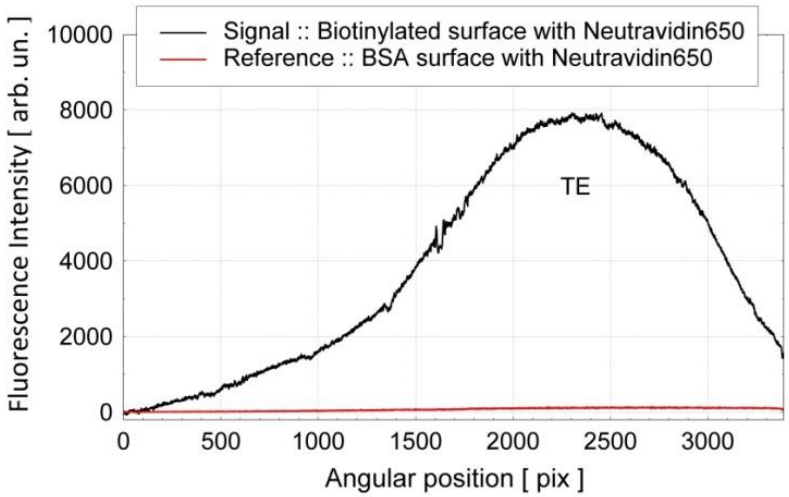

Figure 4.7 – Fluorescence angular spectra in the two regions of the BSW biochip, reference (red curve) and signal (black curve).

Once the biochip is functionalized and bio-conjugated, the modified 1DPC surface is allowed to react with NeutravidinDyLight 650. This conjugated molecule assures specific interaction thanks to neutravidin binding sites and suitable fluorescence characteristics for fluorescence operation. In Fig. 4.7, it is shown a typical fluorescence output with spectra collected in two regions of the biochip, with dye bound at the surface and without dye, respectively. The two macro-spots are referred in the graph as signal and reference sides.

4.4 CHARACTERIZATION OF THE OPTIMIZED 1DPC: CALIBRATION TEST ON S3

4.4.1 Label-free mode

In order to measure the sensitivity of the 1DPC, in TE polarization, a biosensing experiment is carried out injecting different dilutions of D-PBS (Dulbecco‘s Phosphate Buffered Saline) in DI (de-ionized) water. Once a stable base-line is determined in DI-water, 500µL of D-PBS 1X (10mM) with a flow rate of 3.59 µL/s are injected in the flow cell. As a consequence, the resonance shifts reaching a stable value in D-PBS 1X.

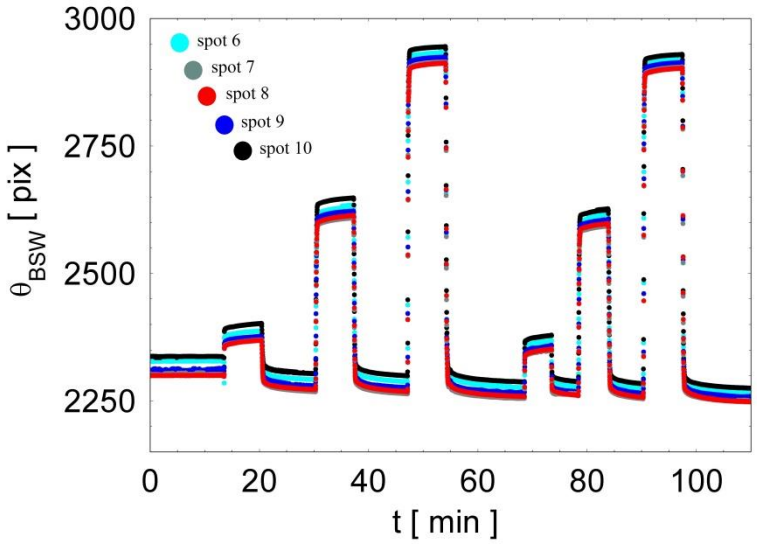

Figure 4.8 - Shift of the resonance position over time when exposing the chip to increasing dilutions of D-PBS in water for different spots. The procedure is repeated twice.

After 10 minutes, DI is injected again in the flow cell in order to replace the previous solution and to allowing to resonance position to recover to the initial position. This procedure is repeated injecting 500 µL of D-PBS 5X (50mM), and then 500 µL of D-PBS 10X (100 mM) always rinsing with 500 µL of DI-water between solution injection. The data shown in Fig 4.8 are acquired with a CCD integration time of 80 ms, and with a laser current of 33,4 mA,

keeping also constant the laser and the chip temperature at 30°C and at 25°C, respectively. By reducing the thermal fluctuations, one can decrease the noise level, improving the resolution. The aim of these experiments is to obtain resonance shifts, according to different dilutions of D-PBS ($C_{D\text{-}BBS}$), thus a calibration curve.

The refractive indices of D-PBS 1X, 5X and 10X (10 mM, 50 mM, 100 mM), used in the experiments, are measured by an Abbe's refractometer. The refractive index values found in the visible range of wavelength (400-700 nm) are plotted in Fig. 4.9.

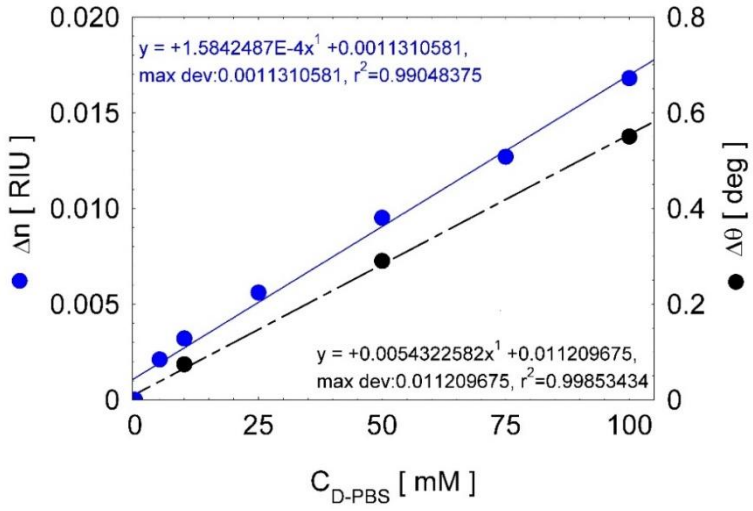

Figure 4.9 – Refractive index vs D-PBS dilutions (blue); angular shift vs D-PBS dilutions (black).

The refractive index is linearly related to the dilutions. By fitting linearly the experimental points we obtained values for "a" ($1{,}584\times10^{-4}$ RIU / mM) and "b" (0,0011 RIU), considering a general linear model: y = ax +b. These parameters represent the conversion factors between RIU and mM. In fact, they allow to evaluate the refractive index variation, once the concentration is known, and vice versa, the concentration can be deduced from the refractive index variation.

In Fig.4.9, the angular shift is reported as a function of the different $C_{D\text{-}PBS}$. In particular, as can be seen in this figure, the three points are represented with their respective error bars (not visible on graph). Different algorithms can be applied to evaluate the minimum position, i.e. the measured value in label-free operation from the angular reflectances. In this case, for each angular reflectance taken experimentally, an approximate minimum position has been determined, followed by fitting in a data interval in $\theta_R \pm \theta_W$ angular (or camera pixel) range around this minimum. From such a fit the final minimum position has been obtained and plotted in real-time. The black line in Fig. 4.9 represents the calibration curve. It describes the instrumental response (analytical signal) changes as a function of the analyte concentration. By

means of this curve the unknown analyte concentration can be determinate by measuring the instrument response (Δθ).

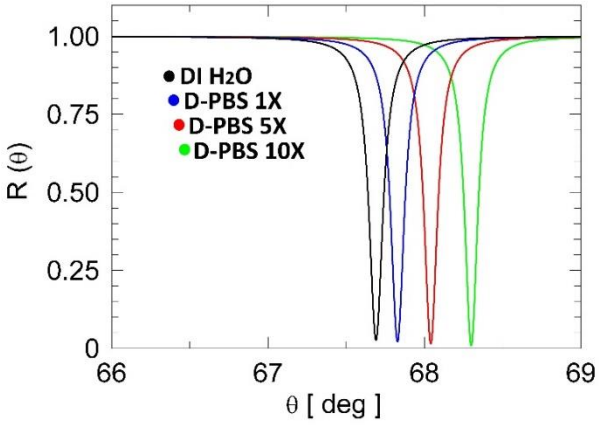

Figure 4.10 –Theoretical dependence of the reflectance to refractive index changes.

In Fig. 4.10 is shown the theoretical dependence of the reflectance profiles as a function of the external medium refractive index. A shift of 0.55 deg is observed when D-PBS 10X is injected. Combining the information summarized in Fig.4.11, an estimation of the sensitivity can be obtained. Since the data collected were in pixels, these were multiplied by the conversion factor (3388 pix = 2.9 deg) in order to obtain values in degree. The volume sensitivity $S_V = d\theta/dn$, as already defined in Section 1, is the slope of the curve representing the angular shift $\Delta\theta$ versus the refractive index change Δn. In Fig. 4.11, both experimental and theoretical data are plotted. The theoretical and experimental sensitivity found are 35.77 deg/RIU (41×10^3 pix / RIU) and 33.20 deg / RIU (39×10^3 pix / RIU), respectively.

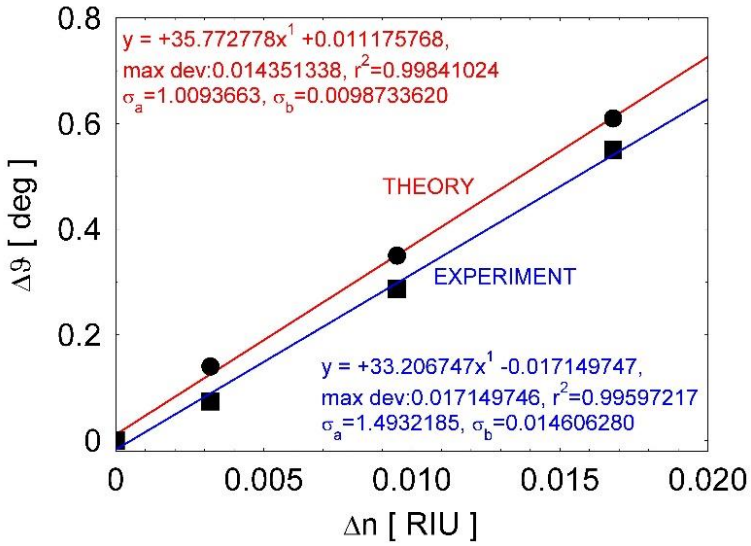

Figure 4.11 - Comparison of theoretical and experimental sensitivity.

The experimental sensitivity differs from the theoretical only for 7%. This is an acceptable value, since one must always take into account the measurement uncertainty, related to the instrument, the operator, the temperature and the wavelength variations. Once obtained the sensitivity, the FoM, described in Section 1, can be easily calculated. In order to get the resonance parameters, deriving the values of D and W (see Fig. 4.12), an averaged reflectance profile is needed. To do that a 2D reflectance map is selected in DI-water at T = 30°C. From such a 2D map one can consider a central slice (two light red horizontal lines in Fig.4.12). The resonance profile and the fundamental parameters needed to FoM calculation are shown in Fig. 4.12.

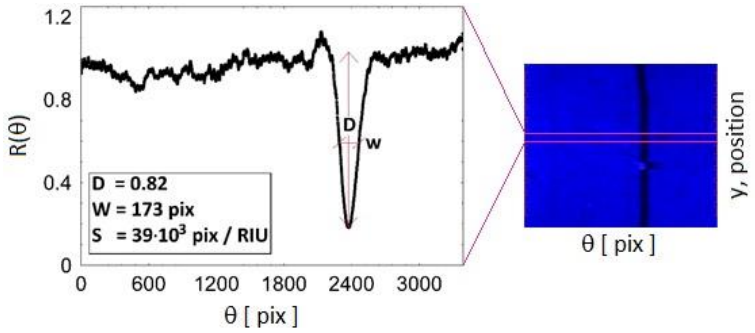

Figure 4.12–Experimental resonance parameters. The averaged reflectance profile (left) is extracted from a central slice of the 2D reflectance map (right).

By substituting these parameters we obtain a FoM:

$$FoM = S \cdot \frac{D}{W} = 184\ RIU^{-1} \tag{4.2}$$

It has to be noticed that, in principle, the FoMs obtained using the same 1DPC geometry in identical optical configuration but different set-ups should not differ. A slightly difference can be attributed to the different substrate on which the 1DPC is deposited. As shown in previous work, 1DPCs deposited on glass could perform better in terms of FoM and LoD [7].

4.3.2 Fluorescence mode

As already explained in Section 3, the S2 instrument can operate in fluorescence mode. Analogously to S1, a simplify protocol is developed to test the fluorescence detection mode. A chemically modified biochip by means of a glutaraldehyde layer (explained in detail in the following Chapter 5) is then washed with 500µL of D-PBS 1X and the baseline was acquired for 5min. After that, the florescence mode is switched on. At the beginning of the experiment, before the dye injection, a scan at different angular positions that ranges from 0 mm to 12 mm

(see Chapter 3) is carried out in order to find the maximum of the fluorescence intensity, exciting the dye resonantly. The recorded backgrounds are acquired at resonance position for different integration times ranging from 5×10^{-4} s to 1×10^{-1} s. After the dye injection, which has an excitation and emission wavelength of 652 nm ± 4nm and 672 nm ±4 nm, respectively, the fluorescence signals were then collected at the resonance and with the same integration times (5×10^{-4} s to 1×10^{-1} s). In Fig. 4.13, the background subtracted signals are plotted as function of the integration time.

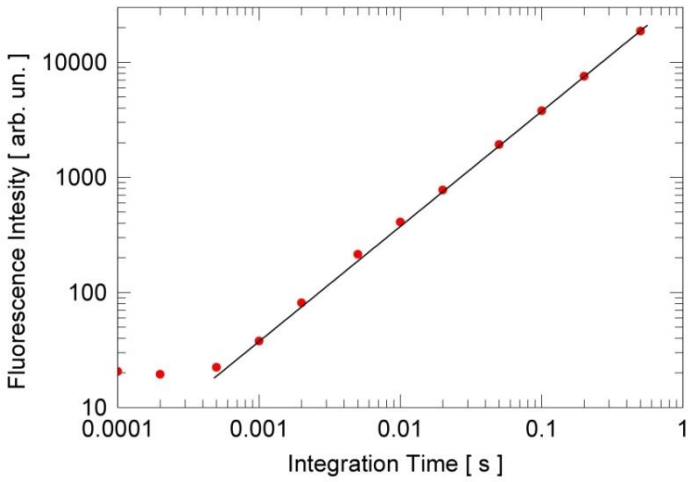

Figure 4.13 – Fluorescence signal background subtracted signal vs integration time.

The fluorescence signals show a linear dependence on integration time, for integration times greater than 1×10^{-3}s. Therefore, integration time greater than this value will be chosen in the following measures. This characterization allowed to determine the range of integration times in which the CCD signals are linear. Therefore, the fit range and the CCD parameters are kept constant during the whole experiment. There is also another strategy to get the backgrounds. Instead of acquiring the backgrounds before the dye injection at the resonance position, these can be taken after the dye injection at a position off-resonance.

As shown in Fig. 4.14, both backgrounds, at resonance (blue spectrum) and off-resonance (red spectrum), approximately lie on the same level. The difference between the two backgrounds could be due to a residual fluorescence signal coming from the dye layer.

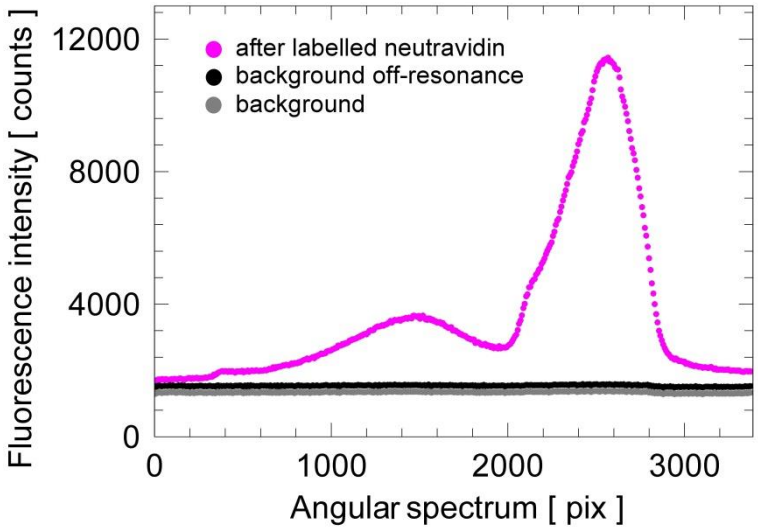

Figure 4.14 – Fluorescence signal and backgrounds

One could normalize either taking into account the off- resonance or the standard background. In this work, I usually made use of the standard background because this normalization procedure avoids irradiating the dye before the experiment starts. This leads to an increase of the dye lifetime that can be decreased by photobleaching. On the other hand, the off- resonance background sometimes may be convenient used because of it takes into account the presence of the dye at the biochip surface (in an off-resonance position).

4.5 EXPERIMENTAL CHARACTERIZATION OF THE LoD

The resolution or limit of detection (LoD) of the our platforms is directly related to the noise of the measurement of the BSW resonance position. In the Chapter 1, the LoD is defined as the minimum change of the refractive index of the external analyte that can be revealed by the measuring platform. According to such definition LoD = σ/S_V, where σ is the standard deviation of the noise and S_V is the volume sensitivity. The LoD depends on the optical design of the platform and on the design characteristics of the particular 1DPC biochip. We carried out an extended study on the noise of the BSW resonance position measurement in order to determine the experimental LoD. Such investigations were carried out by using 1DPC biochips of the A|13|634 family. Such biochips were designed in order to optimize both the label-free and the fluorescence operation of the platform and are characterized by a relatively wide resonance.

The angular position of the BSW resonance was tracked by means of the apparatus (S1) described in Chapter 3. The A|13|634 test biochip was measured in the pure TE configuration at λ_0 = 670 nm. The temperature of the biochip was stabilized at 26°C (±0.01°C). During the

measurements the 8bit CMOS camera was sampling the reflected beam at the rate of 15 frames per second.

In Fig. 4.15, we show the real time operation of the noise measurement LabView code. Two portions of the CMOS image of the angular reflectance pattern are selected (blue images). Each of them is 100 pixel high and corresponds to a spot on the surface of the biochip that is about 0.4mm wide. In all graphs the abscissa is the angle in pixel units (the span corresponds to 1deg).

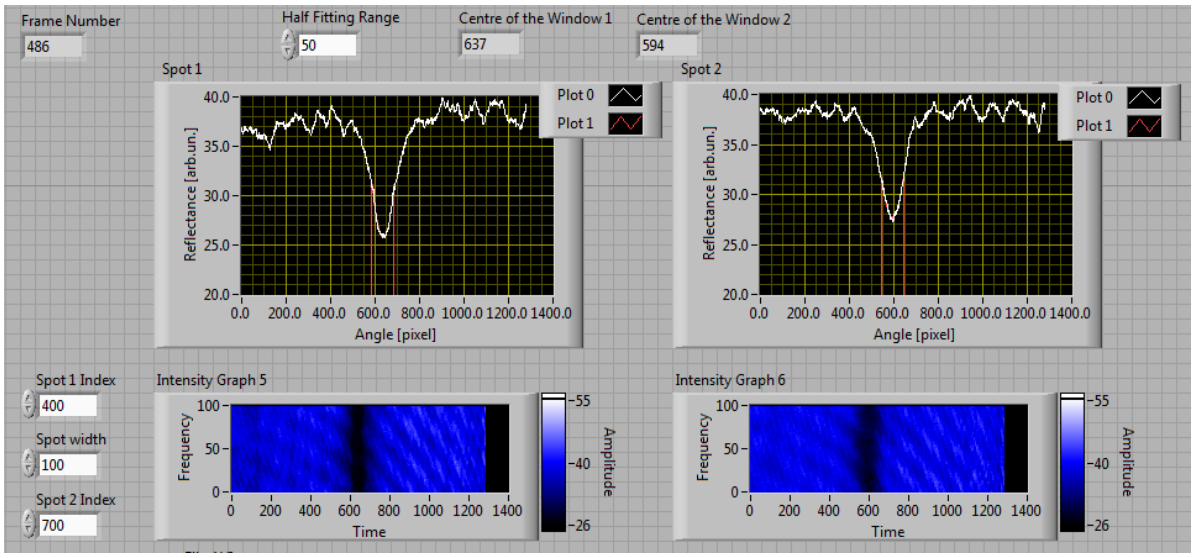

Figure 4.15 - BSW resonance position tracking and evaluation of noise. The two bottom images correspond to two portions of the CMOS array detector, each 100 pixel high; they correspond to two different spots on the sample surface. The corresponding top graph are the plots of the reflectance averaged over the 100 lines constituting each spot.

The angular reflectance is averaged on the 100 lines for each of the two spots (plots) and the BSW resonance is fitted in an interval around the minimum with a parabolic fit. The fitting half range was set to 20, 30, 40, 50 pix.

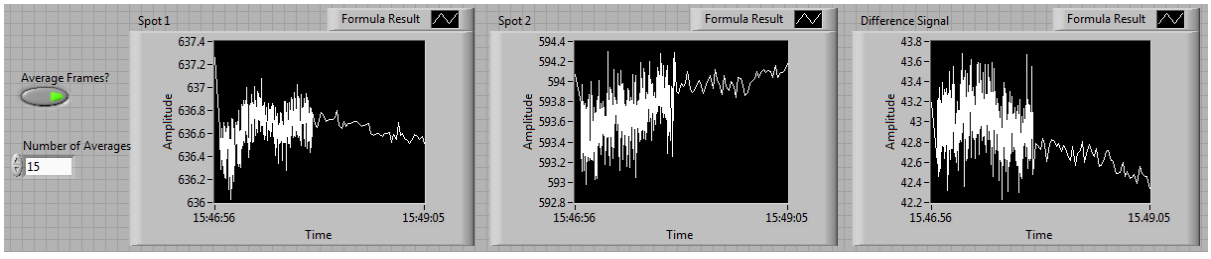

Figure 4.16 - Temporal dependence of the BSW resonance angular position for the two measurement spots and time dependence of the difference signal. The first part of the plots was obtained by fitting one single CMOS frame at a time, the second part by averaging 15 frame and then fitting; noise reduction is the consequence.

In Fig. 4.16 we show the temporal dependence of the BSW resonance angular position (in pixel) in the two measurement spots and the temporal dependence of the difference signal. Given that in the S1 and S3 platforms referencing is adopted in order to rule out parasitic drifts of the BSW resonance position the noise of the difference signal was analyzed and used to evaluate the LoD. The standard deviation of the noise was evaluated from the plot of the difference signal as a function of time on a convenient time slot, for several different fitting ranges (20 to 50) and frame averaging N_{av} (1 to 10).

In Fig. 4.17 we show the result of the analysis. The standard deviation of the noise σ_{NOISE} evaluated from the measurements shown in Fig. 4.16, is plotted as a function of the number of averaged images N_{av} for several different fitting ranges. σ_{NOISE} improves when increasing the fitting range up to the 40 pixel value; after such a limit the range is so large that the parabolic fit is not anymore appropriate and the noise increases. The dependency on N_{av} is well described by the equation:

$$\sigma_{NOISE} = \frac{a}{\sqrt{N_{AV}}} + \sigma_0 \qquad (4.3)$$

corresponding to the solid curves in Fig. 4.17. Extrapolating the curves to N_{av}=15, corresponding to a 1s CMOS sampling time and 1Hz frequency, and in the 40 pixel fitting range case one finds σ_{NOISE}(1Hz) = 0.057pix. Given that for the A|13|634 family we previously estimated the sensitivity S_V=31.8 deg / RIU= 40700 pix / RIU (see above in Paragraph 4.3.1) we get LoD(1Hz) = σ_{NOISE}(1Hz)/S_V= 0.057 / 40700 = 1.4E-6 RIU.

The LoD found above is obtained for a given design of the 1DPC (A|13|634) whose resonance width was purposely widened to improve the fluorescence excitation and collection. Reducing the BSW resonance width can lead to a decrease of the LoD. In order to improve the LoD, keeping the 1DPC design as it is, we decided to increase the number of bits of the camera passing from a CMOS 8bits to a CCD camera with 12bits.

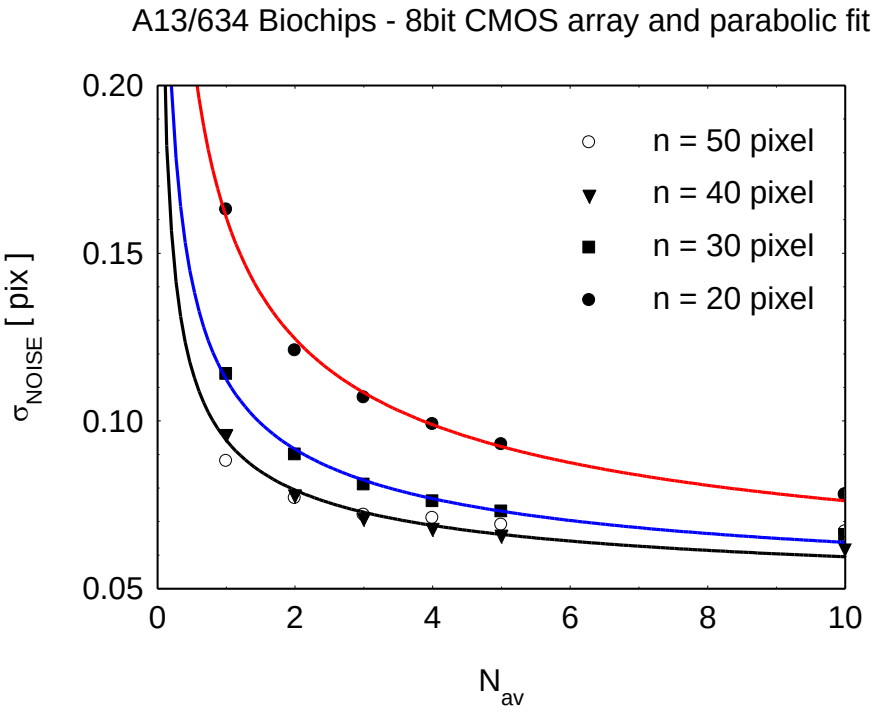

Figure 4.17 – Dependency of the standard deviation of the BSW angular position noise as a function of the number of averaged CMOS images and fitting range.

CHAPTER 5
Chemical functionalization strategies

To achieve a versatile approach for detection, the 1DPC surface should be properly functionalized prior to the recognition molecule conjugation. In this section, we examine both wet functionalization and plasma polymerization deposition techniques for introducing chemical functionalities on the BSW surface that would attach the capturing molecules.
This chapter is fully devoted to surface modification of the sensing surface by means of standard reaction procedures. The main functionalization route used in this work consists in a silanization process followed by an activation step through glutaraldehyde. The final functionalization protocol was carried out through a collaboration between SAPIENZA, Imperial College of London and Fraunhofer-IWS. The basics of reactions are described in details leaving the bio-conjugation step to Chapter 6, because of its variability depending on the application. Moreover, in the last part, an alternative functionalization route based on polymerized poly-acrylic acid coatings is illustrated.

5.1 Functionalization using APTES and Glutaraldehyde: Strategy A

The main functionalization route used in this work involves APTES ((3-amino)propyl-triethoxysilane) chemistry. This strategy is particularly appealing for antibody immobilization, due in part to many advances in the understanding of this class of surface modification agents. APTES can readily react with hydroxyl groups and can support the formation of monolayer coverage under carefully controlled conditions [39-42]. Modification of the surfaces through APTES chemistry results in amino functional group that can be readily conjugated to a chemical agent that would lead to crosslinking with the protein of interest. Conditions for the reaction of APTES with surfaces change in the literature from anhydrous environments to aqueous solutions. The presence of water catalyzes hydrolysis of ethoxy groups (see Fig.5.1), leading to dehydratation and the formation of a siloxane bond between APTES and a surface hydroxyl group, resulting in multilayer formation.

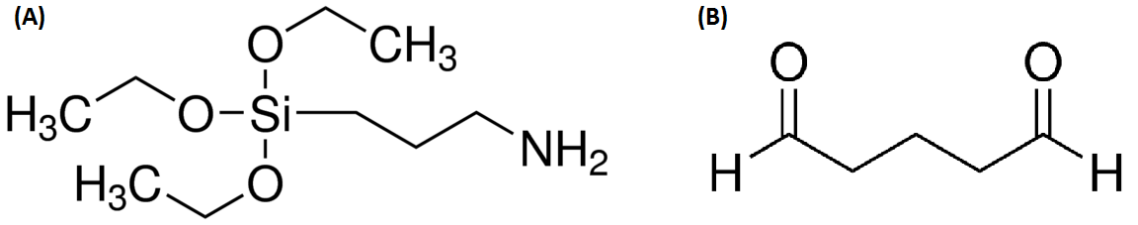

Figure 5.1 – (A) (3-amino)propyl-triethoxysilane and (B) glutaraldehyde molecules.

The functionalization protocol consists in a first cleaning of the bare BSW chips in piranha solution (3:1 mixture of sulfuric acid and 30 % hydrogen peroxide) for 10 minutes. This step is crucial for following steps because it is necessary to have a large density of OH groups at surface before silanization. The chips are then rinsed thoroughly with de-ionized (DI) water and dried under a stream of nitrogen gas, to remove of all organic contaminants and expose hydroxyl groups for the following functionalization step. In order to have primary amines at the BSW surface, the chips are immersed into a 2 % solution of APTES in ethanol/water (95:5 v/v) mixture at room temperature (RT) for 1h.

The chips are then removed from the APTES solution, sonicated, rinsed with ethanol and baked on a hot plate at 110 °C for 1 h. An optimum temperature and duration of the curing step permits to obtain an APTES-modified chip that is more stable and compact.

The activation of silane with glutaraldehyde (GAH) is a standard procedure in surface preparation.

GAH reacts directly with APTES by the formation of a Schiff base. The use of a mild reducing agent, such as sodium cyanoborohydride, reduces the unstable imine bond formed between the primary amino group of APTES and the aldehyde group of glutaraldehyde. Accordingly, the BSW chips are allowed to react with 1 % (v/v) glutaraldehyde in 100 mM sodium bicarbonate buffer (pH 8.5) in the presence of 0.1 mM sodium cyanoborohydride for 1 h at RT.

This reaction requires basic catalysis (in our case pH 8.5), as the APTES amine must be unprotonated to react. Further incubation of the substrate with a protein solution at basic pH conditions results in the formation of a second Schiff base. With time, the unstable Schiff bases undergo complex reactions. Therefore, reduction with the same reduction agents to increase stability is unnecessary when long incubation times are used [43].

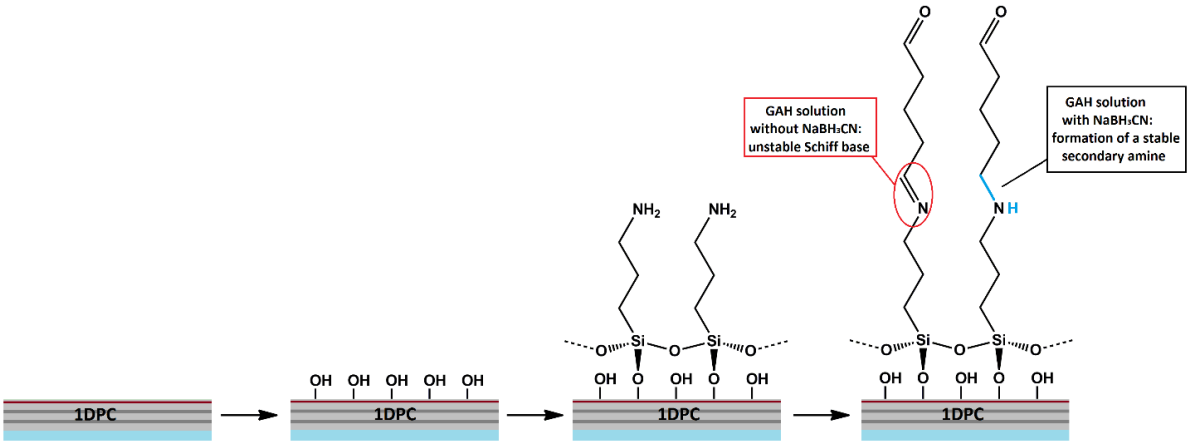

Figure 5.2 – Surface modification scheme.

After the GAH activation step, a further sonication and rinsing step in DI water are performed. This step permits to remove non-covalently adsorbed GAH molecules from the activated 1DPC surface. At this point, the BSW chips can be stored in a dessicator or directly bio-conjugated with the protein of interest.

The immobilization of proteins to glutaraldehyde-activated substrates results in the formation of some linkages that are stable even to acid hydrolysis. The reaction of glutaraldehyde with proteins is complex, but in most proposed mechanisms proceeds, again, through a Schiff base (imine) intermediate, which should be stabilized by reduction. Reduction with sodium borohydride, however, does not usually increase the amount of proteins/antibodies irreversibly bound to the support. For stabilization of the imine bond, sodium boro-hydride must be added after the immobilization is complete, in order to avoid destroying the aldehyde functions with which the enzyme reacts. By contrast, sodium cyanoborohydride ($NaBH_3CN$) reduces aldehydes at a negligible rate under conditions where it reduces Schiff bases rapidly, and it can therefore be present throughout the immobilization, to drive the immobilization to completion by trapping labile Schiff bases by reduction. Because the use of glutaraldehyde for protein immobilization is simple and widely used, a slight modification based on $NaBH_3CN$, would be useful in situ to convert labile Schiff bases formed between protein and support-aldehyde groups to stable secondary amines [39]. A photo collage of a standard APTES-GAH functionalization is shown in Fig.5.3.

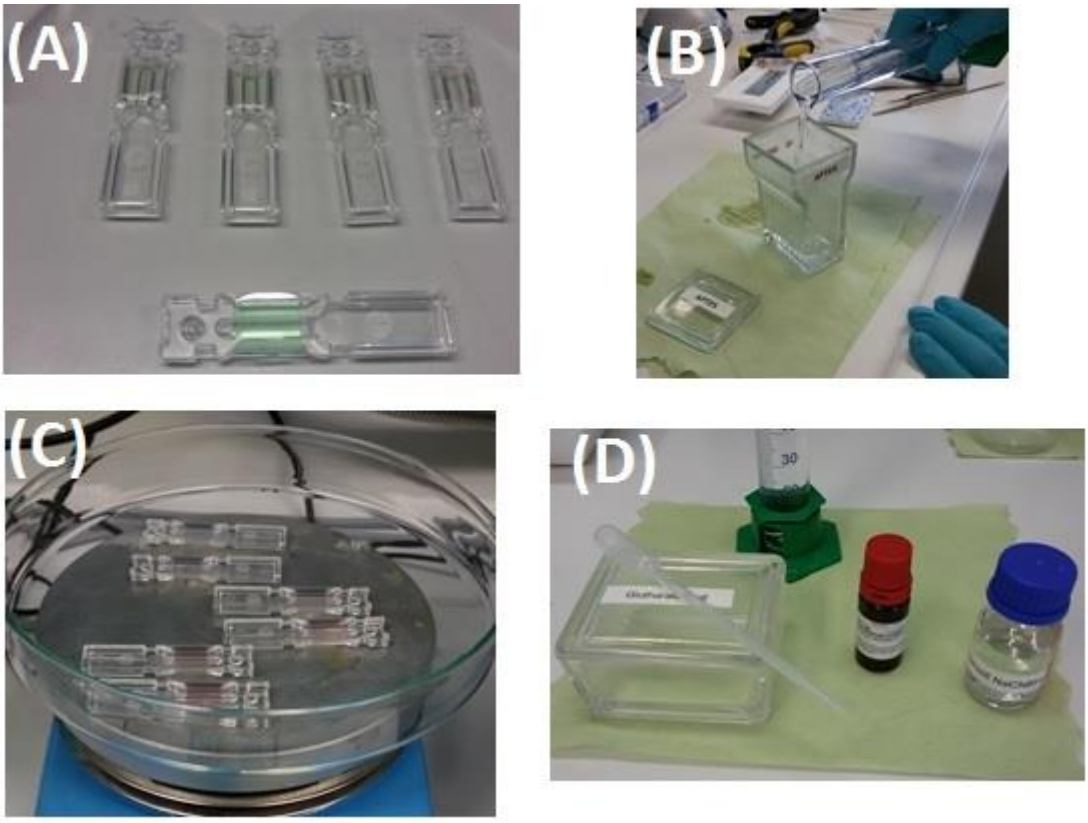

Figure 5.3 – Functionalization steps to produce an APTES-GAH coating on SiO_2 substrate: (A) piranha cleaning; (B) APTES reaction in Et-OH/DI-water environment; (C) hot plate treatment; (D) GAH + Na $CNBH_3$ incubation to form stable –COH functional groups.

Among all possible characterization techniques present at SAPIENZA, we selected water contact angle (WCA) and fluorescence microscopy exploiting our platform S1. As observed from the static WCA, the substrates are very hydrophilic after piranha cleaning with a measured WCA of ~ 8°. The surface hydrophobicity increased significantly after APTES and soft baking treatments with WCA ranging between 55° and 60°. In Fig. 5.4 is shown the behavior of the WCA from one optimized 1DPC during the functionalization process.

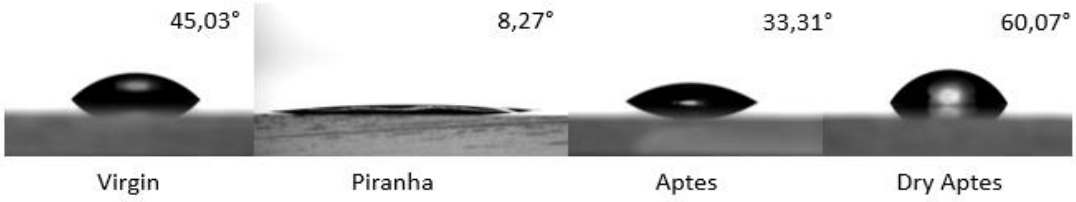

Figure 5.4 - APTES functionalization of 1DPC with SiO_2 outermost layer. Static contact angle of water are measured on surfaces functionalized with 2% APTES (v/v) during preparation. From the left to the

right: bare chip without any cleaning procedure, chip after piranha cleaning, chip after APTES functionalization and chip with APTES after the hot-plate treatment.

To further characterize the APTES-modified surfaces we made use of the extended laboratory test bench described in Section 3. In order to verify the presence of primary amine at the end of the APTES step, a reduced interaction protocol has been developed. The sensitive area of the APTES modified chips are divided in two regions, where two different molecules are allowed to react with the surface. The two regions, named signal and reference, are treated either with a biotinylated cross-linker (EZ-Link® Sulfo-NHS-LC-Biotin) or a bovine serum albumin (BSA), respectively. After incubating for 1 h at RT, the BSW biochips are rinsed with D-PBS 1X (Dulbecco's Phosphate Buffer Saline) and blocked with a BSA solution on both regions at +4°C overnight. The biochips are then thoroughly rinsed with D-PBS 1X and mounted on the S1 platform. Once obtained a stable baseline in D-PBS 1X (see #1 in Fig. 5.5), a solution of Neutravidin conjugated with DyLight 650 (from ThermoFisher Scientific, cod. 84607) is injected at a concentration of 2.5 μg/mL. The conjugated neutravidin binds only to the region where the biotin is present (signal region) and not in the BSA region (reference region).

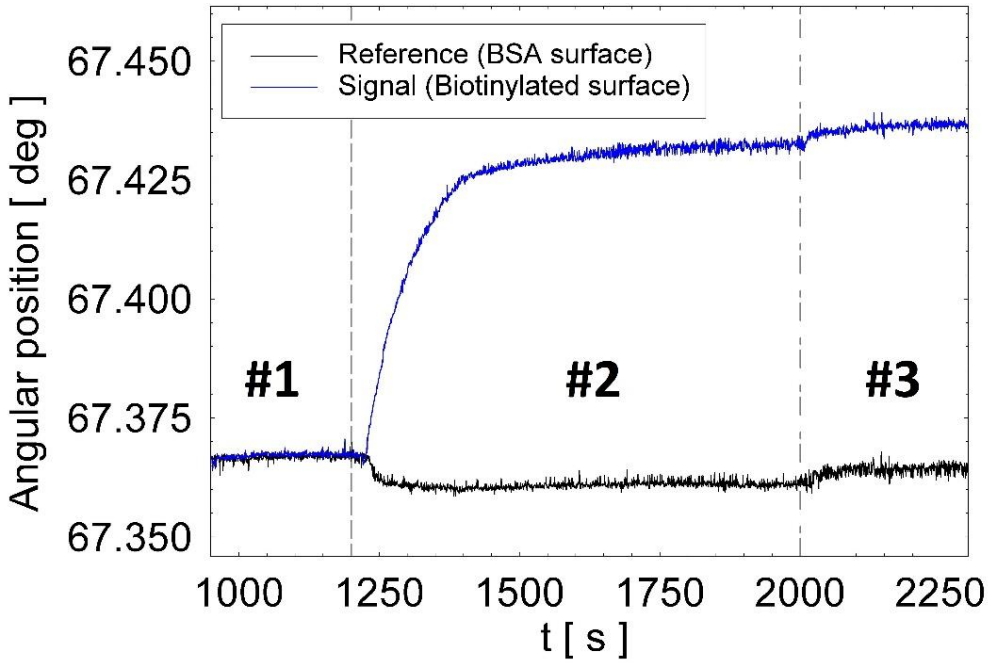

Figure 5.5 – Label-free kinetics of Neutravidin DyLight650 on biotinylated (blue) and blocked (black) regions.

The kinetic curve and the flat response in the reference spot (see #2 in Fig.5.5) demonstrate the specificity of the interaction on the biotinylated region. After washing with D-PBS 1X, the BSW biochip is ready for fluorescence detection (#3 in Fig.5.5). As widely described in Section 4, the platforms used in this work have the possibility to detect the presence of fluorescent molecules bound at the 1DPC surface. With this aim, fluorescence spectra are acquired and analyzed in both regions. As shown in Fig. 5.6 a sharp difference can be noted in the fluorescence spectra coming from the two regions.

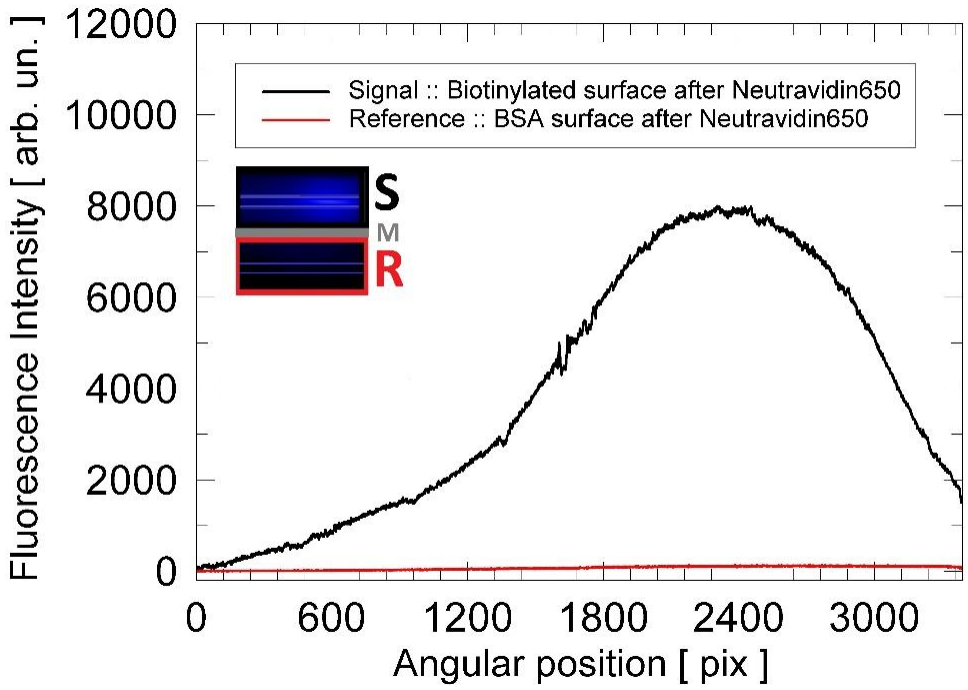

Figure 5.6 – Averaged spectra from the signal (black) and reference (red) regions.

Similar to a fluorescence microscope image (see the inset in Fig.5.6), such a fluorescence map confirms the quality of the APTES-modified surface obtained with the procedure described above. As discussed in the introduction, in the present Chapter we describe all the functionalization steps up to proteins/antibodies bio-conjugation (see Fig.5.7). The bio-conjugation strategies will be considered case by case in Chapter 6.

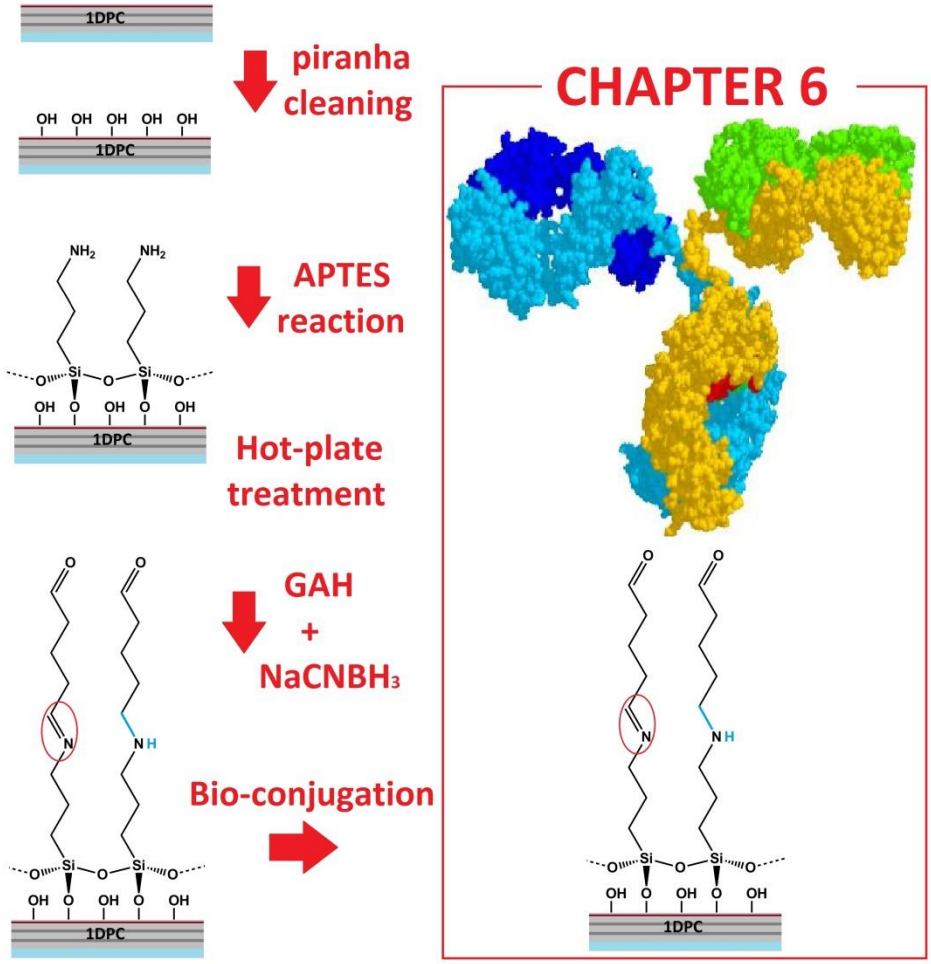

Figure 5.7 – Schematic representation of the functionalization steps described in the present Chapter. The bio-conjugation procedure will be discussed in Chapter 6.

5.2 Functionalization using polymerized poly-acrylic acid: Strategy B

In this paragraph, a plasma polymerization deposition technology for introducing carboxylic chemical functionalities on the BSW surface is presented. This technology was developed at Polytechnic University of Turin and used to coat with plasma polymerized acrylic acid (ppAA) the optimized 1DPCs for bio-sensing experiments. In order to keep the optimized 1DPC design (family A|13|634), we decided to fabricate optimized stacks without the last 20 nm of SiO_2 topping layer. The main reason was to optically compensate (removing the SiO_2 top layer) for the polymer thin layer deposited on top of the 1DPC. In fact, the new family of 1DPCs named A|14|141 was constituted by an optimized 1DPC without the 20 nm of SiO_2 with the possibility to deposit up to 40 nm of ppAA. The optical characteristics in terms of resonance parameters and LoD did not dramatically differ with respect to the optimized 1DPC.

In plasma polymerization, the transformation of low-molecular-weight molecules (monomers) into high-molecular-weight molecules (polymers) occurs with the assistance of energetic plasma species such as electrons, ions, and radicals. Plasma polymerized polymer coatings can show different chemical compositions as well as chemical and physical properties from those formed by conventional polymerization, even starting from the same monomer. The unique feature of such a technique exploits the reaction mechanism of the polymer-forming process that makes use of radicals and ions. The most studied polymers in biomedical and sensing applications, provide as functional groups mainly carboxyls (-COOH) [44] and amines (-NH2) [45], hydroxyls (-OH), and aldehydes (-CHO).

Moreover, in order to tune the density of reactive groups at the surface, there is also the possibility to mix functional monomers with neutral precursors to obtain plasma co-polymerized coatings. Recently, some authors reported on co-polymer substrates with excellent ability to support the growth of human cell lines [46]. In order to further optimize the properties of coatings and surface structures, the plasma can be engineered, making use of pulsed radio-frequency-excited plasmas. This particular technique allows to control plasma parameters through manipulation of the pulse waveform (duty cycle), optimizing the desired chemical groups at the surface. Also the geometry of reactor used for the processes (shape and volumes of the reaction vessel, geometrical location of electrodes and substrates, etc.) and the selected experimental conditions (pressure, power, flow rates of gases, temperature of the substrates, etc.) crucially influence the gas-phase and surface-related plasma chemistry, that is, the modalities of transferring electric or electromagnetic field intensities to the reaction systems. The plant makes use of a system equipped by 4 different gas/vapour lines, one connected directly to the deposition chamber and the other ones intercepted by the corresponding reservoirs used for the storage of the liquid monomers (see Fig. 5.8).

Two horizontal parallel plates, placed at 4 cm far away from each other, act as electrodes and define the vacuum deposition chamber. The gas carrier (Ar), flows into the line, passes through the reservoir containing the liquid monomer and is bubbled in the liquid.

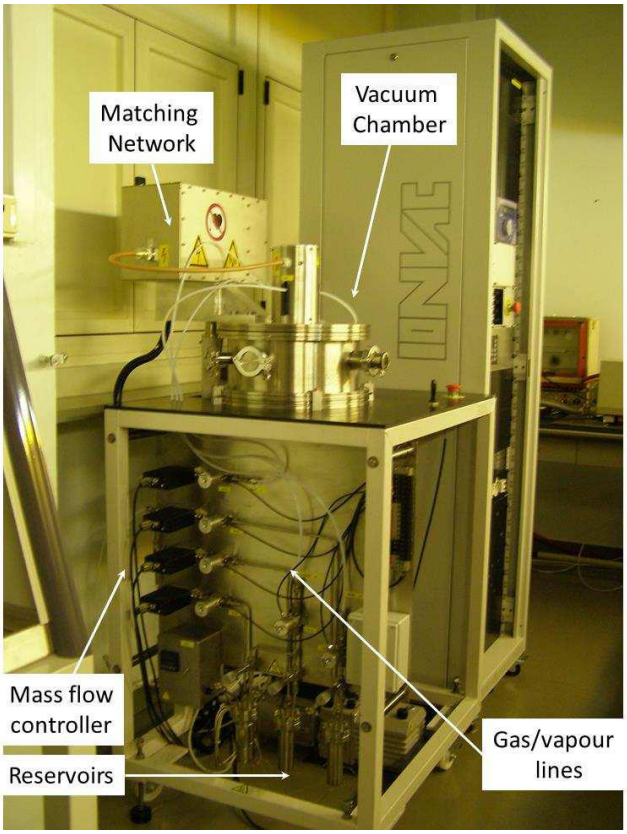

Figure 5.8 – An overview of the Plasma-Polymerization system.

Then, the gas-vapor mixture, passing through its line, is uniformly distributed in the reactor by the upper showerhead electrode. The 1DPC to be coated are placed on a circular sample-holder that corresponds to the grounded electrode and is parallel to the shower electrode.

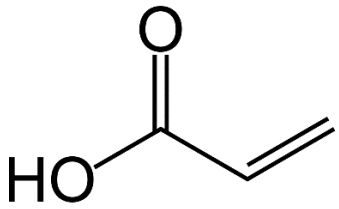

Figure 5.9 – Structure of the acrylic-acid.

As already introduced above, the starting monomer selected for 1DPC coating is pure acrylic acid (AA), anhydrous, 99% liquid monomer (CAS Number 79-10-7) with a vapor pressure of 3.1 Torr at 20C° and 1 atm, (Sigma-Aldrich). The main advantages in selecting such a molecule are the low vapour pressure that permits to control the flux of vapors by the manual metering valve, the nearly absent toxicity of reactants and the presence of carboxylic functionality (-COOH in Fig. 5.9). Such chemical groups provide suitable anchoring system for bio-sensing applications because they can easily form amidic bonds by reacting with the amino groups of proteins with (improving binding efficiency) or without further chemical activation.

To obtain thin polymerized film organic vapors together with a carrier gas (Ar o O_2 were used) feed the system after the formation of a mixture. Plasma activation is mediated by a radiofrequency generator working at a fixed frequency of 13.56 MHz and connected to the shower electrode. Such RF plasma discharge (sustained by Ar) promote polymerization of AA gas mixture in a polymerized poly acrylic-acid (ppAA) thin film. Among ppAA coatings obtained by tuning RF starting power, duty cycle, wave period, carrier gas (Ar and oxygen for adhesion promoting pre-deposition treatment of substrate surface), the optimal conditions for the plasma process are given in Table V.I. Under these conditions, a ppAA growth rate of 8.5-10 nm / min can be obtained.

Monomer	**P_{RF}**	***D.C.***	**t_{on}**	**t_{off}**	**P_{AVE}**	**Thickness**	**Time**
	Watt	**%**	**Ms**	**ms**	**Watt**	**nm**	**min**
Acrylic Acid	200	10	10	90	20	30/50	3.5/5

Table V.I - Selected ppAA process for further study and optimization for BSW biochips

In this experimental work, more than 30 1DPCs were coated and used for sensing characterizations. The ppAA coated 1DPCs (family A|14|141) were extensively used in the first part of the doctorate period to better understand protein interactions. Due to its simple activation chemistry, based on EDC (1-Ethyl-3-(3-dimethylaminopropyl) carbodiimide) and Sulfo-NHS (N-hydroxysulfosuccinimide), ppAA coatings were used to study interactions between protein G and capturing antibodies. As an example, in Fig 5.10 is reported a sensogram showing the time dependence of the BSW resonance angular position in a biosensing test with orienting protein G (PtG) and a gamma globulin 1 (IgG1). The experiment was performed in D-PBS 1X environment. With the aim to better understand regeneration of protein surfaces, injections of glycine with hydrogen chloride were used to test the reusability of the protein G orienting layer. Nevertheless, in Chapter 6, an application of ppAA coatings in cancer biomarkers detection is reported. The characterization of such thin polymeric films are carried out by means contact angle, FTIR-ATR spectroscopy, and fluorescence microscopy.

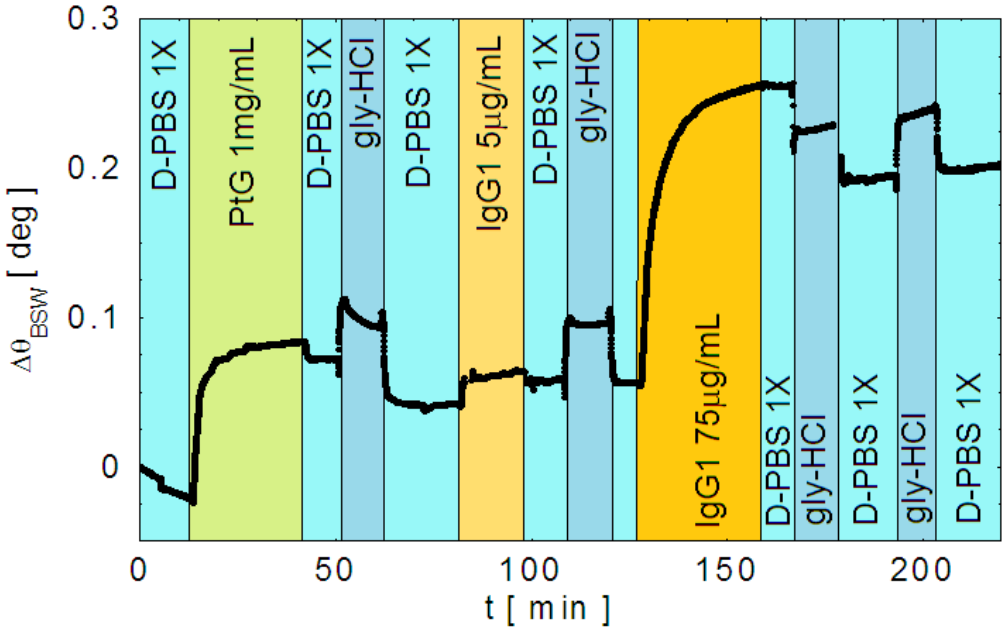

Figure 5.10 - Time dependence of the BSW resonance angular position in a bio-sensing test with PtG and IgG1. The injection of a large IgG1 concentration makes the recovery not possible, keeping the resonance position far from the PtG level in D-PBS 1X.

As an example, in Fig. 5.11 it is shown a typical FTIR spectrum (A) and a fluorescence investigation (B). From the infrared spectrum it is possible to see a new peak related to the presence of –COOH groups at the surface (red circle in Fig-5.11A).

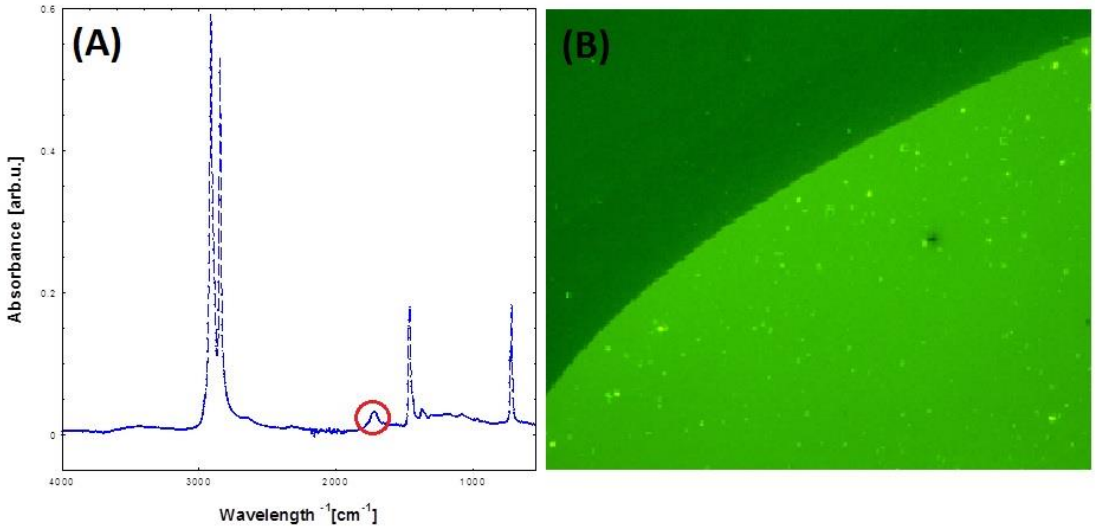

Figure 5.11 –(A) Typical FTIR spectrum with a new band (red circle) introduced by ppAA thin film; (B) Fluorescence image that shows –COOH groups binding of PtA-Alexa 546 (bottom right-hand side). In the up left-hand side region of the image, where PtA-Alexa 546 was not incubated, is possible to observe ppAA auto-fluorescence.

As further confirmation of the plasma process, the ppAA surface is allowed to react for 30 minutes with a solution of Protein A (PtA) labelled with a fluorescent marker (Alexa Fluor 546) with a 0.1 mg/ml w/v concentration (volume dispensed=10 μL). Finally, the samples were rinsed in D-PBS 1X and DI-water to remove unspecific protein, physisorbed on the surface, then it was dried under N_2 flux and observed by fluorescence microscopy (see Fig. 5.11B). The image is taken across the edge of the incubated drop. This technique permitted to quantify the content of carboxylic ($1.15 \pm 0.35 \times 10^{16}$groups/cm^2) functionalities confirming the possibility to produce coatings with high density of –COOH groups.

CHAPTER 6
Applications to cancer biomarker detection

The increasing demand for non-invasive early detection of diseases has pushed the scientific community to develop more and more sensitive techniques to detect disease biomarkers in extremely low concentrations. Among other techniques, optical label-free bio-sensing is considered to be the most promising tool for high throughput detection of biomolecules. In this work, molecules of clinical interest are detected in different biological environments by means of the platforms S1 and S3. In particular, we focused our attention on two classes of molecules: angiopoietins and human epidermal growth factor receptors (ERBB2). Angiopoietin-1 (Ang 1) and angiopoietin-2 (Ang 2) are important regulators of endothelial cell (EC) survival. Current models suggest that an increase in Ang 2 expression in ECs leads to the initiation of angiogenesis. Indeed, the imbalance of Ang 1 and Ang 2 activities in colon carcinoma leads to a net gain in Ang 2. For this reason, Angiopoietin 2 became a clinical marker for angiogenesis and early stage cancer development in adults [46,48].

On the other hand, ERBB2 (also known as Neu, or HER2) is a Tyrosine Kinase (TK) receptor acting as the master integrator of epidermal growth factor receptor (EGFR) signalling, regulating a variety of cell proliferation, growth and differentiation pathways. ERBB2 gene amplification/over-expression occurs in approximately 20% to 30% of breast cancers and until recently this genetic lesion was associated with a dismal prognosis [49,50]. In this context, the platforms developed in this work can find a useful application in pre-clinical/clinical environment improving the standard techniques routinely used for diagnostics.

In this Chapter, the Section 6.1 is dedicated to the first experiment reported in literature showing simultaneous operation in both label-free and fluorescence modes obtained on platform S2. The two modes operate in the near-infrared spectral range with the same configuration of the optical reading apparatus. In the second Section, we make use of an ellipsometric detection scheme (platform S1, described in Chapter 3) to sense Angiopoietin 2

dissolved in BSA solutions. A characterization of the ellipsometric operation is given in order to better explain the sensing principles.

The following Sections describe bio-sensing experiments involving Angiopoietin 2 and ERBB2 in different biological environments, from simple D-PBS 1X buffer to complex cell lysates. The detection platforms (optical schemes) and the functionalization routes are described in Chapter 3 and 5, respectively. In these Sections we leave space to bio-conjugation strategies and bio-sensing experiments that can differ in the different measurements.

6.1 Combined label-free and fluorescence operation on platform S2

In order to validate combined label-free and fluorescence operation I made use of the platform S2. As shown in Fig. 6.1 (top), the reflectance is measured at λ_0 = 804 nm ($\Delta\lambda$ = 2.5 nm, spectrally filtered LED illumination) in the $\theta \in [63.2°; 67.2]$ angular range above the total internal reflection (TIR) edge (details in Chapter 3). In this experiment, either ethanol (EtOH) or DI-water is the external liquid (n_{EtOH} = 1.357, $n_{DI\text{-}water}$ = 1.328 [51]) with the TIR edge situated at θ_{TIR} = 62.73° or θ_{TIR} = 60.87°, respectively. The 1DPC used in the experiments were deposited on 170 μm thick microscope cover slides (Menzel Gläser) by PIAD as described in Chapter 4. SiO_2 and Ta_2O_5 are used as low and high index layers with complex refractive indices n_L= 1.454 + j 6E-6 and n_H = 2.060 + j 2E-5 at λ_0, respectively.

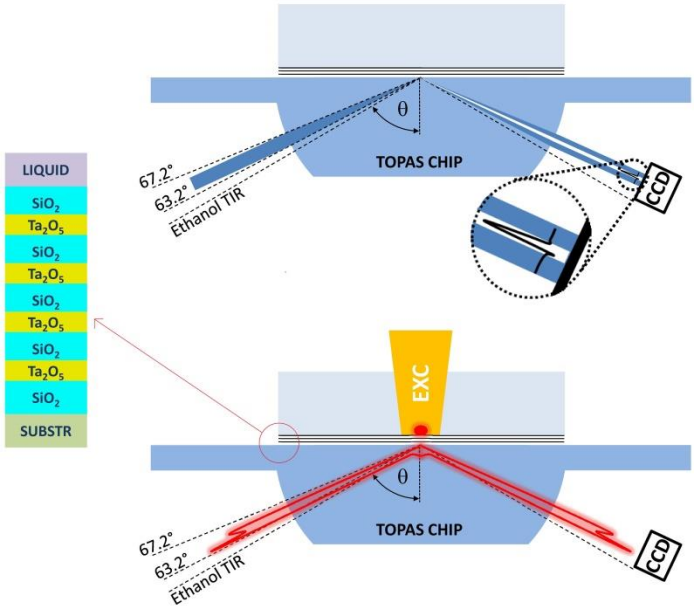

Figure 6.1 - Sketches of the label-free (top) and fluorescence (bottom) modes of operation of the sensing platform. (Top) A focused beam at λ_0 is used to illuminate the chip under total internal reflection conditions, and the presence of resonance is detected by a CCD sensor. (Bottom) An external laser beam at λ_{EXC} is used to excite molecules in the proximity of the chip surface and the emission, strongly

coupled to the BSW surface-bound modes, is directed into a narrow angular range and detected by the same CCD sensor. (Left) Sketch of the 1DPC geometry used in the experiments (not to scale).

Starting from n_L and n_H, we designed the thicknesses of the 1DPC layers in order to obtain a BSW resonance inside the angular acceptance range of our optical reading system. As a result, the 1DPCs designed, fabricated, and used in the experiments had the structure substrate∕L(HL)^4∕EtOH with design thicknesses d_H =170 nm and d_L = 495 nm. The last layer in the stack, which is in contact with the external liquid, is SiO_2. The first L layer was deposited in order to provide a defined surface quality for the growth of the 1DPC. The layers' deposition tolerance (± 2% thickness) ensures that the BSW resonance is within an angular range of 0.2° around the nominal angular position. The peculiarity of the present design is that the 1DPC sustains both a TE- and a TM-polarized BSW. Such a condition cannot be achieved with SPP that are only TM polarized.

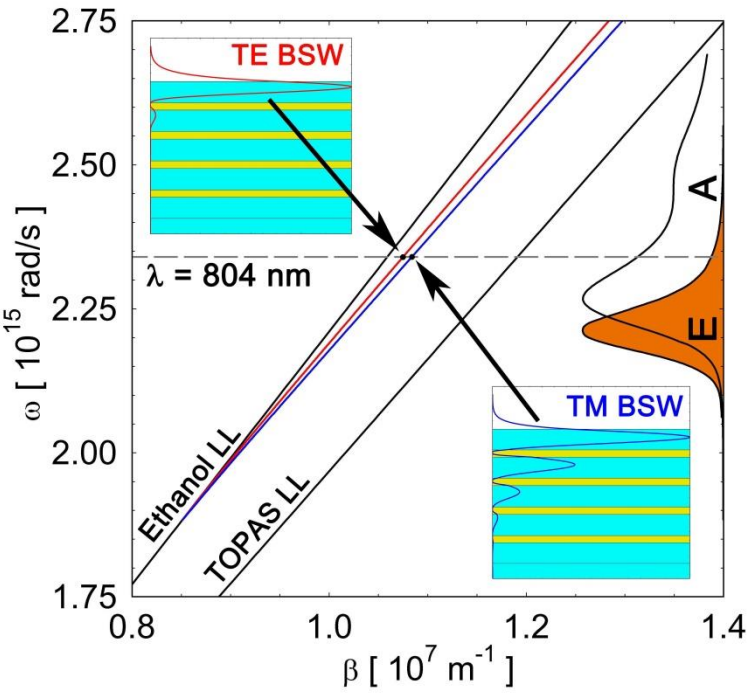

Figure 6.2 - Dispersion relations ω(β) for the TE- and the TM-polarized BSW sustained in EtOH by the 1DPC described in the text. For small ω, the dispersions get to the light line in ethanol (Ethanol LL). (Insets) Normalized $|E|^2$ and $|H|^2$ transverse distributions for both modes. The absorption and emission spectra of the Cy7-VG20 dye used in the fluorescence experiments are also shown. The dashed line marks the wavelength λ_0 used for the label-free operation.

In Fig. 6.2, we show the dispersion relations for such TE (red) and TM (blue) modes calculated in EtOH by means of a transfer matrix method [6]. The dispersions are plotted in the (ω; β) plane, where ω is the angular frequency and β is the wavevector projection (k_z in Chapter 2)

along the 1DPC surface; the (ω; β) window corresponds to λ ∈ [700 nm; 1000 nm] and θ ∈ [62.8°; 67.5°]. The dispersions always lay between the light lines in EtOH and TOPAS. The insets in Fig. 6.2 illustrate that at λ_0 the BSW energy is confined close to the 1DPC interface to the external medium. As a consequence, the modes' characteristics (effective index, losses, and dispersion relation) are strongly sensitive to the properties of the external medium, making them very promising for label-free biosensing [29,52]. Moreover, an emitter placed in the proximity of the interface can couple very efficiently to such modes. After fabrication, the cover slides with the 1D-PC were adapted to a bare TOPAS chip by means of an index matching oil. The chip was previously thinned to account for the thickness of the cover slide when mounting on the instrumental platform, polished, and topped with a glued 170 μm cover slide in order to prevent damage when using the oil. Alternatively, the 1DPC can be deposited directly on TOPAS chips. Complete sensors were mounted on the instrument to carry out the test of the sensitivity with respect to changes of the external refractive index (label-free operation) and the efficiency to collect the emission of a dye in close proximity of the external interface (fluorescence operation). Concerning the label-free operation, Fig. 6.3 shows angular reflectance R spectra measured at λ_0 either in EtOH or in DI-water solutions, when the polarization is set to TE. In the ethanol environment, the excitation of the TE BSW gives rise to a very narrow dip in the reflection spectrum of 9% depth (D = 0.09) and a full width at half-maximum W = 0.030°. For comparison, at the same λ_0 SPP show resonances with D = 0.76 and W = 1.47° [7]. Here, the small value for D is due to both the small absorption losses in the dielectric stack and the limited line-width Δλ of the illumination system. When fitting the reflectance data, one can retrieve the real thicknesses of the 1DPC layers. We found: substrate / 485.0 nm / 165.0 nm / 496.8 nm / 173.1 nm / 501.5 nm / 174.2 nm / 492.5 nm / 167.8 nm / 486.5 nm / EtOH. In the case of DI-water, the light line is shifted to lower angles, the BSW resonance gets broader and the effect of the illumination line-width is reduced; therefore, the BSW resonance is deeper with D = 0.20 and W = 0.036°. In order to evaluate the volume sensitivity $S_V = d\theta/dn$, we poured onto the sensor's surface several solutions of glucose in DI-water with known concentrations [C]. In Fig. 6.3 (right), we show the BSW resonance position for [C] = 5 wt. % (black dots) and [C] = 10 wt. % (red dots). Assuming that the refractive index change of the solution is related to the concentration by $\Delta n = \alpha \bullet [C]$, with $\alpha = 1.5E^{-3}$ RIU/% [38], we find that S_V = 14.7°/RIU. For comparison, SPP show S_V = 92.7°/RIU at the same λ_0 [7]. However, if we estimate the FoM, that is inversely proportional to the limit of detection of the sensor (LoD), we find that $FoM_{BSW} = 82\ RIU^{-1}$. The comparison of such value with that found for SPP $FoM_{SPP} = 48\ RIU^{-1}$ [7] shows that, for this particular 1DPC design, the LoD is about

two times smaller. However, preliminary studies not reported here indicate that the FoM can be further increased by optimizing the 1DPC design and the angular detection window [54]. Concerning the fluorescence operation of the sensor, we decorated the surface with purposely selected dye molecules. With reference to Fig. 6.1 (bottom), we excited the molecules by an external laser beam at λ_{EXC} and collected the emission in the same angular range as in the label-free mode with the same CCD sensor (operated at a different gain and integration time). This condition is very similar to what one could have when performing an immuno-assay on top of such type of sensor [36] in which some of the antibodies are labelled with a fluorescent tag. As a dye, we selected a cyanine molecule (see inset Fig. 6.4), namely, Cy7-VG20, which shows an emission spectrum in a wavelength range that, via the BSW dispersion, corresponds to surface waves that can be outcoupled in the angular window of the instrument. In Fig. 6.2, we show the absorption and emission spectrum of such a dye.

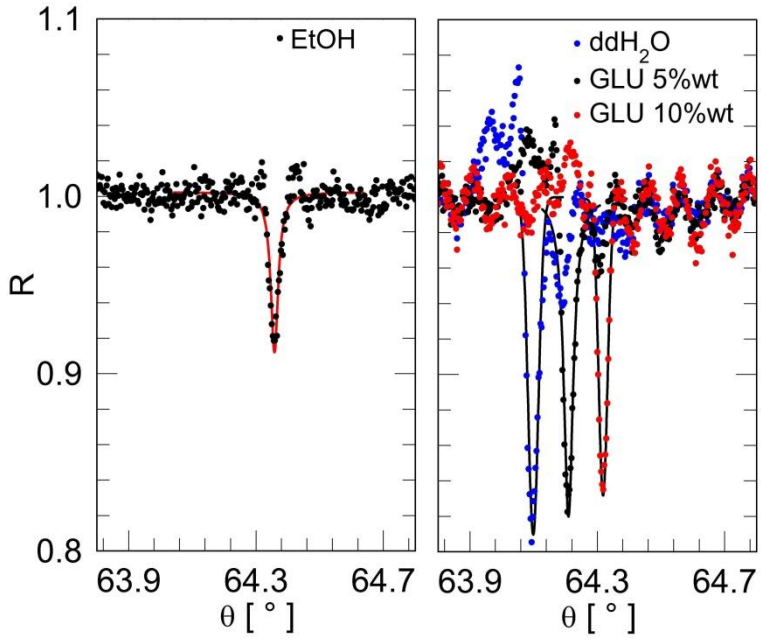

Figure 6.3 - Label-free operation of the sensors at λ_0. The solid lines are guides for the eye. For the sake of clarity, the plots are shown in a reduced angular interval with respect to that taken by the CCD. (Left) BSW resonance measured in EtOH. (Right) BSW resonance measured DI-water (blue dots), 5 wt. % glucose in DI-water (black dots), and 10 wt. % glucose in ddH2O (red dots). The fringes in the measurement are due to interference in the glue layer between the TOPAS substrate and the cover slides.

Coupling of the emission to BSW makes that the peak emission wavelength λ_{peak} = 837 nm corresponds to $\beta = 2\pi/\lambda_{peak} * n_{sub} * \sin(\theta) \sim 1.03E7\ m^{-1}$, i.e., to an angle $\theta \sim 64°$ well in the window. The Cy7 VG20 dye was prepared through a microwave condensation of a quaternized 6-carboxybenz[e]indolenine with N-[5-Anilino-3-chloro-2,4-(propane-1,3-diyl)- 2,4-

pentadiene-1-ylidene]anilinium chloride [55], in the presence of potassium acetate, in EtOH [56]. The obtained crystalline powder was characterized by nuclear magnetic resonance and mass spectrometry. For the fluorescence operation, the sensors were topped with a metal plate with a hole defining a cell located above the sensitive area. The plate was adapted to the surface by means of a VITON o-ring. For surface decoration, the cell was filled with a 1 mM solution of Cy7-VG20 in EtOH, closed by a glass window, and incubated overnight. Before decoration the sensor's surface was cleaned with a piranha solution for 10 min. We tested by the label-free measurement that repeated (>50) piranha cleaning does not affect the BSW resonance characteristics, indicating that the 1DPC geometry and optical quality are preserved (no etching of the last layer and no under-etching, no increase of surface scattering). After incubation, the staining solution was removed from the pool that was then repetitively rinsed with pure EtOH. At the end of the decoration procedure, we filled the pool with pure EtOH and closed it with a glass plate.

The transparent window allows an unfocused laser beam at λ_{EXC} = 632.8 nm (He–Ne, 1 mW at the surface) to reach the 1DPC surface and excite the dye. In Fig. 6.4, we show the angular distribution of the fluorescence collected by the CCD sensor (Sony ICX205AL) when the label-free illumination beam is switched off and the fluorescence excitation beam is switched on. The spectrum was collected with gain G = 600 and integration time 5.1 s; such values must be compared with those used for the label-free operation, G = 374 and τ = 1⁄15 s. The angular spectrum presents two peaks corresponding to the TE- (smaller angles) and TM- (larger angles) polarized BSW. Such angular spectrum has been verified not to change when turning the linear polarization of the excitation beam. We can then assume that the emitting dipoles are isotropically oriented, despite the anisotropic excitation, due to orientational randomization taking place during the molecule's permanence in the excited state. Dipoles can be decomposed into components laying along the 1DPC surface and perpendicular to it. The first will be coupled both to the TE and TM BSW, the second only to the TM BSW. Therefore, the presence of both TE and TM BSW modes allows for an increase of the fluorescence collection efficiency. In Fig. 6.4, we also plot the theoretically predicted angular spectrum of the fluorescence intensity. The calculations are based on a rigorous Green's function approach [33], where we assumed isotropically oriented emitting dipoles uniformly distributed in a 5 nm thick EtOH layer at the surface of the 1DPC. In the calculations, we assumed for the 1D-PC geometry the thicknesses evaluated from the label-free measurement shown in Fig. 6.2 (left)

and the emission spectrum of free Cy7-VG20 in EtOH; we also neglected absorption of the Cy7-VG20 molecules themselves.

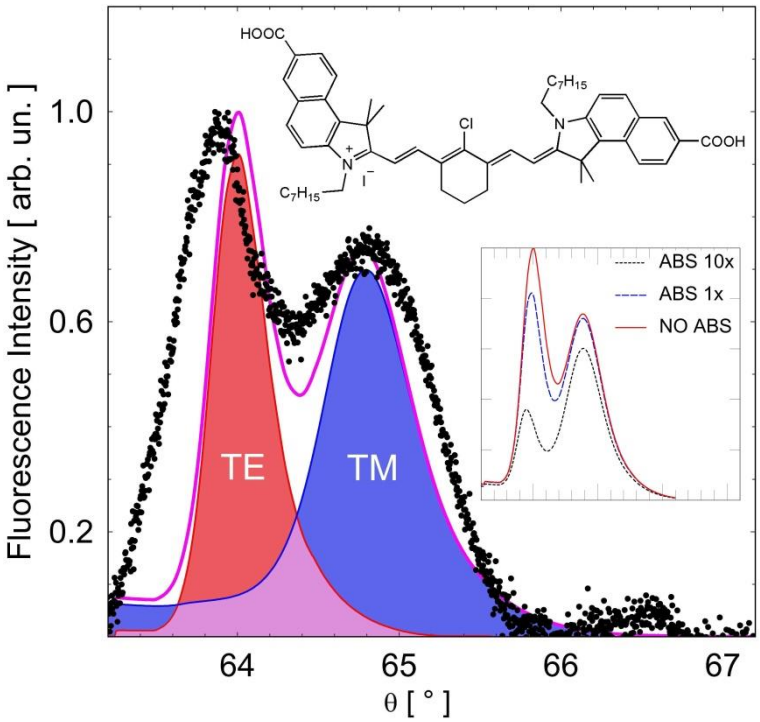

Figure. 6.4 - Experimental angular distribution (dots) of the fluorescence intensity collected by the CCD sensor upon excitation of the Cy7-VG20 molecules by the external laser at λEXC. The angular range is the same used for the label-free operation. The theoretical curve (solid purple curve) was calculated according to the procedure described in the text. Both TE- (red) and TM- (blue) polarized spectra are also plotted. (Top inset) Chemical structure of the Cy7-VG20 dye. (Bottom inset) Angular emission spectra calculated for three different absorption levels of Cy7-VG20 (the axes are the same as the main figure).

The matching with the experimental spectrum is rather good, the only fitting parameter being the total emitted energy (the spectra are in arbitrary units). The broadening of the experimental peaks is probably due to the broadening of the Cy7- VG20 emission spectrum upon interaction with the 1DPC surface [30]. We also observe a shift of the TE emission peak toward smaller angles. This is most probably due to reabsorption by the dye molecules themselves of the radiation coupled to the BSW and propagating along the 1DPC surface before being outcoupled in the TOPAS substrate. We estimate that, for the present 1DPC design, the leakage length of the TE BSW is in the range of 0.3 mm [56]. In order to give a first qualitative description of the effect, in the inset of Fig. 6.4 we show the angular emission spectra calculated when reabsorption by the Cy7-VG20 is considered. The semi-classical approach used here [32] does not describe fluorescence emission in absorbing media. Therefore, we assumed absorption in

the top 5 nm of the last SiO_2 layer, with the spectrum measured in solution and arbitrary peak increasing values. Passing from the no reabsorption condition (NO ABS) to the case in which the peak extinction coefficient of the 5 nm layer is either $1E^{-3}$ (ABS 1×) or $1E^{-2}$ (ABS 10×), leads to increasing suppression of the TE BSW fluorescence and shift of the maximum of the angular distribution. Further experimental and theoretical investigations are being carried out to quantitatively describe such effect.

6.2 Ellipsometric label-free detection of colorectal cancer biomarkers (Angiopoietin-2) on platform S1

6.2.1 BSW biosensor

The 1DPC used in this study was fabricated by PIAD as described in Chapter 4. In Fig. 6.5a, we show a sketch of the geometry of the 1DPC. In Fig. 1b, we show the angular reflectance spectrum calculated at λ_0 in the Kretschmann-Raether configuration with a BK7 coupling prism. A sharp dip in the TE reflectance is clearly visible around $\theta = 69°$, corresponding to the excitation of a TE-polarized BSW, well above the total internal reflection (TIR) edge. A much shallower dip (less than 1 %) appears in the TM reflectance at about $\theta = 64.5°$, corresponding to a TM-polarized mode. In the inset of Fig. 6.5b, we plot both the amplitude and the phase of the complex TE field reflection coefficient; the phase clearly shows a 2π shift around the resonance that will be exploited in the polarization control scheme described below. In the same angular range, the amplitude and phase of the TM field reflection coefficient are almost constant. All numerical calculations were performed by means of a custom code based on the transfer matrix method and using a plane-wave approach [28]. In Fig. 6.5c, we show the distribution of the TE polarized BSW energy density calculated at λ_0 and in resonance conditions. The BSW is confined at the interface between the 1DPC and the external medium. The field is exponentially decaying in the external medium with a penetration length (L_{pen}) of 117 nm (a hypothetic SPP sensor operating at the same λ_0 and resonance angle would exhibit the same L_{pen}). In the present work, we deposited and used two versions of the 1DPC sketched in Fig. 6.5a. In one case (type A), the 1DPC was fully fabricated and used for the physical characterization of their operation. In the second case (type B), the 1DPC was fabricated up to the titanium topping layer.

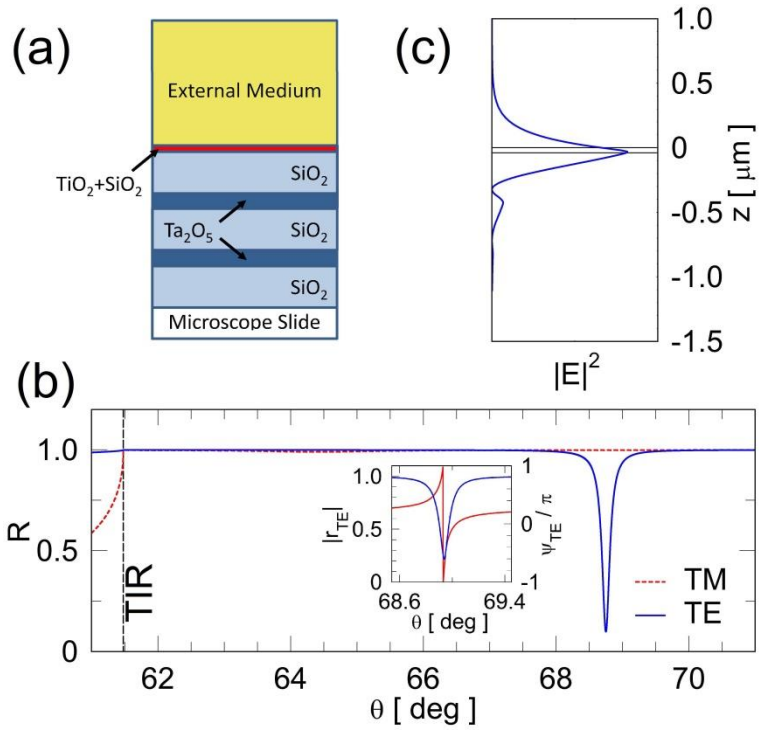

Figure 6.5 - Sketch of the 1DPC geometry. The thicknesses of the five layers of the periodic part are d_{SiO2}= 275 nm and d_{Ta2O5}= 120 nm. The thicknesses of the two topping layers are as follows type A, d_{TiO2}= 20 nm and d_{SiO2}= 20 nm; and type B, d_{TiO2}= 20 nm and d_{ppAA}=40 nm. (b) Numerically calculated TE (solid blue) andTM (dashed red) intensity reflectances for the 1DPC sketched in Fig. 1a in DI water and at λ_0 = 670 nm; TIR is the total internal reflection angle (inset). Detail of the amplitude $|r_{TE}|$ (blue) and phase Ψ_{TE} (red) of the TE field reflection coefficient calculated at λ_0. (c) Numerically calculated distribution of energy density distribution of the TE-polarized BSW at λ_0 and in resonance conditions (θ = 68.75°).

The last silica topping layer was not deposited in order to accommodate a thin functional polymer layer used to provide the chemical groups needed to graft the biomolecules. In such a way, the polymer functional layer is embedded in the 1DPC geometry and the sensing characteristics are preserved (resonance angle, sensitivity, figure of merit).

For the physical characterization of the BSW biosensors, we made use of 1DPC including the last silica topping layer (type A). In Fig. 6.7, we show the angular reflectance spectra at λ_0 for a 1DPC sensor (type A). The top parts of the figure refer to the TE case, whereas the bottom parts correspond to the cross scheme. The theoretical reflectance spectra shown in Fig. 6.7a were numerically calculated by means of a custom algorithm based on the transfer matrix method applied to stratified dielectric media and working in the plane-wave approximation. In the calculations, we did not take into account the presence of reflection losses at the two glass-air interfaces of the coupling prism. With the values assumed for the complex refractive indices

of the dielectric materials constituting the 1DPC, the theoretical TE reflectance shows a sharp and deep BSW resonance. Depending on the value of Ψ, the theoretical reflectance for the cross scheme shows either a dip or a peak and all intermediate shapes. The experimental angular reflectance curves shown in Fig. 6.7b were obtained by operating the apparatus either in the TE or in the cross scheme. The curves were extracted from images of the CMOS array detector similar to those shown in Fig. 6.6, by averaging over 100 rows (the region between the two red lines shown in Fig. 6.6) for different values of Ψ. The experimental curve for the TE polarization shows a resonance in the correct angular range and characterized by the expected full width at half maximum.

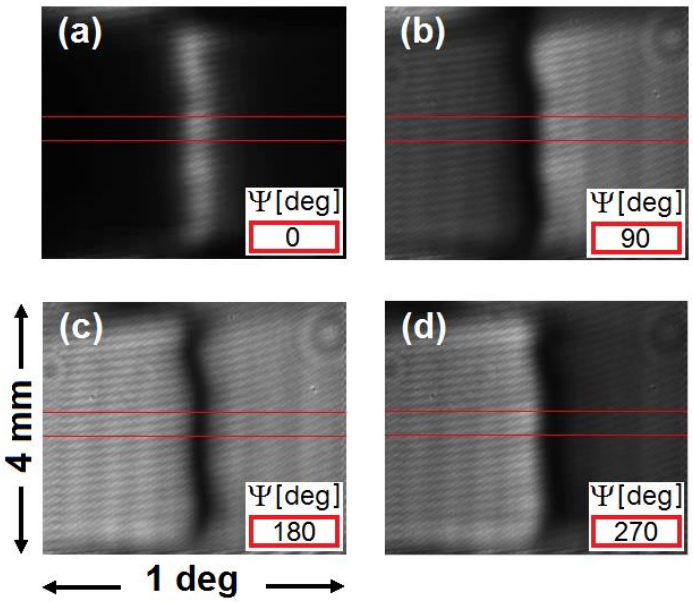

Figure 6.6 - Images captured using the CMOS array detector, for the type A 1DPC, for four different values of the phase (Ψ) introduced by the liquid crystal retarder: (a) Ψ = 0°, (b) Ψ = 90°, (c) Ψ = 180°, (d) Ψ = 270°. The images were acquired by the CMOS at θ = 69°, with an exposition time (t_{int}) of 80.1 ms, i.e. at a sampling frequency (f_{samp}) of 12.5 Hz. The tiny oblique interference fringes are due to multiple reflections in the output polarizer (not AR coated). The objective field of view is shown in (c) for convenience.

However, the resonance is much shallower (about one fourth) than that found from the theory, indicating that the absorption introduced by the thin titanium topping layer is smaller than expected. Such result confirms the difficulty to tune the depth of the BSW resonance dip by controlling the 1DPC losses upon deposition. The experimental curves for the cross case were compared very well to the theoretical curves too. In this case, the smaller absorption enhances the features around the BSW resonance with respect to the theoretical prediction. By varying the phase Ψ in the [0°, 360°] interval, we can experimentally access to all the reflectance

distributions allowed by that 1DPC structure, as shown in the video that can be accessed by clicking on the caption of Fig. 6.6.

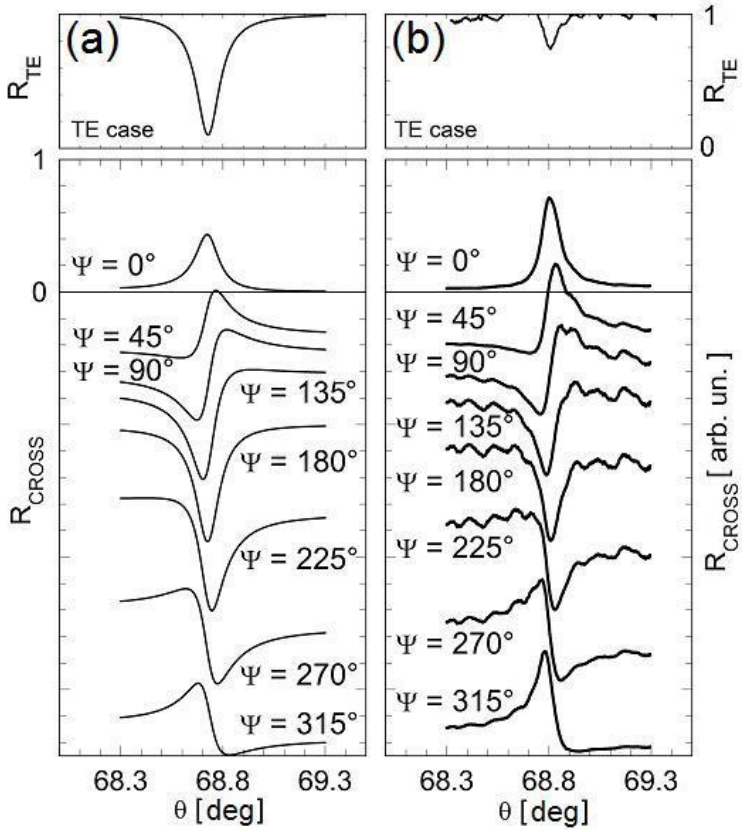

Figure – 6.7 (a) Calculated normalized reflectance spectra for the 1DPC (type A) described in the text for several different phases (Ψ) imposed by the liquid crystal retarder between the TE and TM components of the illumination beam. The Fresnel losses at the coupling prism facets are not taken into account. (b) Normalized experimental angular reflectance for the real 1DPC (type A) for different phases (Ψ). In both cases (a) and (b), the curves are shifted vertically for the sake of clarity.

Therefore, by making use of the same 1DPC sensor, one can select the appropriate phase conditions depending on the different experimental needs. For example, if one wishes to monitor a steep change in the reflectance profile, in amplitude mode at fixed λ_0 and θ_0 [58], he could set the phase around Ψ=90° and monitor the changes of the reflected intensity [29]. In the following, we report experimental results obtained in the cross scheme by setting Ψ=180° and measuring the angular shift of the minimum of the resonance dip as a function of the properties of the analytes injected in the PDMS fluidic cell. The advantage of using the cross with respect to the TE scheme can be better evidenced by defining a FoM and comparing its value in the two cases. We adopt here the same FoM we previously used [29, 17], defined as FoM = $S_V \times D/W$, where S_V is the sensitivity of the BSW resonance angle to changes of the bulk

refractive index of the external medium, D is the depth of the resonance dip (varying between 0 and 1), and W is the resonance full width at half maximum. In Fig. 6.8a, we show the angular reflectance measured for the 1DPC sensor (type A) in both the cross and TE schemes. From the Lorentzian fit of the experimental curves, we find that D_{TE}=0.28, W_{TE}=0.07°, D_{cross}=0.81, and W_{cross}=0.088°. We find that W does not change much in the two cases, while D has a strong improvement in the cross case. We expect therefore that the cross resonance can be tracked more accurately (less noise). The sensitivity (S_V) of the 1DPC sensor (type A) was determined, in both detection schemes, by injecting in the fluidic cell solutions of glucose in DI-water at several different known concentrations (0.05, 0.5 and 5 wt%). In Fig. 6.8b, we show the time dependence of the resonance position measured in the cross scheme, when either DI-water or the glucose solutions are injected in the fluidic cell. From the measurement, we derived the linear dependency of the resonance angle on the refractive index of the solutions as previously done in a precedent work [34].

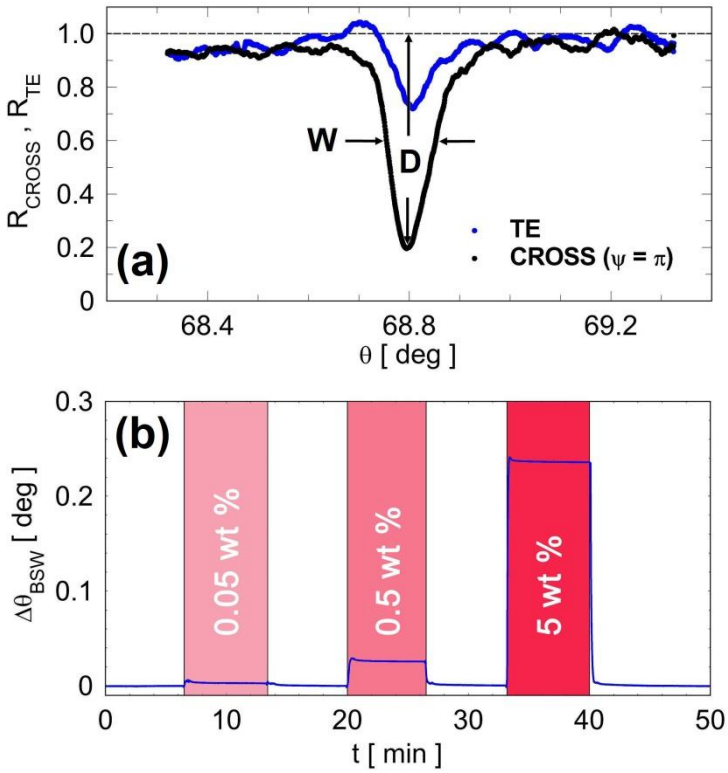

Figure 6.8 - (a) Experimental reflectance spectra in both TE (blue curve) and cross (black curve) schemes. D is the resonance depth, and W is the full width at half maximum. (b) Evaluation of the volume sensitivity obtained by injecting in the fluidic cell three different concentrations of glucose in DI-water (on the right side).

From the slope of the linear behavior, we find the same volume sensitivity for the two detection schemes, as expected also from our numerical calculations, S_V = 31.8°/remote interface units (RIU). From the values measured for S_V, D and W, we can evaluate the FoM for the two schemes. We find FoM_{TE} = 126 RIU^{-1} and FoM_{cross}= 293 RIU^{-1}, indicating that the cross scheme outperforms the TE by more than a factor of 2. Considering that the LoD is inversely proportional to the FoM [31], we expect the LoD to be improved. We determined the LoD in the cross scheme by measuring the noise of the measurement of the angular position of the resonance in static conditions and at fixed temperature (±0.01 °C). We find $\sigma(\theta_{BSW})=7.31°\times10^{-5}°$, when fitting the resonance in a ±0.015° range (±20 pixels) around the minimum with a quadratic model and running the CMOS detector at a sampling frequency (f_{samp}) of 12.5 Hz. Such value corresponds to a 1 Hz equivalent bandwidth noise with σ_{1Hz} $(\theta_{BSW})=2.07°\times10-5°/Hz1/2$. We can therefore say that the $LoD=\sigma 1$ Hz $(\theta_{BSW})/S_V= 6.5\times 10^{-7}$ $RIU/Hz^{1/2}$. Such value is smaller than that found experimentally for the TE case, $LoD_{TE}= 2.6\times10^{-6}$ $RIU/Hz^{1/2}$, and can be further improved by optimizing the 1DPC sensor structure [34] and by detection of features (array detector with lower noise (CCD) and larger number of pixels, larger fitting interval, better fitting algorithms).

6.2.2 Bio-conjugation protocol

In this case, the 1DPC sensor surface is chemically activated with EDC/sulfo-NHS, and differently from the case described in the Chapter 4, the PtG immobilization is carried out externally, before mounting it on the optical setup. This permits to perform PtG immobilization only on some selected regions of the 1DPC sensor surface. For the assay described here, the 1DPC sensor surface which is accessed by the optical measurement was divided in two regions, in order to define one signal and one reference spots. In the two regions, we incubated simultaneously PtG (signal spot) and BSA (reference spot) in a moisturized atmosphere for 1 h at ambient temperature. The concentrations of the solutions used for immobilization of either PtG or BSA were 0.5 and 10 mg/mL, respectively. The concentration of the PtG solution was determined according to the experience gained in the measurements reported in the previous section. After incubation, the 1DPC sensors were washed thoroughly with D-PBS 1X and the incubation of BSA was repeated under the same conditions all over the 1DPC sensor surface in order to saturate all the ppAA functional groups. At the end, the resulting biochips were washed again thoroughly with DPBS 1X.

6.2.3 Results and Discussions

After preparation, the biochip was topped with a one channel microfluidic cell which permits to flow the analytes on top of the signal and reference spots, as sketched in Fig. 6.9a. The biochip was then mounted in the optical setup and operated in the cross scheme at Ψ=180°. The contact surface and volume of the fluidic channel are 18.7 mm^2 and 12 µL, respectively. In Fig. 6.9b, we show the CMOS camera image obtained when operating the biochip in D-PBS 1X. In the two regions where PtG and BSA were immobilized, a BSW resonance dip is observed; the resonance is missing in the intermediate region where the hydrophobic mark used to define the two regions is situated. In all the tests, a given volume (V, µL) of the analyte solution was injected in the channel at a flow rate (F, µL/s) from the reference spot side by means of a motorized syringe pump.

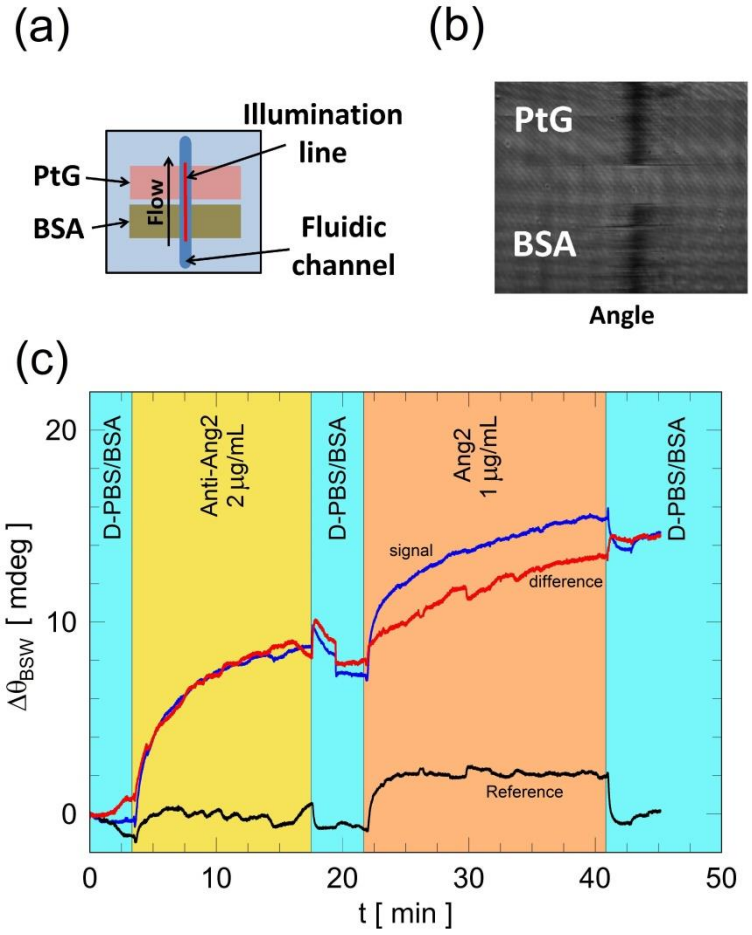

Figure 6.9 - (a) Sketch of the alignment of the fluidic channel, the sharp illumination line and the two spots used for signal and reference measurements for the biochips used in the cancer biomarker detection assays. (b) CMOS camera image obtained when the reference and signal spots are illuminated simultaneously. The image was obtained in D-PBS 1X environment before performing the assay. (c) Time dependence of the BSW resonance angular position in the cross reflectance obtained for Ψ=180°

in a cancer biomarker assay with anti-Ang2 and Ang2. The black curve is the reference, the blue curve is the signal, and the red curve is the difference of the two. $\Delta\theta_{BSW}$ is the relative angular shift of the BSW resonance.

In Fig. 6.9c, we show an exemplary assay performed with a biochip prepared as described above. Before starting the assay, the fluidic cell is filled with D-PBS 1X. Then, a 20 mM solution of glycine in water and HCl (pH 2.5) is injected in the cell to remove the proteins that are not covalently bound to the biochip surface. After 5 min, the solution is removed by injecting the buffer used during the assay, D-PBS 1X with 0.1 wt% BSA, and the assay is started (t = 0). The angular position of the BSW resonance in the signal (blue) and reference (black) spots is tracked as a function of time upon injection of the analytes. The difference between the reference and the signal is also plotted (red) in Fig. 6.9c. At t = 3.3 min, a solution of anti-Ang2 in the buffer, with a concentration of 2 μg/mL, was injected, and at t = 17.5 min, it was removed by injecting the buffer again. At t = 21.7 min, a solution of Ang2 in the buffer, with a concentration of 1 μg/ mL, was injected, and at t = 40.8 min, it was removed by injecting the buffer again. The injections of the anti-Ang2 and Ang2 solutions were performed with V=100 μL and F= 1.13 μL/s. All over the incubation time, a recirculation procedure was applied by pumping back and forth 25 μL from the syringe pump at F=0.5 μL/s. The injections of the buffer were performed with V=500 μL and F=2.95 μL/s. While washing with the buffer, the signal and the reference were measured along a time interval larger than the injection time; therefore, the step in the signals is due to stopping the flow and the last part of the measurement in the buffer is in static conditions. During the assay, the reference shows a slight response due to transient temperature/pressure effects and to the different refractive indices of the solutions. On the other hand, upon injection of both analytes, the signal shows an exponential growth, indicating that the binding of anti-Ang2 to PtG and of Ang2 to anti-Ang2 is taking place during incubation. Fluctuations observed in both spots are due to pressure effects induced by the recirculation procedure. Clearly, the differential signal, due only to binding of anti- Ang2 to PtG and of Ang2 to anti-Ang2, shows residual shifts after buffer washing whose values are reported in Table VI.I.

Protein	MW (kDa)	C^a (μg/mL)	$C_M{}^b$ (μM)	$\Delta\theta^c$ (mdeg)	Γ^d (ng/cm^2)	Σ^e (10^{12}/cm^2)	h^f (nm)
G	21.6	1000	46.3	62	120	3.4	2.5
Anti-Ang2	150	2	0.013	7.1	13.7	0.055	0.29
Ang2	50	1	0.020	5.4	10.5	0.126	0.22

MW the molecular weight

[a] The mass of the solutions in D-PBS 1×

[b] The molar concentrations of the solutions in D-PBS 1×

[c] The residual angular shift of the BSW resonance after PBS and glycine-HCl washing

[d] The mass surface coverage

[e] The surface density

[f] The adsorbed layer thickness calculated assuming as a refractive index for all the biological layers (PtG, anti-Ang2, Ang2); n_{BIO}=1.42

Table VI.I - Summary of the protein properties and results extracted from the sensogram.

From such shifts, by making use of Eq. (6.1), we evaluated the Γ, Σ and h for the anti-Ang2 and Ang2 add layers, as reported in Table VI.I. The results show that the BSW biochip, prepared as reported above, can efficiently detect Ang2 in a buffer solution at the 1 μg/mL concentration. We can infer information on the limit of Ang2 detection by considering the measurement noise. The standard deviation of the noise observed during the assay is $\sigma(\theta_{BSW})=1°\times10^{-4}°$ when operating the CMOS at f_{samp}= 12.5 Hz, calculated from the difference signal measured in the time interval t∈[41, 45 min] at the end of the assay in static conditions. Such value is slightly larger than that reported above for the type A sensor, in which only physical components contribute to the noise. From Eq. (6.1), assuming that the minimum detectable resonance shift is $\sigma(\theta_{BSW})$, one can calculate the limit of the biochip for Ang2 detection as Γ_{LoD}= 1.9 pg/mm^2 at f_{samp}=12.5Hz. Such Γ_{LoD} must be compared to the present state of the art for label-free techniques that is around 1–2 pg/mm^2 [29,60]. The Γ_{LoD} found here can be decreased by decreasing the detection noise and by improving the referencing configuration. As an example, if $\sigma(\theta_{BSW})$ would get to the value we found for this sensor, we would have Γ_{LoD}=1.4 pg/mm^2. Changing the CMOS integration time could lead to further improvement.

6.3 Label-free detection of colorectal cancer biomarkers (Angiopoietin-2) on platform S1

6.3.1 Bio-conjugation protocol

For this specific application, optimized 1DPCs (design A|13|634) are functionalized by means Strategy A (described in Chapter 5). The glutaraldehyde-activated surface of the biochip is then divided into two regions, reference and signal sides, by means of a hydrophobic marker.

The signal and reference regions were incubated with Protein G (PtG, 0.5 mg/ml, Thermo Scientific) in sodium bicarbonate buffer or Bovine Serum Albumin (BSA, 10 mg/ml, Sigma-Aldrich) in D-PBS 1X, respectively, for 1 h at room temperature (RT). Subsequently, the chip was immersed in a solution of BSA (10 mg/ml) in D-PBS 1X to block the remaining reactive sites (overnight at +4 °C). At the end of such incubation steps, on the biochip surface there are a signal region (PtG), which is capable to bind and orient the capture antibodies, and a reference region (BSA), which is biochemically inert. Immediately before their use in a detection assay, the surface of the biochips was treated with a regeneration solution made of glycine (20 mM, Sigma-Aldrich) in DI water and HCl with a pH of 2.5 for 10 min at RT. This procedure removes any adlayers formed on both the signal (PtG) and reference (BSA) regions upon BSA blocking step.

6.3.2 Results and Discussions

Biochips prepared according to the procedures reported above were used to carry out Angiopoietin 2 (Ang-2) detection assays by means of the optical apparatus S1 described in Chapter 3. In the assays we used Ang 2 (Recombinant Human Angiopoietin 2, P.N.623-AN from R&D Systems) spiked in a D-PBS 1X + 0.1 wt% BSA buffer. Under these non-reducing conditions the Ang 2 molecules are mostly (90 %) in a dimer form, with a small presence of trimers (9 %) [61]. At the beginning of the assay the buffer is injected in the fluidic channel and the BSW resonances (see Fig. 6.10) are tracked until a stable baseline is obtained. In Fig. 6.11 we show the time traces of a sensorgram recorded during one exemplary Ang 2 detection assay. The curves are related to the BSA reference (blue) and PtG signal (red) regions, together with the difference signal (black). The angular position of the BSW resonance is extracted from the CMOS array images in both the signal and reference regions, at the sampling rate f_{samp} = 12.5 Hz. BSW resonance curves similar to those shown in Fig. 6.10 are obtained by averaging 64 lines of the CMOS image in each region, corresponding to 0.25 mm wide measurement spots. In each spot the angular position of the BSW resonances minima were found by fitting with a parabola the data in a range that is adapted to the resonance width, here ±50 pix. Both BSA and PtG traces shown in Fig. 6.11 are the average of the traces measured in five different spots of the respective region.

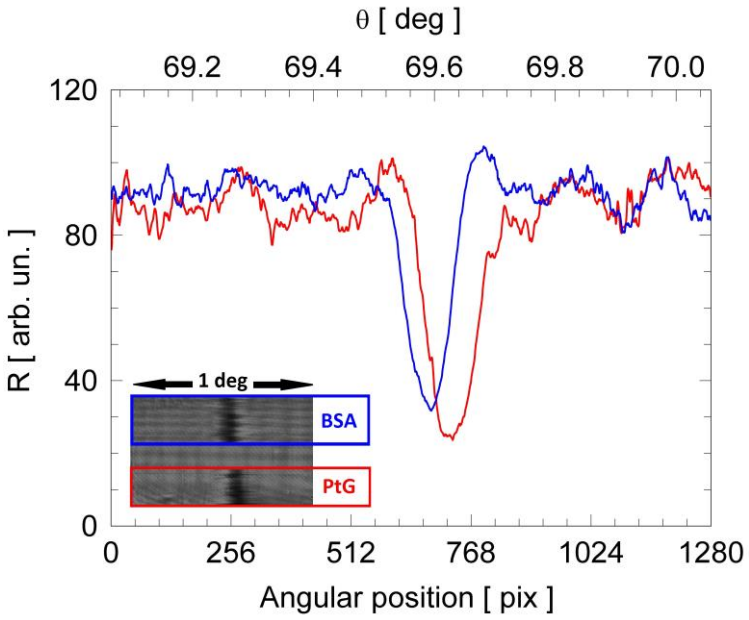

Figure – 6.10 Angular reflectance spectra for both signal (PtG, red line) and reference (BSA, blue line) regions. The spectra were obtained averaging 320 lines of the CMOS array image. In the inset the CMOS image of both PtG and BSA regions.

To specifically detect the presence of Ang 2, a monoclonal anti-human Ang 2 capture antibody is used in the present work (Anti-Ang 2, Monoclonal anti-human Angiopoietin 2, Antibody, P.N.MAB0983 from R&D Systems). The Anti-Ang 2 capture antibody is diluted in the buffer at the concentration of 2 μg/ml. At the beginning of the assay (t = 3 min) a volume of 100 μl of the Anti-Ang 2 solution is directly injected in the fluidic channel at a rate of 4 μl/s by means of the motorized syringe pump and incubated for 16 min. During the incubation a recirculation procedure is applied, in which a 27 μl volume of the Anti-Ang 2 solution is pushed back and forth through the channel at a rate 1 μl/s. The recirculation gives rise to the oscillations observed in the curves due to pressure induced changes of the analyte refractive index.

A clear binding curve is observed in the PtG signal region, whereas the BSA reference region shows a linear slope with steep changes, as a function of sample injections. While the slope is due to a slow temperature drift, the steep changes should be the result of refractive index changes upon different analytes injection, and transient temperature and pressure effects. By subtracting the signal and reference curves one can rule out such parasitic drifts and recover the information related to the specifically binding of Anti-Ang 2 only.

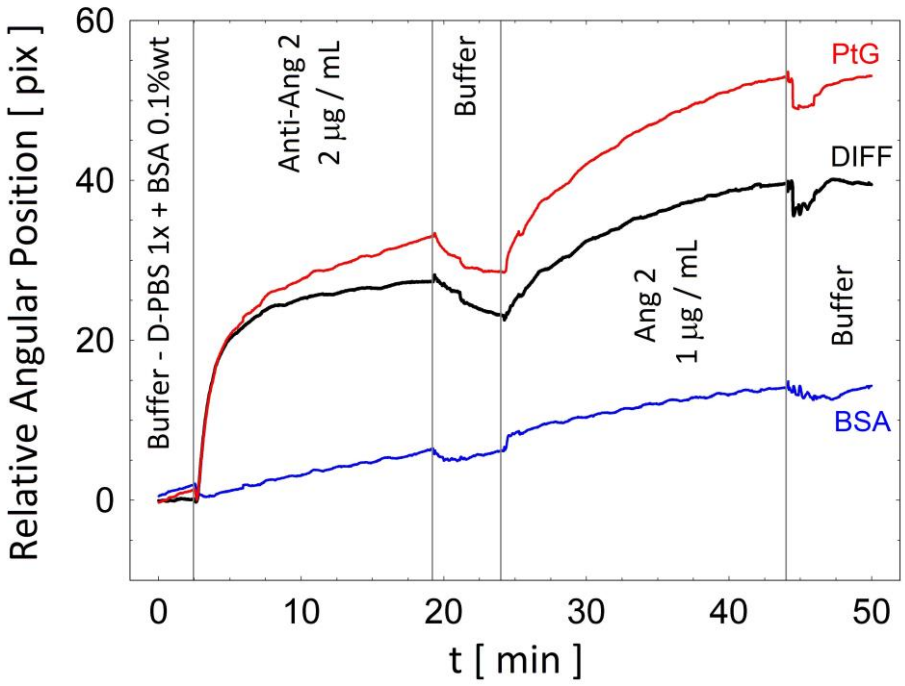

Figure – 6.11 Sensorgrams recorded during the label-free Ang 2 detection assay in the PtG (red) and BSA (blue) regions. The black solid curve is the difference signal from which we extracted the relevant quantities reported in Table VI.II.

Fig. 6.11 demonstrates that the PtG layer in the signal region binds efficiently with the Anti-Ang 2 capture antibodies providing a proper orientation on the 1DPC surface, maximizing the detection of the antigens. On the other hand, the BSA layer in the reference region effectively blocks non-specific adsorption on the 1DPC surface.

At the end of the Anti-Ang 2 incubation a 500 µl volume of buffer is injected in the channel at 4 µl/s for washing. Dissociation of Anti-Ang 2 is observed as expected, due to the removal of excess non-specifically bound Anti-Ang 2. The total residual angular shift $\Delta\theta$ at the end of the washing step, that reflects Anti-Ang 2 binding to PtG, is reported in Table VI.II. Under the conditions reached at the end of the precedent steps the biochip is ready for the detection of the Ang 2 cancer biomarker. Upon injection of a 2 µg/ml Ang 2 solution in the buffer (t = 24 min, injected volume 100 µl at 4 µl/s, incubation for 20 min with recirculation of 27 µl at 1 µl/s) again a clear binding curve is observed in the signal region with respect to the reference region. The difference-signal shows a well-defined exponential growth, indicating that indeed Anti-Ang 2 efficiently detects the Ang 2 antigens present in the test solution. At the end of the incubation the biochip is washed with 500 µl buffer injected at 4 µl/s. The total residual angular shift $\Delta\theta$, due to the specific binding of Ang 2 to Anti-Ang 2, at the end of the washing step is reported in Table VI.II.

From the angular shifts Δθ reported in Table VI.II we can evaluate the mass surface coverage Γ for Anti-Ang 2 and Ang 2 making use of the following formula [62] derived from the De Feijter formula [63]:

$$\Gamma = \frac{\Delta\theta \cdot L_{pen}}{S_V \cdot \partial n/\partial C} \tag{6.1}$$

where $\partial n/\partial C$ is the refractive index increment of the molecules and $\partial n/\partial C$ = 0.19 cm^3/g for most of proteins [63]. From Γ, we calculate the surface density Σ = Γ/MW, where MW is the molecular weight. The analysis of the sensorgram confirms that the 1DPC biochips can efficiently detect the presence of Ang 2 in a buffer solution.

TABLE VI.I
DATA ON THE PROTEIN LAYERS IN THE LABEL-FREE ASSAY

Protein	M_W [kDa]	C [μg/mL]	Δθ [mdeg]	Γ [ng/cm²]	Σ [10^{12}/cm²]
Anti-Ang 2	150	2	18.6	35.1	0.14
Ang 2 (dimer)	140	1	12.4	23.4	0.10

Table VI.II – Data on protein coverage density for Ang 2 experiments.

The experimental value of Σ for Ang 2 is smaller than that found for Anti-Ang 2, as expected for Langmuir isotherm equilibrium far from saturation conditions [64]. Analyzing the noise of the difference signal we find σ_{NOISE} = 0.1 pix = 7.75E-5 deg. From the Eq.(6.1), assuming that the minimum detectable resonance shift is σ_{NOISE}, one can calculate the limit of the 1DPC biochip for Ang 2 detection as Γ_{LoD} = 1.5 pg/mm^2 at f_{SAMP} = 12.5 Hz.

In order to confirm effective recognition of Ang 2 biomarkers by Anti-Ang 2 antibodies in the PtG signal region, we performed the assays by introducing fluorescent labels, similar to the standard enzyme linked fluorescence assays (ELFA). This part of the assay is carried out without monitoring the label-free signal.

A specific biotinylated-detection Anti-Ang 2 antibody (Anti-Ang 2*, Polyclonal Human Angiopoietin 2 Biotinylated Antibody, P.N. BAF623 from R&D Systems) was used to detect the presence of Ang 2 at the biochip surface. A 100 μl volume of a solution of Anti-Ang 2* in the buffer at a concentration of 2 μg/ml was injected in the fluidic channel at the rate of 4 μl/s, incubated for 16 min adopting the same recirculation procedure shown above and washed with the buffer.

Then, a solution of neutravidin labelled with fluorophores emitting at λ_{MAX} = 670 nm (NeutrAvidin650, DyLight 650 conjugated from ThermoScientific) was injected in the channel. Neutravidin with very high affinity for biotin should enable detection of the Anti-Ang 2* antibody. A 100 µl volume of a solution of NeutrAvidin650 in D-PBS 1x at a concentration of 10 µg/ml was injected in the fluidic channel at the rate of 4 µl/s, incubated for 16 min adopting the same recirculation procedure as above and washed with D-PBS 1X.

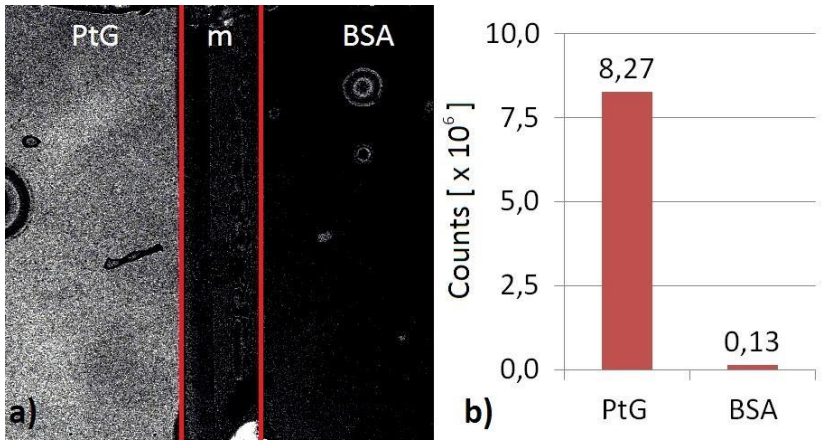

Figure – 6.12 (a) Confocal fluorescence microscopy image of the dry 1DPC biochip at the end of the complete Angiopoietin 2 detection assay. (b) Average intensities in the PtG and BSA regions, confirming that efficient detection of Ang 2 was achieved.

At that time the fluorescence detection arm was not yet working (development stage) and thus we decided to perform the fluorescence analysis ex-situ by means a confocal microscope. Thus, at the end of this process, the biochip fluidic channel was emptied, dried and the biochip unmounted from the optical apparatus. It was immediately transferred to the confocal microscope to investigate the fluorescence emission in the two regions. The confocal fluorescence detection was performed exciting the dried biochips from the 1DPC side. In Fig. 6.12(a) we show the confocal fluorescence image obtained when exciting at λ_{EXC} = 635 nm and detecting in the $\lambda_{EM} \in$ [655 nm, 755 nm] window. The average intensities measured in the two regions are shown in Fig. 6.12(b). The strong fluorescence contrast confirms the efficient detection of Ang 2 in the PtG region.

6.4 Label-free and Fluorescence detection of colorectal cancer biomarkers (Angiopoietin-2) on platform S3

6.4.1 Bio-conjugation protocol

For these experiments, 1DPCs (A|13|634) are functionalized by means Strategy A (described in Chapter 5). The reactive glutaraldehyde surface of the biochip is divided into two regions, reference and signal sides, by means of a hydrophobic marker.

Protein immobilization starts with the coupling of PtG (0.5 mg/ml) in sodium bicarbonate buffer. As previously described, the PtG solution is brought in contact with one part of the sensing area that will be referred to as signal spot. A second part of the sensor surface is incubated with 10 mg/mL of BSA to serve as the reference. Protein coupling was stopped after 1 h interaction time at RT by washing away residual solution. Finally, the full surface was immersed in 10 mg/ml of BSA overnight at +4°C in order to block remaining reactive sites. In result, capture antibodies can be coupled later on with Fc fragment to the PtG (signal spot) surface in order to maintain their functional Fab sites for specific detection. Immediately before use the surface of the biochips was treated with a regeneration solution made of 20 mM glycine and HCl with a pH of 2.5 for 10 min at RT. This step improves the recovery of surface reactivity after the blocking step in BSA, because any adlayers should be removed from the covalently linked protein layers.

6.4.2 Results and Discussions

For the label-free assay we can make reference to the middle part of the sketch shown in Fig. 6.13. The assay starts at t = 0 with the injection of 100 μl of the capture antibody (a-Ang2) with a volume flow rate of 1.35 μl/s. The injection is performed from the inlet at the BSA protein region, which corresponds to the spot number 0-9 of the used system configuration.

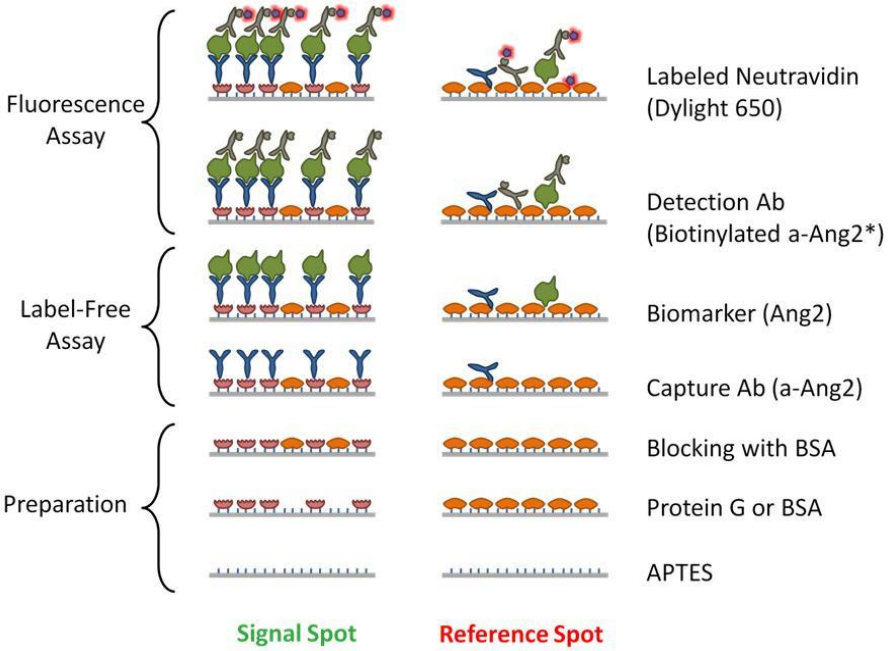

Figure 6.13 – Sketch of the cancer biomarker detection assay for Angiopoietin 2 (Ang2).

After a recirculation of 50 μl (10 times back and forth at 1.35 μl/s) of the a-Ang2 for about 13 min, the microfluidic channel was washed with 500 μl of the buffer. At t = 20 min the Ang2 biomarker was injected and recirculated in the channel (the parameters are the same as above for the a-Ang2). The step is followed by the same washing procedure in the buffer solution.

For what is concerning the label-free mode of operation, in Fig. 6.14 we show the sensorgrams measured in several different spots, inside the signal (PtG) and reference (BSA) regions. Clearly the sensorgrams are grouped in two different families, demonstrating that the PtG region and the BSA region are responding in a different way when the analytes are injected. A drift of the signal is observed in both regions. In this way, the measurements carried out in the BSA region can be used as a reference to rule out all parasitic effects affecting the measurement obtained in the signal region.

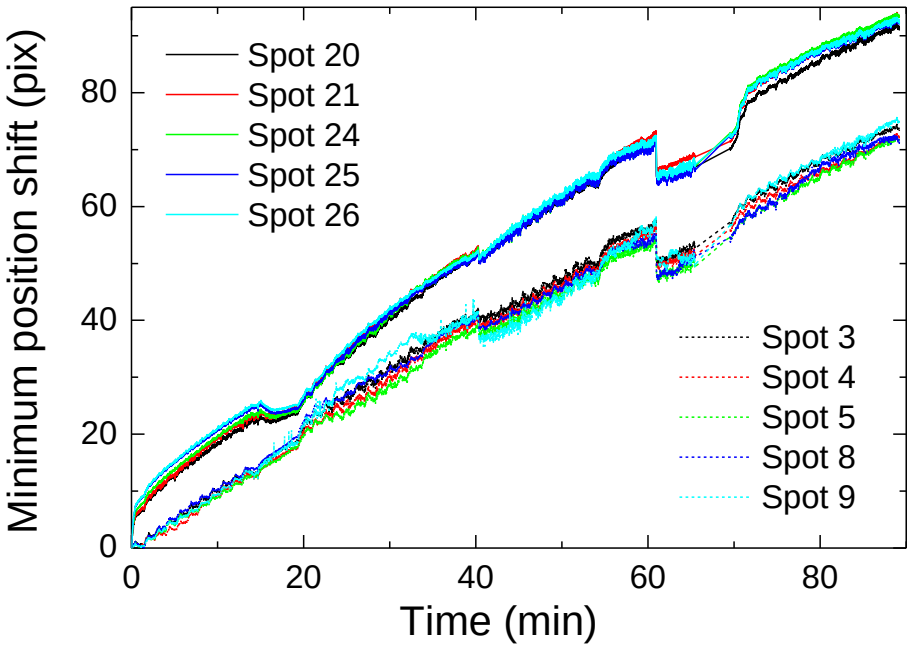

Figure 6.14 – Sensorgrams measured in several different spots in the PtG (spot 20, 21, 24, 25, and 26) and BSA (3, 4, 5, 8, and 9) regions. The sensorgrams were selected out of all those recorded by eliminating those that were corrupted by large noise (bubbles, defects on the surface, ...).

The curves shown in Fig. 6.14 were averaged in the two signal and reference regions, giving rise to averaged signal and a reference curve. Then subtraction of such curves was performed ruling out all parasitic effects (drift of the resonances due to temperature, pressure, refractive index fluctuations, illuminating wavelength fluctuation, and water adsorption inside the 1DPC). In Fig. 6.15 we show the sensorgram obtained after averaging and subtraction. The error bars in Fig. 6.15 are the standard error of the mean, which were obtained from a simple statistical analysis of the signals from the selected spots. It is noteworthy that an adjustment of the label-free signal to the photonic crystal sensitivity, which varies from one spot to another, does not decrease the error of the signal and changes only slightly the mean value. The sensorgram of Fig. 6.15 demonstrates the label-free detection of target biomarkers with the S2 platform. It is worth to notice that, besides providing the fluorescence emission and permitting to operate in the fluorescence mode, the second part of the assay (a-Ang2* and neutravidin) gives rise to an enhancement of the angular shift (mass loading effect) measured in the label-free operation mode.

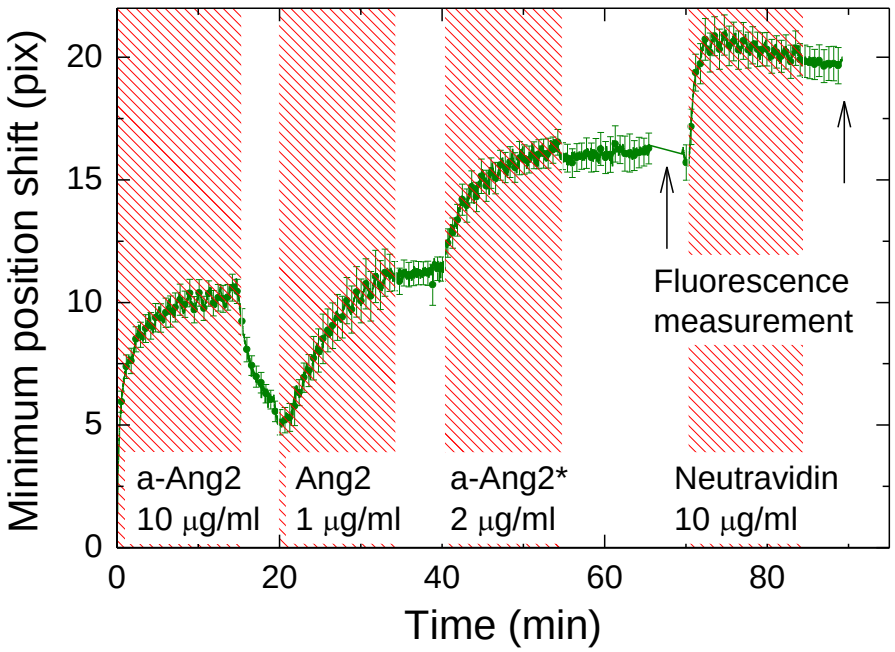

Figure 6.15 – Sensorgram of the complete assay detecting Ang2 biomarker of 1 μg/ml. The arrows mark the fluorescence measurements of the background and assay signals. The shaded areas highlight the time intervals for the injection and recirculation of a corresponding reagent. The y-axis shows the difference of the mean BSW resonance angle in 5 PtG and 5 BSA regions. The error bars are the standard error of the mean of the 5 selected measurement spots.

As shown in Fig. 6.15, the fluorescence assay starts at t = 40 min when the biotinylated detection antibody a-Ang2* is injected and recirculated in the channel (the parameters are the same as above for the a-Ang2). The step is followed by the same washing procedure in the buffer solution. Before injecting a D-PBS 1X solution of the labelled neutravidin, the cell was washed with the D-PBS 1X buffer and the fluorescence background signal was collected using 0.01 sec integration time and scanning the position of the excitation laser diode from 5 to 10 mm. At t = 70 min, the neutravidin was injected and recirculated. At the end of the assay the microfluidic channel was washed with the D-PBS 1x buffer. The fluorescence signal is then measured again using the same integration time, scanning the position of the excitation laser diode from 5 to 10 mm.

In Fig. 6.16 are shown the background subtracted fluorescence signal averaged on the same 5 selected spots in the PtG and BSA regions. The error bars are the standard error of the mean.

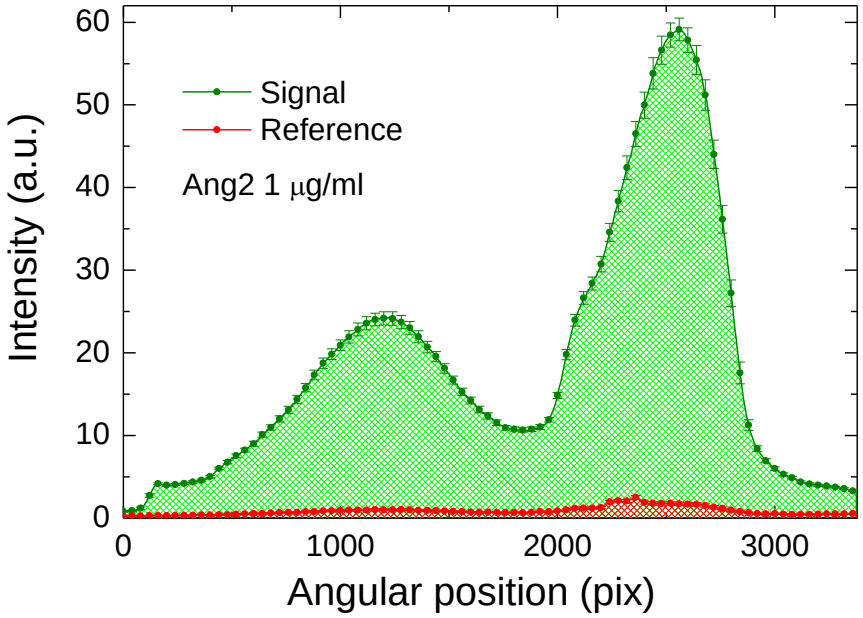

Figure 6.16 - An average fluorescence signal of the immobilized labelled antibody-antigen complex from the PtG (signal) and BSA (reference) regions at the end of the 1 μg/ml Ang2 assay. The excitation laser diode position is fixed at the maximum detected fluorescence intensity. The fluorescence background signal was subtracted from the data. The error bars are the standard error of the mean of 5 selected measurement spots.

The signal in the PtG (light green area) region is much larger than the signal in the BSA (light red area) region, performing both label-free and labelled detection of target cancer biomarkers. Same procedures are repeated for different concentrations of Ang 2 down to 10 ng/ml, varying the concentration of the capture Anti-Ang 2 with the purpose to capture more when lowering the analyte concentration. In Fig. 6.17 and 6.18 we report the differential label-free sensorgrams and the corresponding fluorescence spectra for both regions.

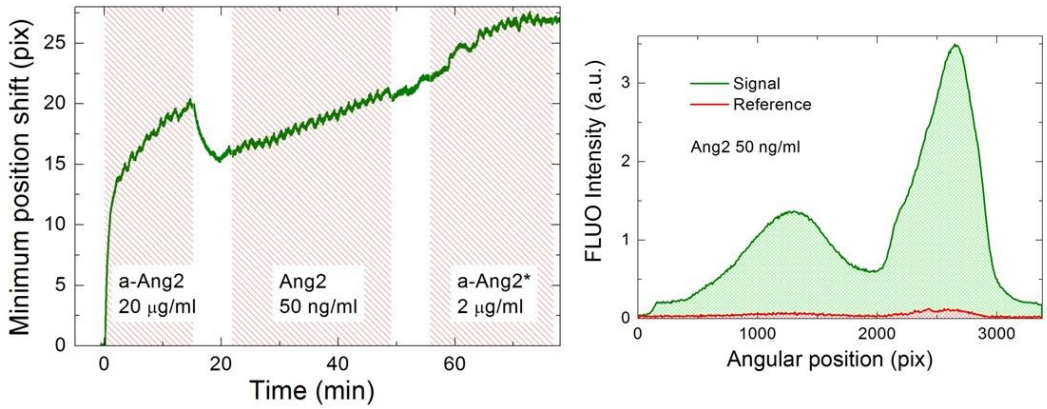

Figure 6.17 – Differential label-free sensorgrams and the background subtracted fluorescence spectra for an Ang 2 concentration of 50 ng/ml.

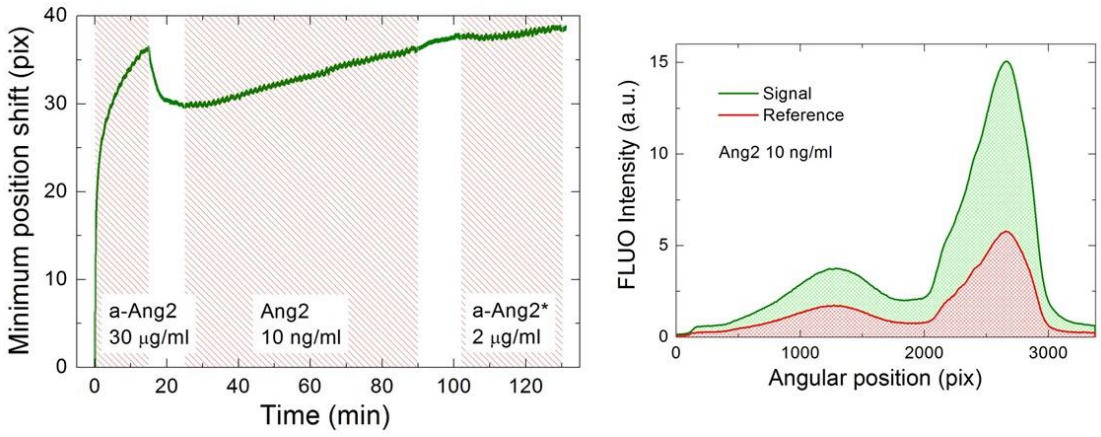

Figure 6.18 – Differential label-free sensorgrams and the background subtracted fluorescence spectra for an Ang 2 concentration of 10 ng/ml.

According to the fluorescence spectra the second antibody could be successfully detected on the PtG coated surface, while practically no fluorescence increase is obtained at the BSA-coated spots. This confirms that fluorescence operation mode can increase the resolution of the platform allowing to sense lower concentration of analytes.
From Fig.6.18, we can evaluate the fluorescence limit of detection as follows:

$$LoD_{S2}^{FLUO} = 10ng/ml \cdot \frac{Average\ Intensity\ Area\ (BSA)}{Average\ Intensity\ Area\ (Anti-Ang2)}\Big|_{10ng/ml}$$

getting a LoD = 4.4 ± 0.6 ng/ml corresponding to 0.088 ± 0.012 nM. Such result was included in the text as a limit of detection for Ang 2 of the platform S2 in the fluorescence mode.

6.5 Label-free/fluorescence detection of breast cancer biomarkers (ERBB2) in cell lysates on S1

6.5.1 Cell Biology and Biochemistry

In the present work we used two different cell lines: SK-BR-3 and Colo 38. SK-BR-3 breast cancer cells carry an amplified and overexpressed ERBB2 gene, and were used as a convenient source of ERBB2 molecules, since their absolute number per cell ($5 \div 6 * 10^5$ molecules per cell) have been concordantly estimated by at least two groups [65,66]. Colo 38 melanoma cells were selected as a negative control (see Fig.6.19) since they do not express detectable amounts of ERBB2 [67].

mAbs W6/300G9 (capture Anti-ERBB2) and W6/800E6 (detection Anti-ERBB2) to distinct epitopes of the ERBB2 ectodomain [68] were used on the biosensing platform for ERBB2 capture and detection, respectively. For fluorescence detection, mAb W6/800E6 was conjugated to the NHS ester of Alexa Fluor 647, at an approximate molar ratio of 10:1 (Anti-ERBB2 AF647).

For internal background referencing, and to subtract non-specific interactions, mAbs of irrelevant specificity were selected. mAb L-31 binds human Major Histocompatibility Complex class I (MHC I) molecules [69], and mAb 34.4.1S binds a highly restricted, polymorphic murine $E\beta^{\delta}$ epitope on MHC II molecules not expressed on any known human protein [70]. All mAbs were dissolved in Dulbecco's Phosphate Buffered Saline 1X (D-PBS 1X).

In the assays with the biosensing platform, we frequently observed that at large concentrations NP40 generates air bubbles and micelles, causing signal degradation. Therefore, we reduced NP40 concentration and determined whether this affects ERBB2 extraction efficiency. With this aim, Western blotting was carried out by SDS-PAGE slabs of SK-BR-3 and Colo 38 NP40 total cellular lysates (10 μg/lane), electroblotting, and filter incubation with selected mAbs: mAb 3D5 to the c-terminus of ERBB2 (ThermoFisher) at 1.0 μg/mL, and a rabbit polyclonal to Heat Shock Protein Hsp90 (StressGen), to equalize input. The signal was developed by chemiluminescence. ERBB2 in SK-BR-3 lysates was recovered in a nearly quantitative way in a range of NP40 concentrations as low as 0.1%. For the assays reported in the present study, 0.5% NP40 concentrations were selected.

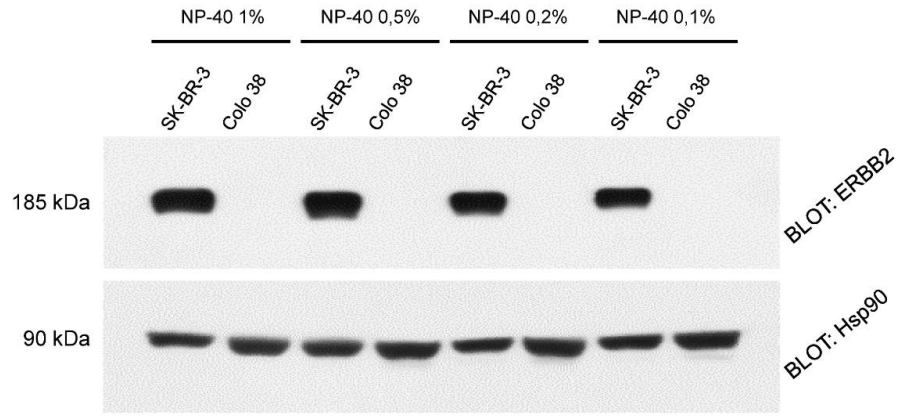

Figure 6.19 - Western Blot of SK-BR-3 and Colo 38 (ERBB2-negative) lysates. A heat shock protein of 90 kDa was used as a control.

SK-BR-3 and Colo 38 lysates were diluted in lysis buffer at 1:16, 1:40, 1:160 and 1:800 dilutions, giving rise to four ERBB2 positive (from P1 to P4) and four ERBB2 negative

samples (from N1 to N4). From a simple conversion one can get the ERBB2 concentration C_{ERBB2} for each sample solution. In Table VI.III, we list the resulting C_{WH} , C_{ERBB2} and m_{LYS} (mass of the raw lysates) values for all dilutions.

SAMPLE	Cell line	Dilution	C_{WH} [μg/mL]	C_{ERBB2} [ng/mL]	m_{LYS} [μg]
P1	SK-BR-3	1:16	500	175	60
P2		1:40	200	70	24
P3		1:160	50	17.5	6
P4		1:800	10	3.5	1.2
N1	Colo 38	1:16	500	-	60
N2		1:40	200	-	24
N3		1:160	50	-	6
N4		1:800	10	-	1.2

Table VI.III – Lysate samples used in the assays carried out with the optical biosensing platform.

For the assays carried out with ERBB2 spiked in D-PBS1X we made use of a recombinant ERBB2 Fc fusion chimera (ERBB2-Fc), which contains the entire extracellular domain of ERBB2 fused to the Fc portion of human immunoglobulin (R&D Systems).

6.5.2 Bio-conjugation protocol

The 1DPC (A|13|634) is used in this experimental session. The glutaraldehyde-activated surface of the biochip is divided into signal and reference spots, by means of a hydrophobic marker. In the signal spot we incubated the capture Anti-ERBB2 and in the reference spots the non-specific mAbs (Anti-MHC I and/or Anti-MHC II). In all cases we dissolved the mAbs in D-PBS 1X at 0.5 mg/ml and incubated for 1 hour at RT. After a further washing step, the chips were immersed in a solution of BSA (10 mg/ml) in D-PBS 1X to block the remaining reactive sites (overnight at +4 °C). At the end the biochip was washed in D-PBS 1X.

6.5.3 Results and Discussions

6.5.3.1 Recombinant ERBB2-Fc spiked in D-PBS 1X buffer

We prepared test solutions by spiking chimera ERBB2-Fc in D-PBS 1X at a concentration of 20 ng / mL. In this case, on the BSW biochip's surface we defined only two sensing spots where either capture Anti-ERBB2 (signal) or Anti-MHC II (reference) were bio-conjugated. In the assay, at the beginning the fluidic channel is filled with D-PBS 1X. The LF laser is illuminating the biochip and the FLUO laser is blocked with a shutter (LF mode).

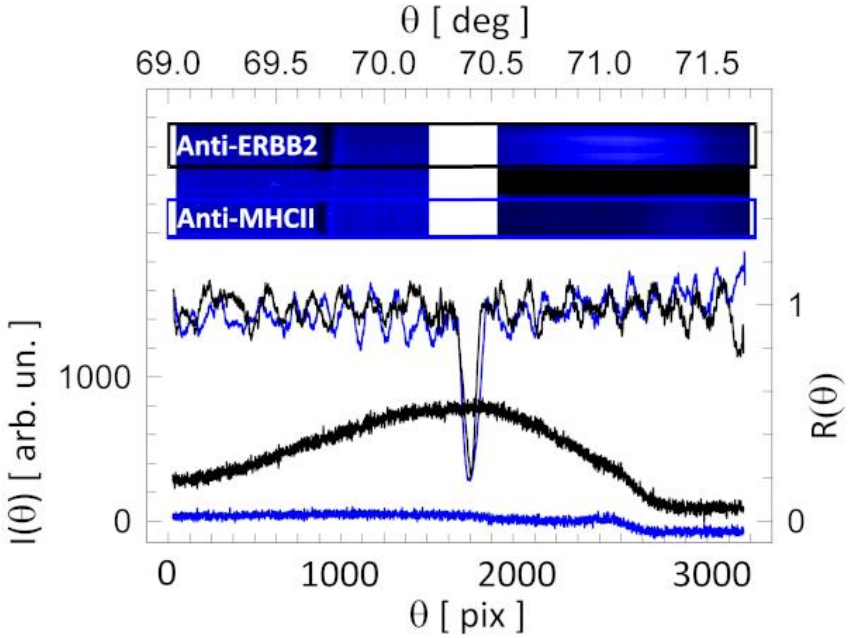

Figure 6.20 - Experimental curves recorded by the CCD camera during the assay with ERBB2 spiked in D-PBS 1X. The curves refer to either LF (top curves) or FLUO (bottom curves) operation for the signal (black) and reference (blue) sensing spots. R(θ) (right axis) shows the BSW resonance in the LF mode. I(θ) shows DyLight 650 fluorescence emission. (Insets) CCD images in the LF (left) and FLUO (right) modes. In both images the top region is the signal spot and the bottom region is the reference spot.

The CCD is continuously acquiring images and sampling R(θ) in the two spots. In Fig. 6.20, the top curves are the BSW resonances in the signal (black) and reference (blue) spots, extracted from the CCD image shown in the top left inset. For each spot, R(θ) is averaged over 80 CCD rows and θ_{LF} is tracked by an iterative fitting procedure. In Fig. 6.21 we show the plot of the θ_{LF} measured in the signal (black curve) and reference (blue curve) spots as a function of time (sensogram). By calculating the difference signal (red curve) we rule out all parasitic effects, such as the change of the refractive index of the solution upon injection, the temperature and pressure induced fluctuations of the refractive index of the solution, the temperature fluctuations of λ_{LF}, and non-specific binding contributions. From the differential baseline

recorded at the beginning in D-PBS 1X we evaluated the instrumental noise, whose standard deviation is $\sigma = 0.57$ pix.

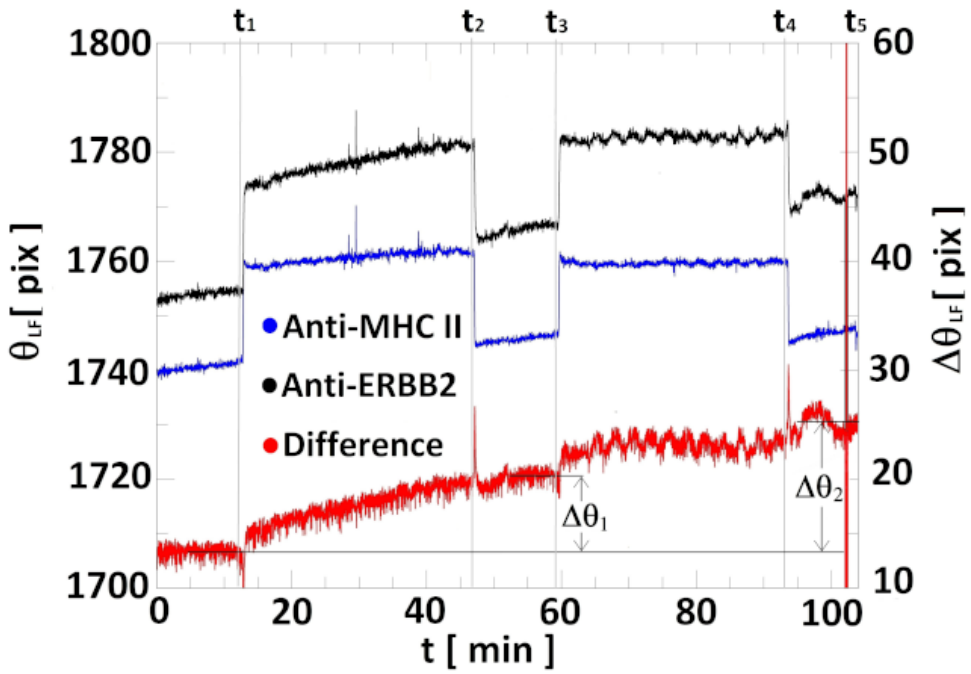

Figure 6.21 - LF sensograms recorded during the assay for the detection of ERBB2 spiked in D-PBS 1X at 20 ng/mL. The curves are for the signal spot (black), reference spot (blue) and difference (red).

At t_1 we started the LF assay by injecting the ERBB2 test solution (140 µL) and recirculating. The differential signal increases, due to specific ERBB2 binding to the capture Anti-ERBB2 spot. At t_2 we washed with D-PBS 1X (500 µL) and measured the residual angular shift $\Delta\theta_1 = 7.5$ pix at t_3. As it can be seen the 20 ng / mL concentration of ERBB2 spiked in D-PBS 1x can be clearly detected in the LF mode.

At t_3 we start the FLUO assay. We complete the sandwich immunoassay by labelling the ERBB2 molecules specifically bound to the BSW biochip surface and performing fluorescence measurements. In this particular case, this is achieved by a two-step procedure. While still tracking θ_{LF} in the LF mode (see Fig. 6.21), at t_3 we inject a biotinylated monoclonal detection antibody Anti-ERBB2 (140 µL), recirculated during incubation and washed with D-PBS 1X (500 µL) at t_4. At t_5 we measure an increased residual shift $\Delta\theta_2 = 12.5$ pix, due to further mass loading. Such part of the measurement can be also considered as an extension of the LF assay in which the detection antibody guarantees an increase of the selectivity and an amplification of the signal from $\Delta\theta_1$ to $\Delta\theta_2$. At t_5 the platform is switched to the FLUO mode, the LF laser beam is blocked, the FLUO laser beam is open and the CCD under resonant excitation

conditions at θ_{EXC} collects the background fluorescence emission. We point out that θ_{EXC} can differ in the two spots; such difference is managed by scanning θ_{EXC} and analyzing for each spot only the fluorescence images taken at resonance. Immediately after we inject neutravidin conjugated with the DyLight 650 dye (140 μL) and incubate while recirculating. Neutravidin binds efficiently to biotin and labels only the signal spot. After neutravidin incubation we wash with D-PBS 1X and measure the fluorescence emission at resonant excitation.

In Fig. 6.20, the bottom curves are the background subtracted I(θ) fluorescence spectra measured in the signal (black curve) and reference (blue curve) spots. An almost flat spectrum is observed in the reference spot, confirming that no interaction between the Anti-MHC II capture antibodies and ERBB2-Fc took place; residual luminance is due to non-specific binding and intrinsic fluorescence of the BSW biochip itself. The difference between the signal and the reference spectra confirms specific binding of ERBB2 to the signal spot and the LF result.

The assays carried out with ERBB2 spiked in D-PBS 1X were used to optimize the protocols. In some cases, we observed a weak capture efficiency of the capture Anti-ERBB2 spot, due to ad-layers formed during the bio-conjugation step and due to poorly effective washing procedures. We therefore introduced an optimized regeneration step with glycine and HCl at pH 3.0 at the beginning of the bio-recognition assay.

We modified the two-step labelling procedure that we initially adopted to keep the possibility to use different neutravidin conjugated dyes and tested the spectroscopic features of the platform. We conjugated the detection antibody Anti-ERBB2 to a reactive ester Alexa Fluor 647 (Thermo Fisher), assessing the conjugation efficiency by cyto-fluorimetry, and reduced the BSW biochip labelling procedure to a single step. This considerably simplifies our assay, reducing the duration from 100 min to 30 min (both LF and FLUO) and making it faster than either the standard [71] or the most recent [5,72] techniques described in literature.

6.5.3.2 Lysates from ERBB2 positive and negative cell lines

We carried out ERBB2 detection assays making use of the samples listed in Table VI.III for SK-BR-3 (P1 to P4) and Colo 38 (N1 to N4). In this case, on the BSW biochips' surface we defined three sensing spots, where capture Anti-ERBB2 (signal, S), or Anti-MHC II ([66], R1) and Anti-MHC I ([69], R2) were bio-conjugated. Each biochip was used for two assays in a sequence; the first with a SK-BR-3 sample in CH1 and the second with a Colo 38 sample in CH2 at identical dilutions (same total amount of proteins). The two assays were performed with a temporal delay of 1 hour; no degradation of the performances was observed within such

a timeframe. Such a strategy guarantees that the functionalization chemistry and immobilization steps were the same for the two channels and lysate solutions. As an example, in Fig. 6.22, we show the results of the LF assay carried out with one BSW biochip for the P1 sample (CH1). The curves correspond to the sensograms registered in the S (black), R1 (red) and R2 (blue) spots. In the inset we show the last part of the sensogram registered for the N1 solution (CH2).

For all BSW biochips the assay was carried out according to the following steps. At the beginning of the assay the fluorescence background was measured in FLUO mode in D-PBS 1X, then the platform was switched to the LF mode and started to record the sensograms. The fluidic cell temperature was raised from 24 °C to 30 °C, by means of the temperature controlled back plate; the drift of the signal is used to compare the sensitivity of each spot and to compensate for differences when analysing data. Regeneration with glycine-HCl at pH 3.0 is performed, followed by D-PBS 1X washing before starting the LF assay. The lysate solution (120 μL) was injected and recirculated during incubation (12 min). The biochip was then washed with D-PBS 1X. The labelled detection antibody Anti-ERBB2 AF647 (120 μL) was injected and recirculated during incubation (15 min). Finally the biochip is washed with D-PBS 1X and the fluorescence is measured in FLUO mode. The timing of the assay was the same for all biochips used in the experiments. Starting from the time of the lysate injection, the duration of the assay is 30 min. In a real application, this can be taken as the assay duration for optimized biochips that are already regenerated and ready for use when mounted on the read out platform.

From the analysis of all sensograms, which are similar to that reported in Fig. 6.22, one can conclude as follows. Clearly, specific binding of ERBB2 to the S spot takes place, whereas a reduced response due to non-specific binding is observed in the R1 and R2 spots.

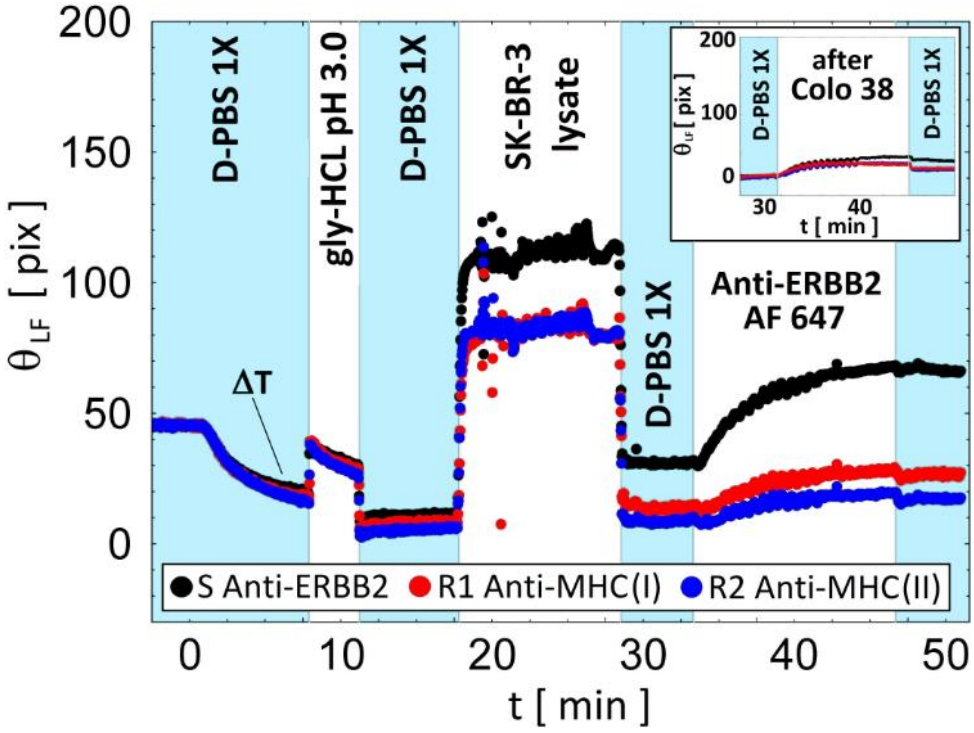

Figure 6.22: LF signal recorded during a complete ERBB2 bio-recognition assay in a SK-BR-3 cell lysate (sample P1). The three sensograms correspond to the specific (black) and non-specific (red and blue) spots where the capture mAbs were incubated. (Inset) LF signal recorded during incubation with the detection antibody for the same biochip in the CH2 and after exposing the biochip to the Colo 38 cell lysate (sample N1). The colour codes of the curves are the same as in the main figure.

One can subtract the signal and reference curves and obtain a differential signal that is only related to the specific interaction of ERBB2. However, signal fluctuations during incubation with lysate are very pronounced due to the large protein content C_{WH} and to the concentration fluctuations deriving from recirculation. This makes the differential signal very noisy and the binding kinetics hard to track. Nevertheless, a clear (final) difference $\Delta\theta_1$ between the residual shifts in the S and R1 spots (worst case) is observed after washing with D-PBS 1X. On the contrary, the signals recorded during the detection antibody incubation are much cleaner, due to the decreased complexity of the matrix. It is therefore possible to track the differential signal and the binding kinetics of the detection antibodies. Also in this case a residual shift $\Delta\theta_2 > \Delta\theta_1$ is observed (amplified LF response). Such results suggest that tracking the LF signals during the incubation with the detection antibody can give information that is much more reliable and can extend the standard label-free direct binding assays [73]. In the inset of Fig. 6.22 we show, for the N1 solution injected in CH2, the sensograms recorded during the incubation with the detection antibody. The response of all spots is low when ERBB2-negative Colo 38 lysates are added, demonstrating the ERBB2 specificity of the assay.

In Fig. 6.23 we report the differential sensograms measured in LF mode, during the Anti-ERBB2 AF647 injection (120 µL) and incubation/recirculation, for four different BSW biochips that were previously exposed to dilutions (P1 to P4) of the SK-BR-3 lysate. The differential curves are normalized by subtracting the signals recorded in the spots S and R1, respectively. All curves were obtained under the same experimental conditions. The binding kinetics and residual shifts $\Delta\theta_{RES}$ after washing with D-PBS 1X can be clearly observed. The assays carried out with the Colo 38 lysate solutions (N1 to N4), show binding kinetics and residual signals that are always below the P4 dilution (smallest ERBB2 content).

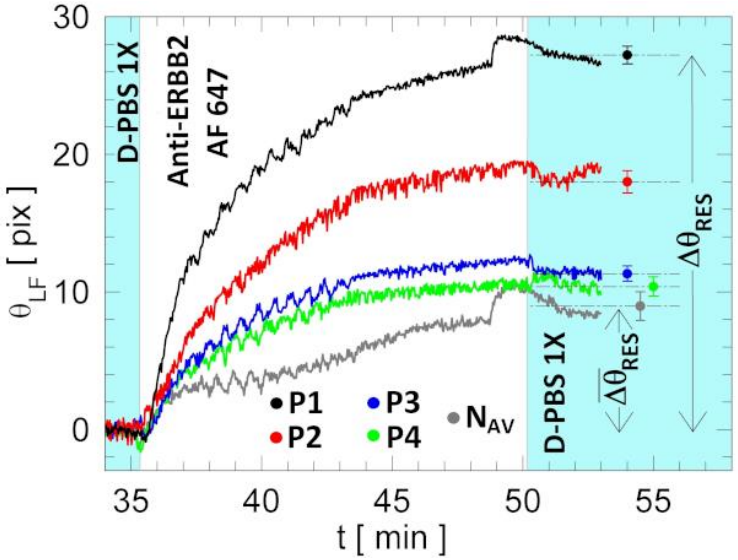

Figure 6.23 - (Curve P1 to P4) Anti-ERBB2 AF647 binding kinetics for different C_{ERBB2}. (N_{AV}) Colo 38 average signal for three BSW biochips (grey). The error bars (3σ) refer to the average residual shifts calculated in D-PBS 1X at the end of the assay. $\Delta\theta_{RES}$ is the residual shift for the P samples and $\overline{\Delta\theta}_{RES}$ is the average residual shift for the N samples.

In Fig. 6.23 we plot the differential curve obtained by averaging the sensograms for three Colo 38 lysate solutions, which shows a residual average shift $\overline{\Delta\theta}_{RES}$. In Fig. 6.24, we show the results of the measurements carried out in FLUO mode for the same assays that provided the LF results shown in Fig. 6.24. The background subtracted radiant intensity I(θ) recorded by the CCD camera for each spot and for each lysate solution (see for example Fig. 6.20) was integrated over the angular detection window, providing a the total emitted power W. The histogram summarizes the W values obtained for all cases. We observe a marked difference between the W values measured for the ERBB2 positive and negative cell lines and between the different sensing spots. In the inset of Fig. 6.24, we show, for the greatest dilution and for the three sensing spots, the difference of fluorescence powers W(P4)-W(N4) recorded for the

SK-BR-3 and Colo 38 samples, respectively. This shows that, even at the lowest ERBB2 content the assay is able to distinguish between a positive and a negative control.

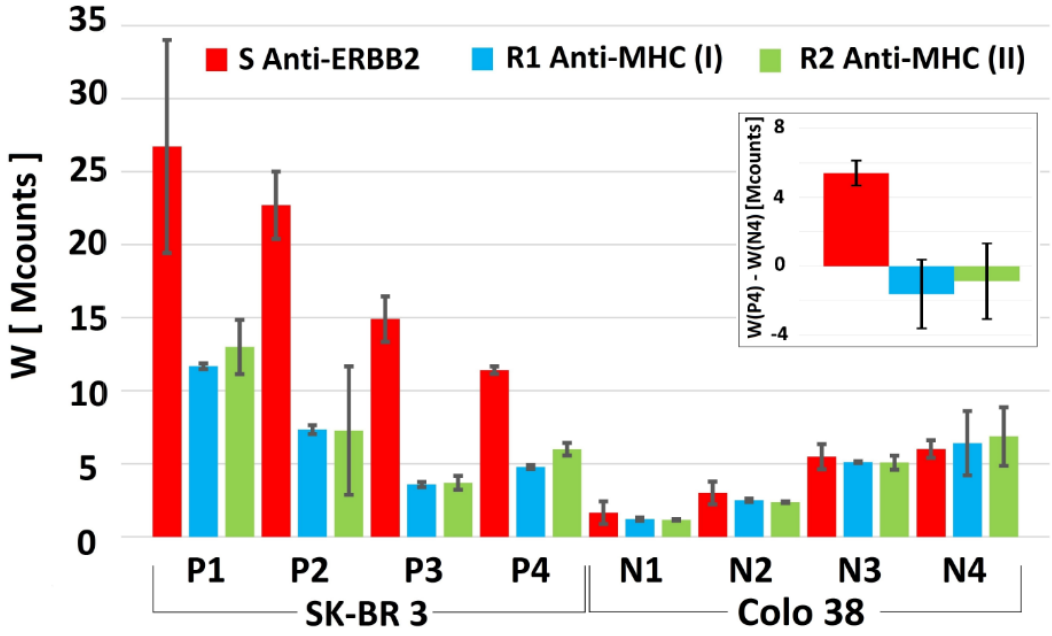

Figure 6.24 - Background subtracted power W after exposition to Anti-ERBB2 AF647 and for different SK-BR-3 and Colo 38 samples. The different colours denote fluorescence values obtained for the three sensitive spots on the BSW biochips. (Inset) W(P4)-W(N4) for the three spots.

6.5.3.3 Analysis and Discussion

The results of the experimental assays carried out with the cell lysates show that the present optical biosensing platform can operate efficiently, integrating both the LF and FLUO modes and making use of the same BSW biochips and optical read out system. In the assays, the platform detected ERBB2 in a complex matrix (cell lysates) in the FLUO mode at the clinically relevant concentration 3.5 ng/mL (19 pM). As reported in the introduction, in serum (a less complex biological matrix with respect to cell lysates), the well-established threshold for ERBB2 is placed at 15 ng/mL [74]. In the LF mode, the platform detected the ERBB2 at a concentration of 17.5 ng/m that is in the range of but not below the clinical threshold. Nevertheless, the performance in the LF is improved with respect to results of previous works with LF and FLUO combined platforms, i.e. 60-100 ng/mL in spiked samples [75,].

The experimental data are analysed more in detail below, to evaluate the limit of detection (LoD) of the immunoassay implemented on the platform, both in the LF and FLUO modes.

In Fig. 6.25a, we report the result of the analysis of the LF data shown in Fig. 6.24. For each SK-BR-3 lysate dilution, we calculated the difference $\Delta\theta_N = \Delta\theta_{RES} - \overline{\Delta\theta}_{RES}$ and plot it as a

function of C_{ERBB2}. The procedure should guarantee that all parasitic effects are ruled out. Fig. 6.25a shows that the experimental uncertainty limits data analysis and the resolution for ERBB2 label-free detection. We found that the Langmuir isotherm model does not fit to the experimental data. However, we can interpolate (red curve) by means of the Hill's model [76]:

$$\Delta\theta_N = \Delta\theta_0 + \frac{\Delta\theta_{sat} - \Delta\theta_0}{1+(K_D/c)^{\beta}} \tag{6.2}$$

where $\Delta\theta_0$ is a residual plateau level of the differential shift, $\Delta\theta_{sat}$ is the saturation level, K_D is the equilibrium dissociation constant of ERBB2 to the capture Anti-ERBB2 used in this work and β is a non-ideality parameter. From the interpolation we find: $\Delta\theta_0 = 0.62$ pixel, $\Delta\theta_{sat} = 21.9$ pixel, $K_D = 95$ ng/mL = 0.5 nM and $\beta = 1.9$. We can derive the LoD_{LF}, i.e. the minimum ERBB2 concentration that can be detected in a lysate solution, assuming that a signal can be detected if it differs from $\Delta\theta_0$ by more than the standard deviation of its associate measurement error. We find that $LoD_{LF} = 14.5$ ng/mL = 78 pM. Such result confirms that the 17.5 ng/mL can be effectively detected in the LF mode.

In Fig. 6.25b, we report the result of the analysis of the FLUO data shown in Fig. 6.24. We plot the difference W_N between the W values found in the signal spot (S), for BSW biochips exposed to either SK-BR-3 or Colo 38 samples, as a function of C_{ERBB2}. Practically, the plotted data are obtained by subtracting the N_i red columns from the P_i red columns (i from 1 to 4) in the histogram shown in Fig. 6.24.

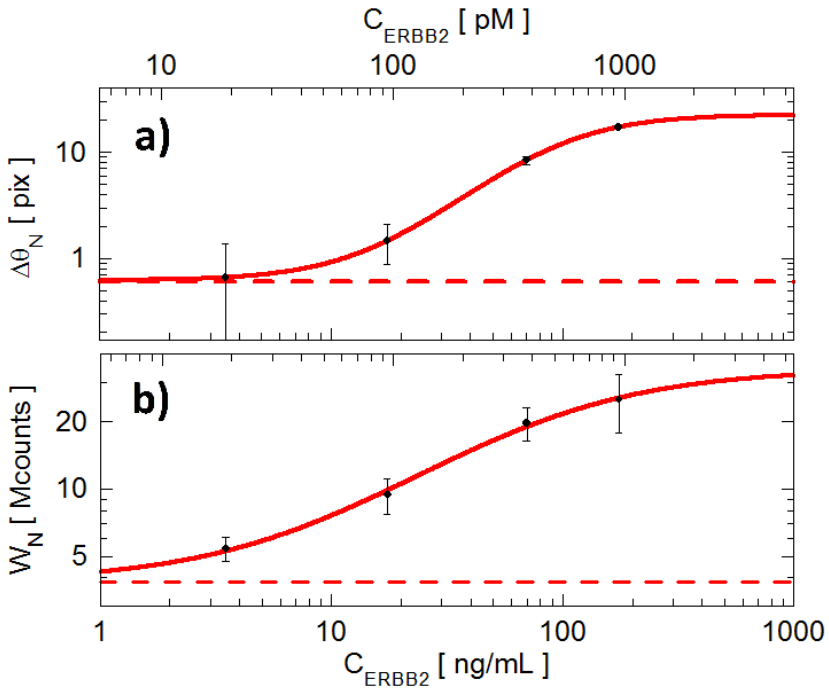

Figure 6.25 - Calibration curves for assays carried out with ERBB2 expressing cell lysates. The error bars show the standard deviation. (a) LF data interpolated with Eq.(1) (b) FLUO data fitted with Eq.(6.2). The dashed horizontal lines correspond to the $\Delta\theta_0$ and W_0 values.

We fitted the experimental data by means of a modified Langmuir isotherm model, taking into account a background signal W_0 that is not removed by the subtraction procedure and the consequent deviation from the first order kinetic behaviour in the low concentration limit [77]:

$$W_N = W_0 + \frac{W_{sat} - W_0}{1 + K_D/c} \tag{6.3}$$

where W_{sat} is the saturation. From the fit we get: W_{sat} = 30.3 Mcounts, W_0 = 3.8 Mcounts, K_D = (70 ± 25) ng/mL = (0.3 ± 0.1) nM.

The K_D value found by fitting the FLUO data, which is in the range the value interpolated from the LF data, is among the smallest found for state-of-the-art high ERBB2 affinity proteins (0.3 nM < K_D < 5.8 nM) developed for cancer therapy [78]. The value is also consistent with the estimation (1 nM) that was previously obtained using radio-binding assays on cultured cells [68]. Of course evaluating K_D from Langmuir-like plot may suffer from a great uncertainty. Kinetic measurements of the association (k_a) and dissociation (k_d) constants and of their ratio K_D=k_d/k_a would be preferable and is one of the objectives of our future work. However, the value found for K_D already gives a strong indication that the Anti-ERBB2 capture antibody used in this work is extremely specific for ERBB2.

We can derive the LoD_{FLUO}, i.e. the minimum ERBB2 concentration that can be detected in a lysate solution, assuming that a signal can be detected if it differs from W_0 by more than the standard deviation of its associate measurement error. We find that LoD_{FLUO} = (1.7 ± 0.7) ng/mL = (9 ± 4) pM. Such a result shows that in the FLUO mode the limit of detection is about 10 times smaller than the LF case. Such a LoD_{FLUO} is well below the standard immunohistochemistry (IHC) limits and in the range of the ELISA commercial kits for ERBB2 (0.2 ng/mL).

The LoD_{FLUO} we found is smaller than all other results reported in literature for ERBB2 with platforms which can be considered for point-of-care applications, say with an assay duration shorter than 2 hours ([5] and references therein).

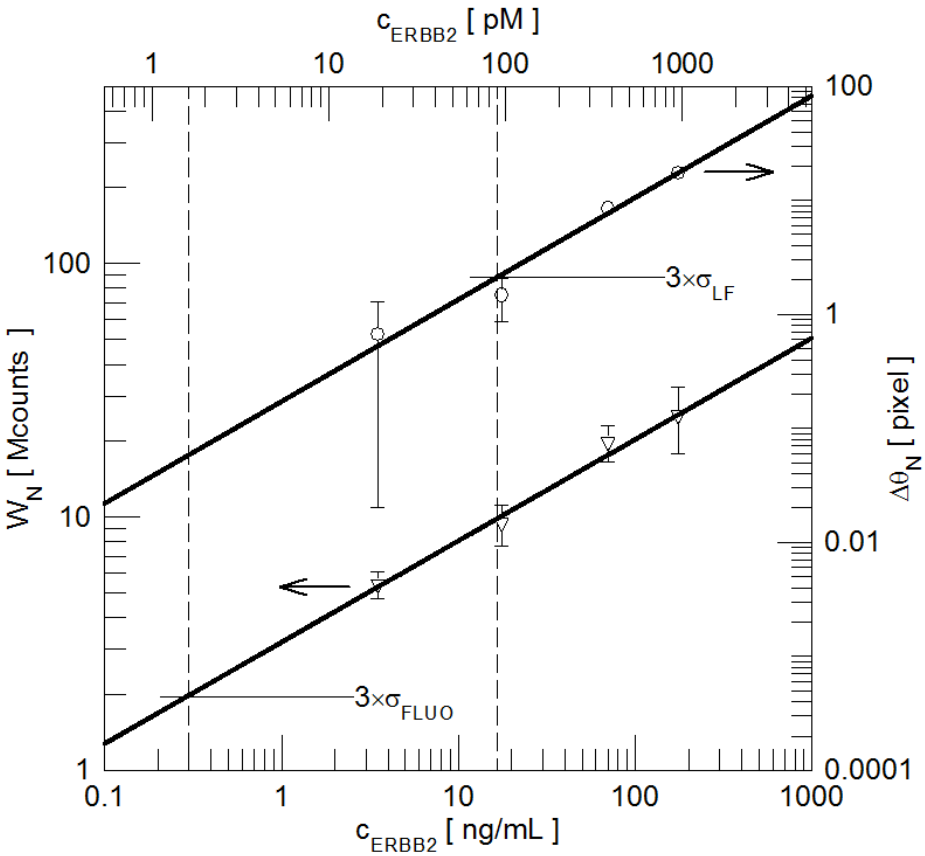

Figure 6.26 - Calibration curves for the LF and FLUO operation modes for assays carried out with ERBB2 expressing cell lysates. The lines show the linear fit and the error bars show the standard deviation.

In our case the duration of the assay is only 30 min, positioning the BSW biochip at the top of the classification in terms of assay response time, including the standard ELISA kits, whose total assay time is approximately 4 hours. We remark that, if the data shown in Fig. 6.25 are analysed according to other procedures that are commonly reported in literature [12,79], the LoD values get smaller.

According to such approaches, we linearly fitted data and evaluated the LoD as the concentration for which the fit reaches 3 times the standard deviation of the error σ (Fig. 6.26). We get $\sigma_{LF}(\Delta\theta_N) = 0.7$ pix and $LoD_{LF} = (16 \pm 9)$ ng/mL = $(90 \pm 50$ pM) and $\sigma_{FLUO}(W_N) = 0.65$ Mcounts and $LoD_{FLUO} = (0.3 \pm 0.2)$ ng/mL = (1.5 ± 1.0) pM, for the LF and FLUO case respectively. Such values should be used to compare the resolution of our platform to other systems that were calibrated according to such a procedure.

The analysis of Fig. 6.25 indicates that the LoD could be further improved by optimizing the blocking step after the mAbs bio-conjugation. An insight on the blocking efficiency can be indirectly found by observing in detail Fig. 6.24. The Colo 38 results show that increasing

values of W (for all the three spots S, R1 and R2) are found when the complexity of the matrix decreased, i.e. from N_1 to N_4, indicating that increasing lysate concentration improves the passivation. The lysate matrix contributes to blocking, playing a role in the non-specificity of the surface.

We point out that the LoD_{LF} for ERBB2 spiked in D-PBS 1X is indeed lower, as expected due to the reduced complexity of the matrix. Comparing the residual shift $\Delta\theta_2$-$\Delta\theta_1$ in Fig. 6.21 to the standard deviation of the noise σ yealds LoD_{LF} =20 ng/mL*σ/($\Delta\theta_2$-$\Delta\theta_1$) = 2.3 ng/mL = 10 pM.

CHAPTER 7
Conclusions and Future perspectives

7.1 CONCLUSIONS AND OUTCOMES OF THE THESIS WORK

In this thesis, I described the experimental work that contributed to develop a combined label-free/fluorescence platform based on one dimensional photonic crystals sustaining Bloch surface waves. By means of such a platform cancer biomarker detection protocols in complex biological media were successfully implemented.

After a general introduction on optical biosensors, the Chapter 1 was dedicated to describe the main parameters characterizing the BSW biochips in both label-free and fluorescence operation modes. Moreover, the situation of the state of the art on the combined label-free/fluorescence platforms was described showing advantages and drawbacks.

In Chapter 2, I discussed the theoretical formulation used in this work to describe the propagation of surface waves in periodically modulated dielectric stacks. In particular, a series of simulations were carried out in order to find an optimal 1DPC structure enabling an effective cancer biomarker detection. Meanwhile, I started to experimentally characterize the first 1DPC families providing quick feedback to the design and fabrication process in order to achieve optimized 1DPC. Moreover, the fluorescence operation and emission patterns were deeply described to put into evidence the decoupling mechanisms and the output response in fluorescence regime. In Chapter 3 all the bio-sensing platforms used in this work were illustrated and described in detail. In particular, I focused my experimental work on the development of the extended laboratory test bench (S1) and of the adapted SPR platform (S2). In particular, by means of S2, I obtained the first experimental validation of the combined label-free/fluorescence operation. The characterization of several generations of 1DPC, including to the final optimized one, was mainly carried out by means the platforms S1 and S3, the two instruments that were finally used for the cancer biomarker assays. The complete characterization of label-free and fluorescence operation modes was reported in Chapter 4. The

experimental FoMs on the two platforms were in very good agreement demonstrating the reliability of the results obtained on S1 and S3. During the thesis period, I strongly focused my work in protocol validation by characterizing, functionalizing and testing more than 200 biochips along last three years. These experiments were aimed to test molecule stability in different environments and to better understand protein reactions at the 1DPC surface.

Chapter 5 was completely devoted to the chemical modification of the sensing surface by means of purposely developed procedures. The main functionalization route used during the doctorate period consisted in an APTES silanization process followed by an activation step through glutaraldehyde. Standard characterization techniques (WCA, FTIR and Fluorescence Microscopy), supplemented by the test assays performed on platform S1, permitted to adapt APTES to the BSW biochips and to reach an optimized functionalization protocol. Thus, I transferred APTES protocols onto glass BSW biochip operating on platform S1 with related optimization procedures. The validated protocols on S1 were successfully transferred to plastic BSW biochips on S3. By means of such optimized protocols, a final validation of S3 was carried out in a pre-clinical environment. However, the development of complete functionalization protocols gave me the possibility to produce APTES coatings for different applications (see the Paragraphs 7.1.1 and 7.1.2). In the last part of the Chapter 5, an alternative functionalization route based on polymerized poly-acrylic acid coatings was also described. This functionalization strategy was extensively used in the first period of the doctorate in order to better understand molecular interactions.

In Chapter 6, I described the most relevant results obtained with the label-free/fluorescence platforms for cancer biomarkers detection applications.

In the first part, the use of the combined label-free and label-free/fluorescence approaches were applied to detect Angiopoietin 2 in different biological matrices. The combined approach permitted to reach a limit of detection in fluorescence mode of 4.4 ng/mL, better than commercial instruments available on the market [75].

In the second part, I focused my work on a different cancer biomarker such as ERBB2. Also in this case I developed new functionalization strategies in order to obtain optimal conditions in biochip bio-conjugation. The analytical characteristics, in terms of limit of detection of the proposed ERBB2 assay, brought to an improvement with respect to other biosensors [71, 80, 81] reaching a LoD of 0.3 ng/mL (linear extrapolation) in cell lysates. Furthermore, the presented BSW biochips show a LoD in the range of an ERBB2 commercial ELISA kit, with a considerable difference in the assay duration, only 30 minutes in this case. The resolution achieved is actually adequate for the analysis of serum sample, since 15 ng/mL was set by the

Food and Drug Administration (FDA) as the appropriate threshold between basal and abnormal ERBB2 protein expression levels.

In addition, the possibility to assay molecules using a platform that ensures two different quantification techniques (LF or FLUO modes), while maintaining the optical system unchanged, is the real added value of this platform. Combined detection in real-time introduces a clear advantage in terms of result reliability to clinical diagnosis.

7.2 FUTURE PERSPECTIVES AND BOUNDARY ACTIVITIES

The extreme versatility of the proposed platform offers the possibility to address different kind of phenomena. The unique properties of 1DPC permit to modify the penetration of the evanescent tail in the surrounding medium by simply changing the structural parameters (geometry, materials) and making it suitable for a wide range of applications. As an example, by increasing the penetration depth from 120 nm to 1000 nm, the sensitive 1DPC surface can probe efficiently bacteria activities providing information on living systems in terms of label-free and fluorescence responses. As already reported in Chapter 1, particular 1DPCs can be also used for cell adhesion studies enhancing live cell imaging applications [13,14]. In the following paragraphs, I briefly report on future research projects and boundary activities in which I have been involved during the doctorate period.

7.2.1 Characterization of cell lysates over-expressing different amount of cancer biomarkers

The perspective that is most at reach in cancer biomarker detection is to extend the last results presented in Chapter 6 to other ERBB2 positive cellular lines. The final goal is to quantify the total ERBB2 amount in cell lysates coming from different ERBB2 expressing cell lines. The analytical quantification of ERBB2 content will overcome the standard semi-quantitative techniques used in immunology laboratory, for example, immunohistochemical assays (IHC). The possibility to have an optical technique with a resolution in the order of 0.3 ng/ml can better monitor the presence of ERBB2 in cell lysates giving a direct information on the progression of a tumor already at an early stage facilitating the diagnosis and medical treatments. For this reason, we are trying to push down the LoD of the platform through continuous optimization procedures either optimizing the optical 1DPC design and the quality of the chemical functionalization/bio-conjugation.

Future investigation will also be devoted to human plasma samples, trying to apply directly the described techniques to real cases. Meanwhile, the latest experimental results obtained with the platform S3, which after the end of the BILOBA project is hosted in our laboratory and is being used for further experiments, show the potential of the cancer biomarker assay developed and optimized in our laboratory. In fact, with the present (assay) protocol, an ERBB2 concentration in D-PBS 1X (no matrix effect) down to of 0.1 ng/mL was successfully detected in both detection modes, assessing an absolute quantity of ERBB2 of 14 pg. The detection of such a small ERBB2 concentration, considerably below the cut-off given by FDA (15 ng/mL in serum), paves the way towards early diagnosis of breast cancer and to a possible lengthening the positive patient life prospects. In Fig.7.1 it is shown a complete characterization in terms of label-free and fluorescence of an ERBB2 solution at 0.1 ng/ml. The signals during the detection antibody interaction for the reference (grey-violet) and the signal (dark and light green) spots are plotted as a function of the incubation time. From the blue curve (differential sensogram) it is clear that a concentration of 0.1 ng/ml can be effectively detected (4 pixel shift). The result is confirmed by the fluorescence results. The promising results push us in setting up optimized procedures to effectively transfer our know-how into the diagnostic field.

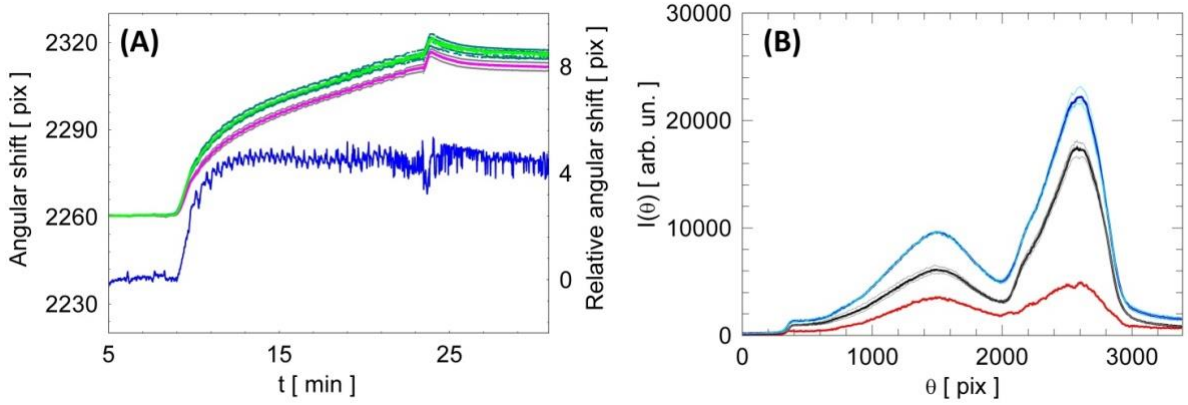

Figure 7.1 – Label-free (A) and fluorescence (B) averaged responses to an ERBB2 concentration of 0.1 ng/ml.

7.2.2 Study of fibronectin-phosphorylcholine coatings for cardiovascular applications

The possibility to monitor the interaction between biomolecules at a solid surface is key point for scientists involved in active coatings for biomedical devices. In particular, the use of biomolecules as coatings on biomaterials constitutes a promising approach to modulate the biological response of the host. A bilateral collaboration SAPIENZA (Italy) - University of Laval (Québec) started on 2016 with the aim to characterize the biomolecular interactions by

means of the platform S1. We studied a coating composed by two bio-molecules providing complementary properties for cardiovascular applications: fibronectin (FN) to enhance endothelialization, and phosphorylcholine (PRC) for its non thrombogenic properties. By exploiting the label-free detection features of platform S1, I systematically studied the interactions of the two biomolecules in different conditions: for example with/without the presence of a functional (GAH) layer, through EDC activation and varying the hydrophobicity of the 1DPC surfaces. As an example, in Fig.7.1, it is shown a typical sensogram indicating the adsorption of fibronectin (FN) and then phosphorylcholine (PRC) injected onto a bare 1DPC (A|13|634) surface.

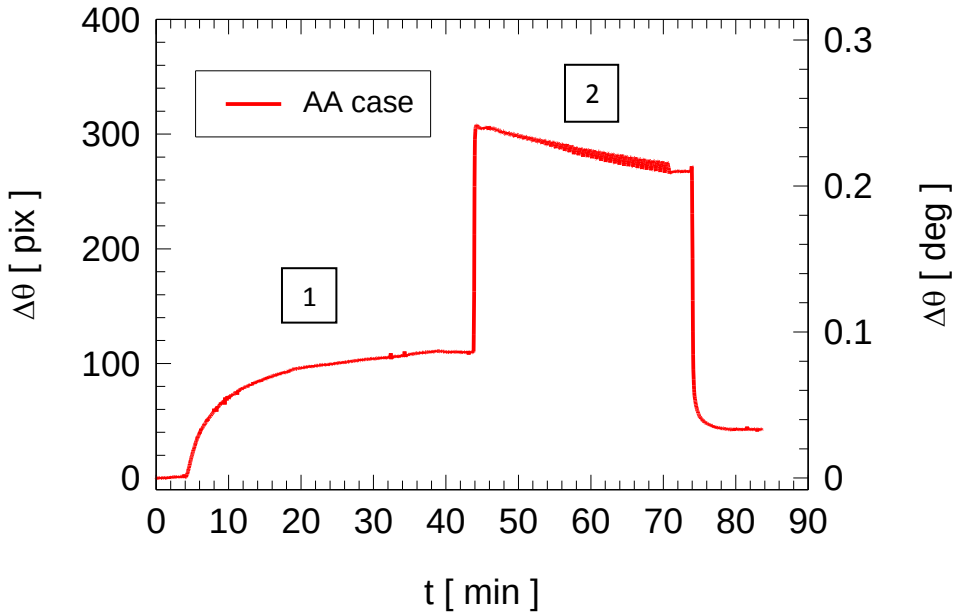

Figure 7.2 – Sensogram showing the two adsorption kinetics for FN (box 1) and PRC (box 2) on a bare 1DPC.

As appears from Fig.7.2, by means of a real-time of BSW resonance monitoring it is possible to extract useful information. By evaluating the plateau levels between the two kinetics (box 1 and 2 in Fig.7.2) measured in D-PBS 1X, one can experimentally evaluate the mass coverage and the surface density of such a molecules for different conditions (pH variations, temperature changes, extreme ionic conditions). This permits to infer on the stability of the resulting coating and calibrate the amount of proteins in terms of concentration injected to reach optimized conditions. Thereby, FN-PRC coatings are currently tested with our platform with the aim to improve cell adhesion and non-thrombogenic properties for cardiovascular applications.

7.2.3 Optimization and robustness studies on 1DPCs

During the doctorate period, I also collaborated to the optimization and robustness studies conducted on 1DPCs. In particular, we investigated experimentally and numerically the robustness of optical biosensors based on Bloch waves at the surface of periodic one-dimensional photonic crystals. The statistical distributions of sensor parameters caused by the fabrication tolerances of the dielectric layers' thicknesses in a 1DPC have been analyzed and robustness criteria have been set forth and discussed. We show that the performance of the surface wave sensors is sufficiently robust with respect to the changes of the photonic crystal layer thicknesses. Layer thickness optimization of the photonic crystal, carried out to achieve low limit of detection, leads to an improvement of the robustness of the surface wave sensors that is attributed to Bloch states lying deeper in the photonic band gap (see Chapter 2). As an example, in Fig. 7.3A, it is reported the distribution of the TE reflectivity curves around the BSW resonance in water for 19 virgin 1DPCs deposited on plastic chips.

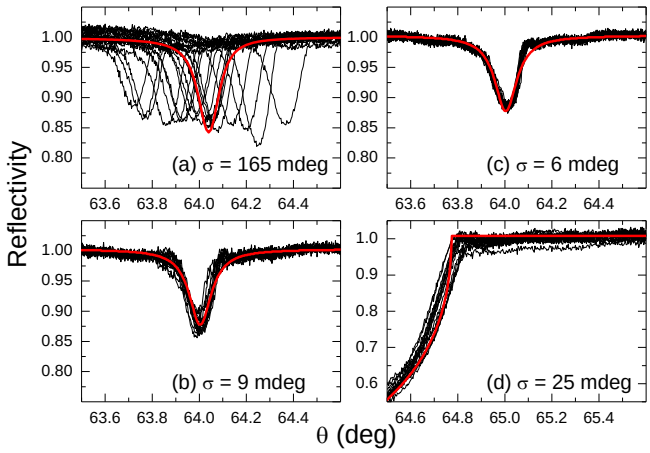

Figure 7.3 – (a) TE reflectivity curves around the BSW resonance in water for the central spot on 19 virgin 1DPCs deposited on plastic chips. Thick red curve in (a) is the fit model of the centermost reflectivity curve. (b) BSW resonance distribution due to variations among 15 different spot positions on the surface of one chip. (c) BSW resonance distribution due to the uncertainty of the mechanical fixture. The red curves in (b) and (c) are examples of the Lorentzian fit. (d) The TIR angle measurements from the surface of the TOPAS® chip in contact with 1-propanol. The red curve in (d) is an example of the Fresnel's formula fit. Measurements were performed at room temperature with the excitation wavelength centered at $\lambda_0 = 804$ nm. The standard deviation of the BSW and TIR angular positions are shown in the figures.

These activities were performed with the aim to completely control the physical parameters associated to 1DPC fabrication and characterization in order to reduce variability during critical biosensing assays.

7.3 FUNDING

This dissertation work was funded with European funds from the FP7-ICT BILOBA project.

7.4 ARTICLES PUBLISHED AND SUBMITTED DURING THE DOCTORATE PERIOD

The work reported in the present thesis has also been published and presented at peer-review journals or conferences as follows:

1) **Sinibaldi A**., Rizzo R., Figliozzi G., Descrovi E., Danz N., Munzert P., Anopchenko A., and Michelotti F.
"A full ellipsometric approach to optical sensing with Bloch surface waves on photonic crystals"
Optics Express, **21** (20), pp. 23331-23344 (2013).

2) **Sinibaldi A**., Fieramosca A., Rizzo R., Anopchenko A., Danz N., Munzert P., Magistris C., Barolo C., and Michelotti F.
Optics Letters, **39**, 10, 2947-2950 (2014).

3) R. Rizzo R., N. Danz N., Michelotti F., Munzert P., **Sinibaldi A.**
"Limit of detection comparison for surface wave biosensors"
Proc. of SPIE, SPIE Photonics Europe 14-17 (2014).

4) **Sinibaldi A.**, Rizzo R., Anopchenko A., Danz N., Descrovi E., Munzert P., and Michelotti F. "Exploiting the phase properties of Bloch surface waves on photonic crystals for efficient optical sensing"
SPIE Photonics Europe 2014, 14 - 17, Brussels, Belgium (2014).

5) **Sinibaldi A.**, Anopchenko A., Rizzo R., Danz N., Munzert P., Rivolo P., Frascella F., Ricciardi S. and Michelotti F.
"Angularly resolved ellipsometric optical bio-sensing by means of Bloch surface waves"
Anal. & Bioanal. Chem., 407 (14), 3965–3974 (2015).

6) **Sinibaldi A**., Danz N., Anopchenko A., Munzert P., Schmieder S., Chandrawati R., Rizzo R., Rana S., Sonntag F., Occhicone A., Napione L., De Panfilis S., Stevens M.M., and

Michelotti F.
“Label-Free Detection of Tumor Angiogenesis Biomarker Angiopoietin 2 Using Bloch Surface Waves on One Dimensional Photonic Crystals”
Journal of Lightwave Technology, **33**, 16, 3385-3393 (2015).

7) Danz N., **Sinibaldi A**., Munzert P., Anopchenko A., Förster E., Schmieder S., Chandrawati R., Rizzo R., , Heller R., Sonntag F., Mascioletti A., Rana S., Schubert T., Stevens M.M. and Michelotti F.
“Biosensing platform combining label-free and labelled analysis using Bloch surface waves”
Proc. of SPIE, Optical Sensors 2015, edited by Francesco Baldini, Jiri Homola, Robert A. Lieberman, Vol. 9506, 95060V.

8) **Sinibaldi A.**, Anopchenko A., Rizzo R., Danz N., Munzert P., Rivolo P., Frascella F., Ricciardi S. and Michelotti F.
“Phase-sentitive bloch surface wave biosensors,”
AISEM 2015, 18th Conference on Sensors and Microsystems, (2015).

9) Anopchenko A., Occhicone A., Rizzo R., **Sinibaldi A.**, Figliozzi G., Danz N., Munzert P., and Michelotti F.
“Effect of thickness disorder on the performance of photonic crystal surface wave sensors”
Optics Express, **24**, 7, 7728-7742 (2016).

10) Michelotti F., Schmieder S., Anopchenko A., Munzert P., **Sinibaldi A**., Chandrawati R., Rana S., Sonntag F., Occhicone A., Napione L., Stevens M. M., Maillart E., Hibti F.E., Frydman C., Danz N.
“Label-free and fluorescence biosensing platform using one dimensional photonic crystal chips”
Proc. of SPIE, 9750, 97501D-1-10 (2016).

11) Munzert P., Danz N. **Sinibaldi A.**, Michelotti F.
“Multilayer coatings for Bloch surface wave optical biosensors”
Surf. Coat. Technol., http://dx.doi.org/10.1016/j.surfcoat.2016.08.029 (published on-line, in press, 2016).

12) **Sinibaldi A.**, Sampaoli C., Danz N., Munzert P., Sibilio L., Sonntag F., Occhicone A., Tremante E., Falvo E., Giacomini P., and Michelotti F.

"Detection of soluble ERBB2 in breast cancer cell lysates using a combined label-free/fluorescence platform based on Bloch surface waves"
Submitted to *Biosensors and Bioelectronics* (2016) – status: Under Review.

13) Occhicone A., **Sinibaldi A.**, Sonntag F., Munzert P., Danz N., Michelotti F.
"A novel technique based on Bloch surface waves sustained by one-dimensional photonic crystals to probe fluid dynamics in a microfluidic channel"
Submitted to *Sensors and Actuators B* (2016) – status: Under Review.

14) Rizzo R., Alvaro M., Danz N., Napione L., Descrovi E., Schmieder S., **Sinibaldi A.**, Chandrawati R., Rana S., Munzert P., Schubert T., Maillart E., Anopchenko A., Rivolo P., Mascioletti A., Sonntag F., Stevens M.M., Bussolino F. and Michelotti F.
"Bloch surface wave platform working in tandem configuration for the detection of tumor biomarkers in different matrices"
Submitted to *Biosensors and Bioelectronics* (2016) – status: Under Review.

15) Rizzo R., Alvaro M., Danz N., Napione L., Descrovi E., Schmieder S., **Sinibaldi A.**, Chandrawati R., Rana S., Munzert P., Schubert T., Maillart E., Anopchenko A., Rivolo P., Mascioletti A., Sonntag F., Stevens M.M., Bussolino F. and Michelotti F.
"Surface enhanced fluorescence biosensor detecting clinically relevant levels of Angiopoietin-2 tumor biomarker directly from plasma of cancer patients."
Submitted to *ACS Sensors* (2016) – status: Under Review.

REFERENCES

[1] NASDAQ, *Global press release distribution* https://globenewswire.com

[2] Borisov S.M., Wolfbeis O.S.
"Optical biosensors"
Chemical. Reviews., **108**, 423–461 (2008).

[3] Van Dorst B., Mehta J., Bekaert K., Rouah-Martin E., De Coen W., Dubruel P., Blust R., Robbens J.
"Recent advances in recognition elements of food and environmental biosensors: a review."
Biosensors and Bioelectronics, **26**, 1178–1194 (2010).

[4] Dixit C.K., Vashist S.K., MacCraith B.D., and O'Kennedy R.
"Multisubstrate-compatible ELISA procedures for rapid and high-sensitivity immunoassays"
Nature Protocols, **6**, 439–445 (2011).

[5] Eletxigerra U., Martinez-Perdiguero J., Merino S., Barderas R., Torrente-Rodríguez R.M., Villalonga R., Pingarrón J.M., Campuzano S.
"Amperometric magnetoimmunosensor for ErbB2 breast cancer biomarker determination in human serum, cell lysates and intact breast cancer cells"
Biosensors and Bioelectronics, **15**;70:34-41 (2015).

[6] Long F, Zhu A., and Shi H.
"Recent Advances in Optical Biosensors for Environmental Monitoring and Early Warning"
Sensors, **13(10)**, 13928-13948 (2013).

[7] Sinibaldi A., Danz N., Descrovi E., Munzert P., Schulz U., Sonntag F., Dominici L., and Michelotti F.
"Direct comparison of the performance of Bloch surface wave and surface plasmon polariton sensors"
Sensors and Actuators B, **174**, 292– 298 (2012).

[8] Liedberg B., Nylander C., and Lundström I.
"Biosensing with surface plasmon resonance: how it all started"
Biosensors and Bioelectronics, **10**, pp. i–ix (1995).

[9] Piliarik M., and Homola J.
"Surface plasmon resonance (SPR) sensors: approaching their limits?"

Optics Express, **17**, pp. 16505–16517 (2009).

[10] Nguyen H.H., Park J., Kang S., and Kim M.
"Surface Plasmon Resonance: A Versatile Technique for Biosensor Applications"
Sensors, **15**, 10481-10510 (2015).

[11] Homola J.
"Present and future of surface plasmon resonance biosensors"
Anal. Bioanal. Chem., **377**, 528-539 (2003).

[12] Wang Y., Brunsen A., Jonas U., Dostálek J., and Knoll W.
"Prostate Specific Antigen Biosensor Based on Long Range Surface Plasmon-Enhanced Fluorescence Spectroscopy and Dextran Hydrogel Binding Matrix"
Anal. Chem., **81**, 9625–9632 (2009).

[13] Chen W., Long K.D., Lu M., Chaudhery V., Yu H., Choi J.S., Polans J., Zhuo Y., Harley B.A.C., and Cunningham B.T.
"Photonic crystal enhanced microscopy for imaging of live cell adhesion"
Analyst, **138**, 5886 (2013).

[14] Chen W., Long K.D., Yu H., Tan Y., Choi J.S., Harley B.A., and Cunningham B.T.
"Enhanced live cell imaging via photonic crystal enhanced fluorescence microscopy"
Analyst, **139**, 5954–5963 (2014).

[15] Lakowicz J.R.

"Principles of fluorescence spectroscopy"

Springer Science & Business Media (2013).

[16] S. Robinson S. and Nakkeeran R.
"Photonic Crystal Ring Resonator Based Optical Filters, Advances in Photonic Crystals"
Advances in Photonic Crystals, Prof. Vittorio Passaro (Ed.), InTech (2013).

[17] Shuo-Hui Cao S.H., Cai W.P., Liu Q., and Yao-Qun Li Y.Q.
"Surface Plasmon–Coupled Emission: What Can Directional Fluorescence Bring to the Analytical Sciences?"
Annu. Rev. Anal. Chem., 5:317–36 (2012).

[18] Ballarini M., Frascella F., Michelotti F., Digregorio G., Rivolo P., Paeder V., Musi V., Giorgis F., and Descrovi E.
"Bloch surface waves-controlled emission of organic dyes grafted on a one-dimensional photonic crystal"
Appl. Phys. Lett., **99**, 4, 043302 (2011).

[19] BILOBA-Final Summary Report (www.bilobaproject.eu)

[20] Zhuo Y. and Cunningham B.T.
"Label-Free Biosensor Imaging on Photonic Crystal Surfaces"
Sensors, **15**, 21613-21635 (2015).

[21] Lee, M. R., and Fauchet, P. M.
"Two-dimensional silicon photonic crystal based bio-sensing platform for protein detection"
Optics Express, **15**, 4530-4535 (2007).

[22] Zlatanovic S., Mirkarimi L.W., Sigalas M.M., Bynum M.A., Chow E., Robotti K. M., Burr G.W., Esener S., Grot A.
"Photonic crystal microcavity sensor for ultracompact monitoring of reaction kinetics and protein concentration"
Sensors and Actuators B, **141**, 13-19 (2009).

[23] Kang C., and Weiss S. M.
"Photonic crystal with multiple-hole defect for sensor applications"
Optics Express, **16**, 18188-18193 (2008).

[24] Wu D.K.C., Kuhlmey B. T., and Eggleton B.J.
"Ultrasensitive photonic crystal fiber refractive index sensor"
Optics Letters, **34**, 322-324 (2009).

[25] Sinibaldi A., Rizzo R., Figliozzi G., Descrovi E., Danz N., Munzert P., Anopchenko A., and Michelotti F.
"A full ellipsometric approach to optical sensing with Bloch surface waves on photonic crystals"
Optics Express, **21** (20), pp. 23331-23344 (2013).

[26] Yuan D., Dong Y., Liu Y., and Li T.

"Mach-Zehnder Interferometer Biochemical Sensor Based on Silicon-on-Insulator Rib Waveguide with Large Cross Section"
Sensors, **15**, 21500-21517 (2015).

[27] www.photonics.ethz.ch
"Photonic crystals and optical resonators"

[28] Yeh, P., Yariv, A., Hon, C-S.
"Electromagnetic propagation in periodic stratified media. I. General theory"
J. Opt. Soc. Am., **67**, 4, 423–438 (1977).

[29] P. Rivolo P.; Michelotti F.; Frascella F.; Digregorio G.; Mandracci P.; Dominici L.; Giorgis F., Descrovi E.
"Real time secondary antibody detection by means of silicon-based multilayers sustaining Bloch Surface Waves"
Sensors and Actuators B, **161**,1, 1046-1052 (2012).

[30] Homola J.
"Surface plasmon resonance sensors for detection of chemical and biological species"
Chemical Reviews, **108**, 462-493 (2008).

[31] Johnson S.G., and Joannopoulos J. D.
"Block-iterative frequency-domain methods for Maxwell's equations in a plane wave basis"
Optics Express, **8**, 3, 173-190 (2001).

[32] Rizzo R., Danz N., Michelotti F., Maillart E., Anopchenko A., and Wächter C.
"Optimization of angularly resolved Bloch surface wave biosensors"
Optics Express, **22**, 19, 23202-23214 (2014).
[33] Danz, N., Waldhäusl, R., Bräuer, A., and Kowarschik, R.
"Dipole lifetime in stratified media"
J. Opt. Soc. Am. B, **19**, 3, 412-419 (2002).

[34] Danz N., Kick A., Sonntag F., Schmieder S., Höfer B., Klotzbach U., Mertig M.
"Surface plasmon resonance platform technology for multi-parameter analyses on polymer chips"
Eng. Life Sci., **11**, 566–572 (2011).

[35] Sinibaldi A., Fieramosca A., Rizzo R., Anopchenko A., Danz N., Munzert P., Magistris

C., Barolo C., and Michelotti F.
Optics Letters, **39**, 10, 2947-2950 (2014).

[36] Sinibaldi A., Danz N., Anopchenko A., Munzert P., Schmieder S., Chandrawati R., Rizzo R., Rana S., Sonntag F., Occhicone A., Napione L., De Panfilis S., Stevens M.M., and Michelotti F.
"Label-Free Detection of Tumor Angiogenesis Biomarker Angiopoietin 2 Using Bloch Surface Waves on One Dimensional Photonic Crystals"
Journal of Lightwave Technology, **33**, 16, 3385-3393 (2015).

[37] Anopchenko A., Occhicone A., Rizzo R., Sinibaldi A., Figliozzi G., Danz N., Munzert P., and Michelotti F.
"Effect of thickness disorder on the performance of photonic crystal surface wave sensors"
Optics Express, **24**, 7, 7728-7742 (2016).

[38] Giorgis F., Descrovi E., Summonte C., Dominici L.,Michelotti F. Experimental determination of the sensitivity of Bloch surface wave based sensors.
Optics Express, **18**(8), 8087–8093 (2010).

[39] Kallury K.M.R., DeBono R.F., Krull U.J., Thompson M.
"Silanes and other coupling agents"
VSP, Zeist, Netherlands, 263–269 (1992).

[40] Vashist S.K., Lam E., Hrapovic S., Male K.B., and. Luong J. H. T
"Immobilization of Antibodies and Enzymes on 3‑Aminopropyltriethoxysilane-Functionalized Bioanalytical Platforms for Biosensors and Diagnostics"
Chemical Reviews, **114**, 11083−11130 (2014).

[41] Jonkheijm P., Weinrich D., Schröder H., Niemeyer C.M., and Waldmann H.
"Chemical Strategies for Generating Protein Biochips"
Angew. Chem. Int. Ed., **47**, 9618 – 9647 (2008).

[42] Rusmini F., Zhong Z., and Feijen J.
"Protein Immobilization Strategies for Protein Biochips"
Biomacromolecules, **8**, 1775-1789 (2007).

[43] Miller A.W., and Robyt J.F.
Biotechnology and Bioengineering, **XXV**, pp. 2795-2800 (1983).

[44] Ricciardi S., Castagna R., Severino S. M., Ferrante I., Frascella F., Celasco E., Mandracci P., Vallini I., Mantero G., Pirri C. F., Rivolo P.
"Surface functionalization by poly-acrylic acid plasma-polymerized films for microarray DNA diagnostic"
Surface and Coating Technology, **207**, 389-399 (2012).

[45] Montano-Machado V., Hugoni L., Dıaz-Rodrıguez S., Tolouei R., Chevallier P., Pauthe E., and Mantovani D.
"A comparison of adsorbed and grafted fibronectin coatings under static and dynamic conditions"
Phys.Chem.Chem.Phys., **18**, 24704 (2016).

[46] Siow K.S., Britcher L., Kumar S., Griesser H.J.
"Plasma Methods for the Generation of Chemically Reactive Surfaces for Biomolecule Immobilization and Cell Colonization - A Review"
Plasma Process. Polym., **3**, 392–418 (2006).

[47] Holash J., Wiegand S. J., and Yancopoulos G. D.
"New model of tumor angiogenesis: dynamic balance between vessel regression and growth mediated by angiopoietins and VEGF"
Oncogene, **18**, 5356-5362 (1999).

[48] Ahmad S. A., Liu W., Jung Y. D., Fan F., Reinmuth N., Bucana C. D. and Ellis L. M., "Differential expression of Angiopoietin-1 and Angiopoietin-2 in colon carcinoma,"
Cancer, **92**(5), 1138-1143 (2001).

[49] Dawood S., Broglio K., Buzdar A.U., Hortobagyi G.N., Giordano S.H.
"Prognosis of Women With Metastatic Breast Cancer by HER2 Status and Trastuzumab Treatment: An Institutional-Based Review"
J. Clin. Oncol. **28**(1):92-98 (2010).

[50] Mahfoud O.K., Rakovich T.Y., Prina-Mello A., Movia D., Alves F., and Volkov Y., "Detection of ErbB2: nanotechnological solutions for clinical diagnostics"
RSC Adv, **4**, 3422-3442 (2014).

[51] Kedenburg S., Vieweg M., Gissibl T., and Giessen H.,
"Linear refractive index and absorption measurements of nonlinear optical liquids in the visible and near-infrared spectral region"

Optical Materials Express, **2**, 1588 (2012).

[52] Sinibaldi A., Descrovi E., Giorgis F., Dominici L., Ballarini M., Mandracci P., Danz N., and Michelotti F.
"Hydrogenated amorphous silicon nitride photonic crystals for improved-performance surface electromagnetic wave biosensors"
Biomed. Opt. Express, **3**, 2405 (2012).

[53] Weast R. C.,
Handbook of Chemistry and Physics,
CRC Ed. 70th edition (1989).

[54] R. Rizzo R., N. Danz N., Michelotti F., Munzert P., Sinibaldi A.
"Limit of detection comparison for surface wave biosensors"
SPIE Photonics Europe 14-17 (2014).

[55] Nagao Y., Sakai T., Kozawa T., and Urano T.
"Synthesis and properties of barbiturate indolenine heptamethinecyanine dyes"
Dyes Pigm., **73**, 344 (2007).

[56] Barbero N., Magistris C., Park J., Buscaino R., Barolo C., and Viscardi G.
"Microwave assisted synthesis of nearinfrared fluorescent squaraine derivatives," (submitted).

[57] Tien P. K., and Ulrich R.
"Theory of Prism–Film Coupler and Thin-Film Light Guides"
J. Opt. Soc. Am., **60**, 1337 (1970).

[58] Homola J., Yee S.S., Gauglitz G.
"Surface plasmon resonance sensors: review."
Sensors Actuators B, **54**:3–15 (1999).

[59] Michelotti F., Sinibaldi A., Munzert P., Danz N., Descrovi E.
"Probing losses of dielectric multilayers by means of Bloch surface waves"
Optics Letters, **38**:616–618 (2013).

[60] Luchansky M.S., Washburn A.L., Martin T.A., Iqbal M., Gunn L.C., Bailey R.C. "Characterization of the evanescent field profile and bound mass sensitivity of a label-free silicon photonic microring resonator biosensing platform"
Biosensors & Bioelectronics, **26**:1283–1291 (2010).

[61] R&D Systems, Recombinant Human Angiopoietin 2 Specifications, Catalog Number 623 AN; Dr. Fioravanti E.(R&D Systems) direct personal communication.

[62] Maillart E.
"Développement d'un biocapteur par imagerie SPR,"
PhD dissertation, Université Paris XI, France (2004).

[63] Voros J.
"The density and refractive index of absorbing protein layers"
Biophys. J., **87**, 1, 553-561 (2004).

[64] www.gelifesciences.com Biacore Assay Handbook
GE Healthcare Bio-Sciences AB, Uppsala, Sweden, (2012).

[65] ShiY., HuangW., TanY., Jin X., Dua R., Penuel E., Mukherjee A., Sperinde J., Pannu H., Chenna A., DeFazio-Eli L., Pidaparthi S., Badal Y., Wallweber G., Chen L., Williams S., Tahir H., Larson J., Goodman L., Whitcomb J., Petropoulos C., Winslow J.
"A novel proximity assay for the detection of proteins and protein complexes: quantitation of HER1 and HER2 total protein expression and homodimerization in formalin-fixed, paraffin-embedded cell lines and breast cancer tissue"
DiagnMol. Pathol., 18, 11–21 (2009).

[66] Zhang Y., González R.M., Zangar R.C.
"Protein secretion in human mammary epithelial cells following HER1 receptor activation: influence of HER2 and HER3 expression"
BMC Cancer, 11:69, 10.1186/1471-2407-11-69 (2011).

[67] Galeffi P., Lombardi A., Donato M.D., Latini A, Sperandei M., Cantale C., Giacomini P.
"Expression of single-chain antibodies in transgenic plants"
Vaccine, 23:1823-1827 (2005).

[68] Digiesi G., Giacomini P., Fraioli R., Mariani M., Nicotra M.R., Segatto O., et al.
"Production and Characterization of Murine mAbs to the Extracellular Domain of Human Neu Oncogene Product GP185HER2"
Hybridoma, **11**, 519-527 (1992).

[69] Giacomini P., Beretta A., Nicotra M. R., Ciccarelli G., Martayan A., Cerboni C., et al.

"HLA-C Heavy Chains Free of Beta2-Microglobulin: Distribution in Normal Tissues and Neoplastic Lesions of Non-Lymphoid Origin and Interferon-Gamma Responsiveness"
Tissue Antigens, **50**, 555-566 (1997).

[70] Ozato K., Mayer N. M., Sachs D.H.
"Monoclonal Antibodies to Mouse MHC Antigens. III. Hybridoma Antibodies Reacting to Antigens of the H-2b Haplotype Reveal Genetic Control of Isotype Expression"
Transplantation, **34**(3), 113-120 (1982).

[71] Marques R.C., Viswanathan S., Nouws H.P., Delerue-Matos C., González-García M.B.
"Electrochemical immunosensor for the analysis of the breast cancer biomarker HER2 ECD"
Talanta, **129**, 594-599 (2014).

[72] Patris S., De Pauw D., Vandeput M., Huet J., VanAntwerpen P., Muyldermans S., Kauffmann J.M.
"Nanoimmunoassay onto a screen printed electrode for HER2 breast cancer biomarker determination"
Talanta, **130**, 164-170 (2014).

[73] Eletxigerra U., Martinez-Perdiguero J., Barderas R., Pingarrón J.M., Campuzano S., Merino S.
"Surface plasmon resonance immunosensor for ErbB2 breast cancer biomarker determination in human serum and raw cancer cell lysates"
Anal. Chim. Acta, **905**, 156-162 (2016).

[74] Carney W.P., Bernhardt D., and Jasani B.,
"Circulating HER2 Extracellular Domain: A Specific and Quantitative Biomarker of Prognostic Value in all Breast Cancer Patients?"
Biomark Cancer, **5**, 31-39 (2013).

[75] Michelotti F., Schmieder S., Anopchenko A., Munzert P., Sinibaldi A., Chandrawati R., Rana S., Sonntag F., Occhicone A., Napione L., Stevens M. M., Maillart E., Hibti F. E., Frydman C., Danz N.
"Label-free and fluorescence biosensing platform using one dimensional photonic crystal chips"
Proc. of SPIE, 9750, 97501D-1-10 (2016).

[76] Morales A. J., Swairjo M. A., and Schimmel P.

"Structure-specific tRNA-binding protein from the extreme thermophile Aquifex aeolicus" *EMBO J.*, **18**, 3475–3483 (1999).

[77] O'Shannessy D. J., Winzor D. J.
"Interpretation of Deviations from Pseudo-First-Order Kinetic Behavior in the Characterization of Ligand Binding by Biosensor Technology"
Anal. Biochem., **236**, 275–283 (1996).

[78] Nilvebrant J., Åstrand M., Georgieva-Kotseva M., Björnmalm M., Löfblom J., Hober S.
"Engineering of Bispecific Affinity Proteins with High Affinity for ERBB2 and Adaptable Binding to Albumin"
PLOS ONE, **9**, e103094 (2014).

[79] Vaisocherová H., Faca H., Taylor V.M., Hanash A. D., Jiang S.
"Comparative study of SPR and ELISA methods based on analysis of CD166/ALCAM levels in cancer and control human sera"
Biosensors and Bioelectronics, **24**, 2143 (2009).

[80] Al-Khafaji Q. A. M., Harris M., Tombelli S., Laschi S., Turner A. P. F., Mascini M., and Marrazza G.
"An Electrochemical Immunoassay for HER2 Detection"
Electroanalysis, **24**, 4, 735–742 (2012).

[81] Mucelli S.P., Zamuner M., Tormen M., Stanta G., Ugo P.
"Nanoelectrode ensembles as recognition platform for electrochemical immunosensors"
Biosensors and Bioelectronics, **23**,1900–1903 (2008).